27. Aboudi, J. 1989. Micromechanical analysis of composites by the method of cells. *Applied Mechanics Reviews*, 42(7), 193–221.
28. Paul, B. 1960. Prediction of elastic constants of multi-phase materials. *Transactions of AIME*, 218, 36–41.
29. Hashin, Z. and Rosen, B.W. 1964. The elastic moduli of fiber reinforced materials. *Journal of Applied Mechanics*, 31, 223–232. Errata, p. 219 (March 1965).
30. Torquato, S. 1991. Random heterogeneous media: microstructure and improved bounds on effective properties. *Applied Mechanics Reviews*, 44(2), 37–76.
31. Halpin, J.C. and Tsai, S.W. 1969. Effects of environmental factors on composite materials. AFML-TR-67-423.

4

Strength of a Continuous Fiber-Reinforced Lamina

4.1 Introduction

Because of the variety of failure modes that can occur in composites, the analysis of composite strength is more difficult than the analysis of elastic behavior, which was discussed in chapter 2 and chapter 3. As shown in chapter 1, the strength of a composite is derived from the strength of the fibers, but this strength is highly directional in nature. For example, the longitudinal strength of the continuous fiber-reinforced lamina, s_L, is much greater than the transverse strength, s_T. In addition, the compressive strengths $s_L^{(-)}$ and $s_T^{(-)}$ associated with these directions may be different from the corresponding tensile strengths $s_L^{(+)}$ and, $s_T^{(+)}$, and the transverse tensile strength $s_T^{(+)}$ is typically the smallest of all the lamina strengths for reasons that will be explained later. The in-plane shear strength s_{LT} associated with the principal material axes is still another independent property. These five lamina strengths form the basis of a simplified lamina strength analysis, which will, in turn, be used later in a simplified laminate strength analysis. The relationships among these five lamina strengths and the allowable lamina strengths under off-axis or multiaxial loading are discussed in this chapter, as are several micromechanical models for predicting the lamina strengths. Interlaminar strengths will be discussed in chapter 7 and chapter 9.

As shown in chapters 2 and chapter 3, the linear elastic stress–strain relationships for the orthotropic lamina are simplified by the use of "effective moduli." The effective moduli, which relate the volume-averaged lamina stresses to the volume-averaged lamina strains [recall equation (2.7) to equation (2.9)], are defined by simple uniaxial or shear stress conditions associated with the lamina principal material axes. Using a similar approach, the "effective strengths" of the lamina may be defined as ultimate values of the volume-averaged stresses that cause failure of the lamina under these same simple states of stress. The stress–strain curves in figure 4.1 show the graphical interpretation of these simple states of stress, the effective strengths $s_L^{(+)}$, $s_L^{(-)}$, $s_T^{(+)}$, $s_T^{(-)}$, and s_{LT}, and the corresponding

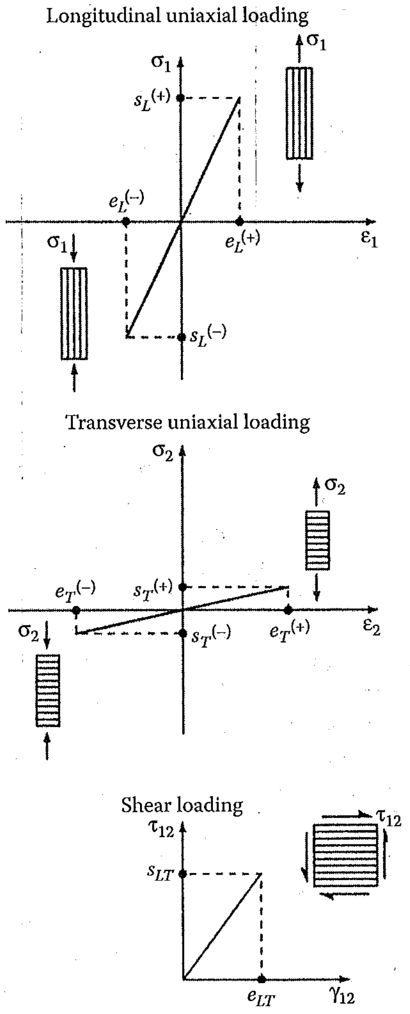

FIGURE 4.1
Stress–strain curves for uniaxial and shear loading showing lamina in-plane strengths and ultimate strains.

ultimate strains $e_L^{(+)}$, $e_L^{(-)}$, $e_T^{(+)}$, $e_T^{(-)}$, and e_{LT}. If we assume linear elastic behavior up to failure, the ultimate stresses are related to the ultimate strains by

$$s_L^{(+)} = E_1 e_L^{(+)}; \quad s_T^{(+)} = E_1 e_T^{(+)}; \quad s_{LT} = G_{12} e_{LT}$$
$$s_L^{(-)} = E_1 e_L^{(-)}; \quad s_T^{(-)} = E_2 e_T^{(-)} \tag{4.1}$$

Typical experimental values of the effective lamina strengths for selected composites are given in table 4.1 [1,2]. Note that the transverse tensile strength, $s_T^{(+)}$, is the lowest of all the strengths. As shown later, this condition is often responsible for the so-called "first ply failure" in a laminate. It is also interesting to note in table 4.1 that the compressive strengths are not necessarily equal to the corresponding tensile strengths; the transverse compressive strengths are generally greater than the transverse tensile strengths, and the longitudinal compressive strengths are usually less than or equal to the longitudinal tensile strengths. The intrinsic compressive strength of composites has always been difficult to determine experimentally, however, and the validity of such compression test results is a subject of continuing debate. Recent test results indicate that if the proper technique is used, the compression strength may be about the same as the tensile strength. Measurement of composite properties will be discussed in more detail later in chapter 10.

In this section, the lamina effective strengths under simple states of stress have been defined. In the next section, we will discuss the use of these properties in several theories for predicting lamina strength under off-axis or multiaxial loading conditions. Elementary mechanics of materials models for micromechanical prediction of several of the lamina strengths will also be described in this chapter for illustrative purposes.

4.2 Multiaxial Strength Criteria

In the cases of off-axis or multiaxial loading, we assume that lamina failure can be characterized by using a multiaxial strength criterion (or failure criterion) that incorporates the gross mechanical strengths described in the previous section. The objective of such a theory is to provide the designer with the capability to estimate quickly when lamina failure will occur under complex loading conditions other than simple uniaxial or shear stresses. In this semiempirical "mechanics of materials" approach, we do not concern ourselves with the details of specific micromechanical failure modes such as fiber pullout, fiber breakage, fiber microbuckling, matrix cracking, and delamination. The actual failure process is complicated by the fact that these microfailure modes may occur in various combinations and sequences. Indeed, as pointed out by Hashin [3], our knowledge of the details of failure at the micromechanical level is so incomplete that "the failure process cannot be followed analytically." The existence and growth of cracks and other defects in the composite are also ignored with this approach. Studies of micromechanical failure modes generally require the use of more advanced approaches

TABLE 4.1

Typical Values of Lamina Strengths for Several Composites at Room Temperature

Material	$s_L^{(+)}$ Ksi (MPa)	$s_L^{(-)}$ Ksi (MPa)	$s_T^{(+)}$ Ksi (MPa)	$s_T^{(-)}$ Ksi (MPa)	s_{LT} Ksi (MPa)
Boron/5505 boron/epoxy $\upsilon_f = 0.5^a$	230(1586)	360(2482)	9.1(62.7)	35.0(241)	12.0(82.7)
AS/3501 carbon/epoxy $\upsilon_f = 0.6^a$	210(1448)	170(1172)	7.0(48.3)	36.0(248)	9.0(62.1)
T300/5208 carbon/epoxy $\upsilon_f = 0.6^a$	210(1448)	210(1448)	6.5(44.8)	36.0(248)	9.0(62.1)
IM7/8551-7 carbon/epoxy $\upsilon_f = 0.6^b$	400(2578)	235(1620)	11.0(75.8)		
AS4/APC2 carbon/PEEK $\upsilon_f = 0.58^c$	298.6(2060)	156.6(1080)	11.3(78)	28.4(196)	22.8(157)
B4/6061 Boron/aluminum $\upsilon_f = 0.50^c$	199(1373)	228(1573)	17.1(118)	22.8(157)	18.5(128)
Kevlar® 49/epoxy aramid/epoxy $\upsilon_f = 0.6^a$	200(1379)	40(276)	4.0(27.6)	9.4(64.8)	8.7(60.0)
Scotchply® 1002 E-glass/epoxy $\upsilon_f = 0.45^a$	160(1103)	90(621)	4.0(27.6)	20.0(138)	12.0(82.7)
E-glass/470-36 E-glass/vinyl ester $\upsilon_f = 0.30^d$	85(584)	116(803)	6.2(43)	27.1(187)	9.3(64.0)

Note: Kevlar® is a registered trademark of DuPont Company, and Scotchply® is a registered trademark of 3M Company.

Source: [a]From Chamis, C.C. 1987. *Engineers' Guide to Composite Materials*, 3-8–3-24, ASM International, Materials Park, OH. With permission.
[b]From Hexcel Website www.hexcel.com.
[c]From Daniel, I.M. and Ishai, O. 1994, Engineering Mechanics of Composite Materials, Oxford University Press, New York. With permission.
[d]Courtesy of Ford Motor Company, Research Staff.

such as fracture mechanics and are the subjects of numerous journal publications. Additional discussion of such topics will be given in section 4.3 and in chapter 9.

Available multiaxial composite failure criteria have been reviewed and discussed by Hashin [4], Wu [5], Sendeckyj [6], Chamis [7], Kaminski and Lantz [8], Franklin [9], Tsai [10], Christensen [11], and Zhu et al. [12]. During the period from 1998 to 2004, Soden, Hinton, and Kaddour reported on the various aspects of the so-called World Wide Failure Exercise (WWFE) in a series of journal articles [13–22] and a book [23]. The WWFE was an international exercise in which the developers of 19 leading composite material failure theories were asked to apply their theories to predict failure in unidirectional laminae and in multiply laminates under 14 different test cases involving complex states of stress. The results from the different theories were compared with each other and with experimental data. Since this chapter only covers prediction of failure in unidirectional laminae, only the key results of the WWFE that are relevant to lamina failure prediction will be discussed here, and the results that are relevant to laminate failure prediction will be deferred until later in chapter 7. Complete coverage of the WWFE is beyond the scope of this book, and the reader is referred to the previously mentioned journal articles [13–22] and the book [23] for details. All the criteria are phenomenological, having evolved from attempts to develop analytical models to describe experimental observations of failure under combined stresses. As pointed out by Wu [5], a large experimental database alone could form the basis for an empirical failure criterion, but the semiempirical mathematical model is preferable because it can reduce the number of required experiments and provide a more systematic approach to design. None of the available theories has been shown to accurately predict failure for all materials and loading conditions, however, and there is no universal agreement as to which theory is best.

Many of the failure criteria for anisotropic composites are based on generalizations of previously developed criteria for predicting the transition from elastic to plastic behavior in isotropic metallic materials. As such, they make use of the concept of a "failure surface" or "failure envelope" generated by plotting stress components in stress space. The coordinate axes for the stress space generally correspond to the stresses along the principal material axes. The theory predicts that those combinations of stresses whose loci fall inside the failure surface will not cause failure, whereas those combinations of stresses whose loci fall on or outside the surface will cause failure. *Thus, in the application of all the failure criteria, the first step is the transformation of calculated stresses to the principal material axes.* Since we are only dealing with two-dimensional stress states in a lamina at this point, the failure surface would be 2-D. Failure surfaces for each of the criteria will be presented as they are discussed here.

4.2.1 Maximum Stress Criterion

The Maximum Stress Criterion for orthotropic laminae was apparently first suggested in 1920 by Jenkins [24] as an extension of the Maximum Normal Stress Theory (or Rankine's Theory) for isotropic materials, which is covered in elementary mechanics of materials courses [25]. This criterion predicts failure when any principal material axis stress component exceeds the corresponding strength. Thus, in order to avoid failure according to this criterion, the following set of inequalities must be satisfied:

$$-s_L^{(-)} < \sigma_1 < s_L^{(+)}$$
$$-s_T^{(-)} < \sigma_2 < s_T^{(+)} \quad (4.2)$$
$$|\tau_{12}| < s_{LT}$$

where the numerical values of $s_L^{(-)}$ and $s_T^{(-)}$ are assumed to be positive. It is assumed that shear failure along the principal material axes is independent of the sign of the shear stress τ_{12}. Thus, only the magnitude of τ_{12} is important, as shown in the last of equations (4.2). *As shown later, however, the shear strength for off-axis loading may depend on the sign of the shear stress.*

The failure surface for the Maximum Stress Criterion in $\sigma_1 - \sigma_2$ space is a rectangle, as shown in figure 4.2. Note that this failure surface is independent of the shear and stress τ_{12}, and that the criterion does not account for possible interaction between the stress components. That is, the predicted limiting value of a particular stress component is the same whether or not other stress components are present. Figure 4.3 shows a

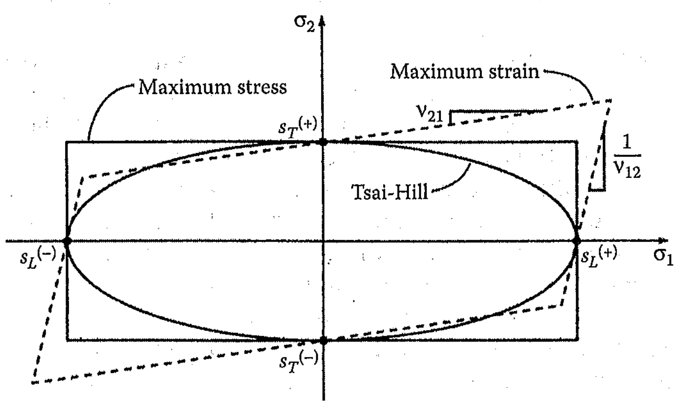

FIGURE 4.2
Maximum Stress, Maximum Strain, and Tsai–Hill failure surfaces in σ_1, σ_2 space.

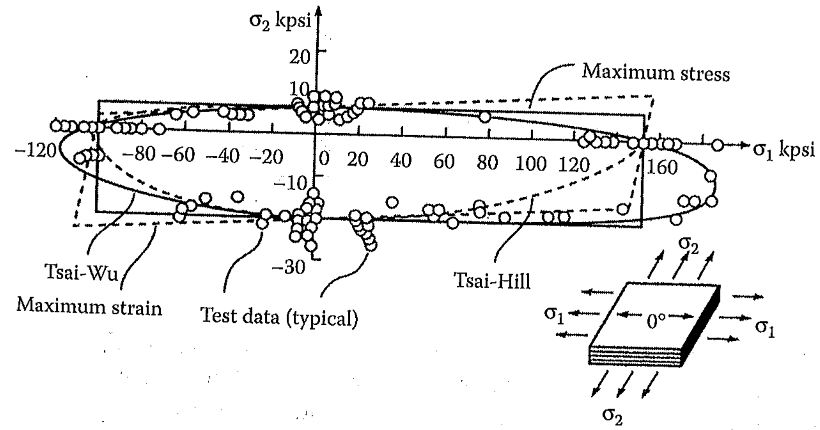

FIGURE 4.3
Comparison of predicted failure surfaces with experimental failure data for graphite/epoxy. (From Burk, R.C. 1983. *Astronautics and Aeronautics*, 21(6), 58–62. Copyright AIAA. Reprinted with permission.)

comparison of theoretical failure surfaces with experimental biaxial failure data for a unidirectional graphite/epoxy composite [26]. Since the strengths along the principal material directions provide the input to the criterion, we would expect the agreement to be good when the applied stress is uniaxial along those directions. Due to lack of stress interaction in the Maximum Stress Criterion, however, the agreement is not so good in biaxial stress situations. The scatter in the experimental data is unfortunately typical for composite strength tests.

Experimental biaxial failure data for comparison with predicted failure surfaces can be obtained by applying biaxial loading directly to the test specimens. Biaxial stress fields can also be generated indirectly by using off-axis uniaxial loading tests [27] or off-axis shear-loading tests. According to equations (2.31), the applied normal stress, σ_x, in the off-axis uniaxial loading test shown in figure 4.4 produces the following biaxial stress state along the principal material axes

$$\sigma_1 = \sigma_x \cos^2\theta$$
$$\sigma_2 = \sigma_x \sin^2\theta \quad (4.3)$$
$$\tau_{12} = -\sigma_x \sin\theta\cos\theta$$

where the applied normal stress, σ_x, may be positive or negative. The importance of the sign of the applied stress in the

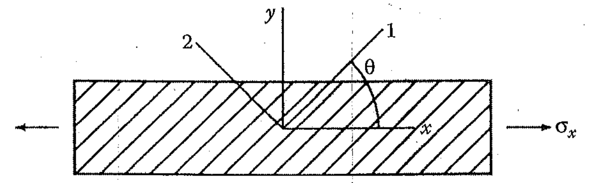

FIGURE 4.4
Off-axis uniaxial test of a unidirectional lamina specimen.

test results here is obvious. These stress components may then be substituted into equations similar to equations (4.2) in order to generate failure surfaces. By plotting the predicted and measured values of σ_x at failure versus lamina orientation, θ, the various failure criteria can be evaluated [28].

For the off-axis shear test described in figure 4.5, the applied shear stress, τ_{xy}, generates the following biaxial stress state along the principal material axes according to equations (2.31):

$$\sigma_1 = 2\tau_{xy}\cos\theta\sin\theta$$
$$\sigma_2 = -2\tau_{xy}\cos\theta\sin\theta \qquad (4.4)$$
$$\tau_{12} = \tau_{xy}(\cos^2\theta - \sin^2\theta)$$

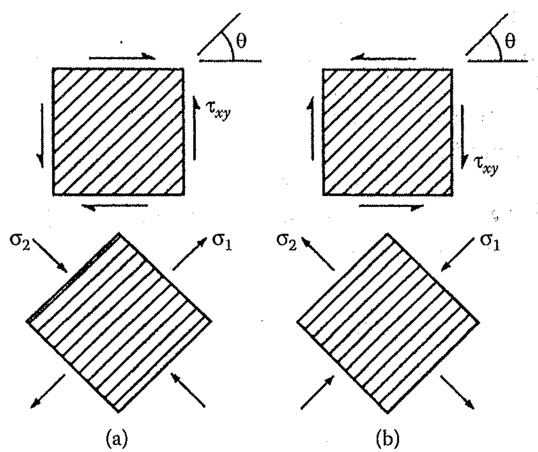

FIGURE 4.5
Off-axis shear test of a unidirectional lamina specimen. (a) Positive τ_{xy}; (b) negative τ_{xy}.

The importance of the sign of the applied shear stress in the interpretation of test results may not be so obvious here, and further discussion is warranted. For example, if the angle $\theta = 45°$, equations (4.4) reduce to $\sigma_1 = \tau_{xy}$, $\sigma_2 = -\gamma_{xy}$, and $\tau_{12} = 0$. Thus, a positive applied shear stress, τ_{xy}, would produce longitudinal tension and transverse compression along the principal material axes, as shown in figure 4.5(a). On the other hand, a negative applied shear stress would produce longitudinal compression and transverse tension, as shown in figure 4.5(b). Given the fact that the transverse tensile strength is so much lower than the other strengths (table 4.1), the importance of the sign of the applied off-axis shear stress should now be obvious. It is easy to visualize a situation where a negative shear stress of a certain magnitude could cause a transverse tensile failure, whereas a positive shear stress of the same magnitude would not cause failure. A similar development for pure shear along the principal material axes shows that the sign of the shear stress makes no difference in that case. The importance of the sign of the shear stress extends beyond the interpretation of tests results as described here; it has implications for all phases of stress analysis in composite materials.

EXAMPLE 4.1

An element of an orthotropic lamina made of T300/5208 carbon/epoxy material is subjected to a positive off-axis shear stress, τ_{xy}, at an angle $\theta = 45°$ as shown in figure 4.5(a). Determine the value of the off-axis shear stress τ_{xy} that would cause failure according to the Maximum Stress Criterion.

Solution. From figure 4.5(a), it is seen that a positive off-axis shear stress produces longitudinal tension and transverse compression along the principal material axes. Employing equations (2.31) and the Maximum Stress Criterion, along with the strength data for T300/5208 from table 4.1, the calculations are as follows:

For failure by the longitudinal tensile stress,

$$\sigma_1 = 2\tau_{xy}\cos\theta\sin\theta = 2\tau_{xy}\cos 45°\sin 45° = \tau_{xy} = S_L^{(+)} = 1448\,\text{MPa}$$

So the corresponding off-axis shear stress required to produce this mode of failure is

$$\tau_{xy} = 1448\,\text{MPa}$$

For failure by the transverse compressive stress:

$$\sigma_2 = -2\tau_{xy}\cos\theta\sin\theta = -2\tau_{xy}\cos 45°\sin 45° = -\tau_{xy} = S^{(-)} \ldots$$

So the corresponding off-axis shear stress required to produce this mode of failure is:

$$\tau_{xy} = 248\,\text{MPa}$$

There is no shear stress along the principal material axes, since

$$\tau_{12} = \tau_{xy}(\cos^2\theta - \sin^2\theta) = \tau_{xy}(\cos^2 45° - \sin^2 45°) = 0$$

So transverse compression is the governing mode of failure, and the value of the off-axis shear stress required to produce failure is:

$$\tau_{xy} = 248\,\text{MPa}$$

EXAMPLE 4.2

Repeat example 4.1 if the off-axis shear stress in example 4.1 is negative, as shown in figure 4.5(b).

Solution. From figure 4.5(b), it is seen that a negative off-axis shear stress produces longitudinal compression and transverse tension along the principal material axes. Employing equation (2.31) and the Maximum Stress Criterion, along with the strength data for T300/5208 from table 4.1, the calculations are now as follows:

For failure by the longitudinal compressive stress,

$$\sigma_1 = -2\tau_{xy}\cos\theta\sin\theta = -2\tau_{xy}\cos 45°\sin 45° = -\tau_{xy} = -S_L^{(-)} = -1448\,\text{MPa}$$

So the corresponding off-axis shear stress required to produce this mode of failure is:

$$\tau_{xy} = 1448\,\text{MPa}$$

For failure by the transverse tensile stress,

$$\sigma_2 = 2\tau_{xy}\cos\theta\sin\theta = 2\tau_{xy}\cos 45°\sin 45° = \tau_{xy} = S_T^{(+)} = 44.8\,\text{MPa}$$

So the corresponding off-axis shear stress required to produce this mode of failure is:

$$\tau_{xy} = 44.8\,\text{MPa}$$

Again there is no shear stress along the principal material axes, since

$$\tau_{12} = \tau_{xy}(\cos^2\theta - \sin^2\theta) = \tau_{xy}(\cos^2 45° - \sin^2 45°) = 0$$

So transverse tension is now the governing mode of failure, and the corresponding value of the off-axis shear stress required to produce failure is now only

$$\tau_{xy} = 44.8\,\text{MPa}$$

So simply changing the sign of the off-axis shear stress from positive to negative produces a completely different mode of failure and a much lower failure stress.

4.2.2 Maximum Strain Criterion

In 1967, Waddoups [29] proposed the Maximum Strain Criterion for orthotropic laminae as an extension of the Maximum Normal Strain Theory (or Saint Venant's Theory) for isotropic materials, which is also discussed in elementary mechanics of materials courses [25]. This criterion predicts failure when any principal material axis strain component exceeds the corresponding ultimate strain. In order to avoid failure according to this criterion, the following set of inequalities must be satisfied:

$$\begin{aligned} -e_L^{(-)} &< \varepsilon_1 < e_L^{(+)} \\ -e_T^{(-)} &< \varepsilon_2 < e_T^{(+)} \\ |\gamma_{12}| &< e_{LT} \end{aligned} \tag{4.5}$$

where the numerical values of $e_L^{(-)}$ and $e_T^{(-)}$ are assumed to be positive and the ultimate strains are all *engineering strains* as defined by equation (4.1). As with the Maximum Stress Criterion, it is assumed that shear failure along the principal material axes is independent of the sign of the shear strain γ_{12}.

Due to the similarity of equation (4.5) and equation (4.2), the failure surface for the Maximum Strain Criterion in $\varepsilon_1 - \varepsilon_2$ space is a rectangle similar to that of the Maximum Stress Criterion in $\sigma_1 - \sigma_2$ space. In $\sigma_1 - \sigma_2$ space, however, the Maximum Strain Criterion failure surface is a skewed parallelogram, as shown in figure 4.2 and figure 4.3. The shape of the parallelogram can be deduced by combining the lamina stress–strain relationships in equation (2.24) with the relationships ...

equation (4.1). For example, the limiting strain associated with the positive 1 direction is

$$\varepsilon_1 = \frac{s_L^{(+)}}{E_1} = \frac{\sigma_1}{E_1} - \frac{\nu_{12}\sigma_2}{E_1} \tag{4.6}$$

$$\sigma_2 = \frac{\sigma_1 - s_L^{(+)}}{\nu_{12}} \tag{4.7}$$

which is the equation of a straight line having intercept ($s_L^{(+)}$, 0) and slope $1/\nu_{12}$ (fig. 4.2). A similar development using the limiting strain along the positive 2 direction yields the equation:

$$\sigma_2 = \nu_{21}\sigma_1 + s_T^{(+)} \tag{4.8}$$

which is the equation for a straight line having intercept (0, $s_T^{(+)}$) and slope ν_{21}. These lines form the right and top sides, respectively, of the parallelogram shown in figure 4.2, and similar consideration of the limiting strains in the negative 1 and 2 directions yields equations for the remaining two sides. It should be noted, however, that depending on the magnitudes of the lamina strengths and stiffnesses, the intercepts of the Maximum Strain Criterion parallelogram may not be the same as those of the Maximum Stress Criterion rectangle in stress space. For some materials, the lines defining the top and bottom of the Maximum Strain Criterion parallelogram intercept the horizontal axis at stresses less than the measured tensile and compressive longitudinal strengths, which contradicts experimental evidence [5,8]. According to Wu [5], such contradictions develop as a result of an ambiguous conversion from strain space to stress space unless certain mathematical constraints on the properties are satisfied. Only for isotropic materials are the intercepts always the same for the maximum stress and maximum strain criteria. As with the Maximum Stress Criterion, the Maximum Strain Criterion does not account for possible interaction between stress components, and the predicted failure surface does not show good agreement with experimental biaxial failure data for graphite/epoxy in figure 4.3. Off-axis uniaxial test data have led to similar conclusions [28], but both criteria are still used for orthotropic materials because the resulting equations are relatively simple.

4.2.3 Quadratic Interaction Criteria

The so-called quadratic interaction criteria also evolved from early failure theories for isotropic materials, but they differ from the maximum stress and maximum strain criteria in that they include terms to account for

interaction between the stress components, and the quadratic forms of the equations for plane stress lead to elliptical failure surfaces. As shown in any mechanics of materials book, the maximum distortional energy criterion or von Mises Criterion (circa early 1900s) is the most widely used quadratic interaction criteria for predicting the onset of yielding in isotropic metals [25]. In 1948, Hill [30] suggested that the von Mises Criterion could be modified to include the effects of induced anisotropic behavior in initially isotropic metals during large plastic deformations. For a general three-dimensional state of stress along the principal axes of anisotropy (the 123 axes) in such a material, the failure surface (or yield surface) for the Hill Criterion in σ_1, σ_2, and σ_3 space is described by the equation:

$$A(\sigma_2-\sigma_3)^2 + B(\sigma_3-\sigma_1)^2 + C(\sigma_1-\sigma_2)^2 + 2D\tau_{23}^2 + 2E\tau_{31}^2 + 2F\tau_{12}^2 = 1 \tag{4.9}$$

where A, B, C, D, E, and F are determined from yield strengths in uniaxial or shear loading. In order to avoid failure, the left-hand side of equation (4.9) must be <1, and failure is predicted if the left-hand side is ≥1. For a uniaxial test along the 1 direction with $\sigma_1 = Y_1$ and all other stresses equal to zero equation (4.9) reduces to:

$$B + C = \frac{1}{Y_1^2} \tag{4.10}$$

where Y_1 is the yield strength along 1 direction. Similarly, uniaxial tests along the 2 and 3 directions give the equations

$$A + C = \frac{1}{Y_2^2}; \quad A + B = \frac{1}{Y_3^2} \tag{4.11}$$

where Y_2 and Y_3 are the uniaxial yield strengths along the 2 and 3 directions, respectively. The yield strengths in tension and compression are assumed to be the same. Solving equation (4.10) and equation (4.11) simultaneously for A, B, and C, we find that

$$\begin{aligned} 2A &= \frac{1}{Y_2^2} + \frac{1}{Y_3^2} - \frac{1}{Y_1^2} \\ 2B &= \frac{1}{Y_3^2} + \frac{1}{Y_1^2} - \frac{1}{Y_2^2} \\ 2C &= \frac{1}{Y_1^2} + \frac{1}{Y_2^2} - \frac{1}{Y_3^2} \end{aligned} \tag{4.12}$$

Similarly, for pure shear tests along the 23, 31, and 12 planes, equation (4.9) gives:

$$2D = \frac{1}{Y_{23}^2}; \quad 2E = \frac{1}{Y_{31}^2}; \quad 2F = \frac{1}{Y_{12}^2} \tag{4.13}$$

where Y_{12}, Y_{23}, and Y_{31} are the yield strengths in shear associated with the 12, 23, and 31 planes, respectively.

The extension of the Hill Criterion to prediction of failure in an orthotropic, transversely isotropic lamina was suggested by Azzi and Tsai [31] and Tsai [32]; the resulting equation is often referred to as the Tsai–Hill Criterion. If the 123 directions are assumed to be the principal material axes of the transversely isotropic lamina, with the 1 direction being along the reinforcement direction, if plane stress is assumed ($\sigma_3 = {}_{31} = \tau_{23} = 0$), and if Hill's anisotropic yield strengths are replaced by the corresponding effective lamina strengths, then $Y_1 = s_L$, $Y_2 = Y_3 = s_T$, and $Y_{12} = s_{LT}$, and equation (4.9), equation (4.12), and equation (4.13) reduce to the equation for the Tsai–Hill failure surface:

$$\frac{\sigma_1^2}{s_L^2} - \frac{\sigma_1\sigma_2}{s_L^2} + \frac{\sigma_2^2}{s_T^2} + \frac{\tau_{12}^2}{s_{LT}^2} = 1 \tag{4.14}$$

As with the Hill equation, failure is avoided if the left-hand side of equation (4.14) is <1, and failure is predicted if the left-hand side is ≥1. The failure surface generated by this equation is an ellipse, as shown in figure 4.2. The ellipse shown in figure 4.2 is symmetric about the origin because of the assumption of equal strengths in tension and compression. The Tsai–Hill equation can be used when tensile and compressive strengths are different by simply using the appropriate value of s_L and s_T for each quadrant of stress space. For example, if σ_1 is positive and σ_2 is negative, the values of $s_L^{(+)}$ and $s_T^{(-)}$ would be used in equation (4.14). The resulting failure surface is no longer symmetric about the origin, as shown for the case of graphite/epoxy in figure 4.3. Although such a procedure is inconsistent with the assumptions used in formulating the original von Mises and Hill Criteria, it has been successfully used for some composites [25,32]. As shown in figure 4.3, the procedure seems to work reasonably well for the graphite/epoxy material except for the fourth quadrant of stress space. One way to account for different strengths in tension and compression is to include terms that are linear in the normal stresses σ_1, σ_2, and σ_3, as suggested by Hoffman [33].

In addition to the previously mentioned limitations of the quadratic interaction criteria based on the von Mises model, there is another problem. Since the von Mises and Hill Criteria are phenomenological theories for the prediction of yielding in ductile metals, the equations are based on

principal stress differences and the corresponding shear stresses and strains that drive slip and dislocation movement in metallic crystals. Experimental evidence suggests that a hydrostatic state of stress does not cause the slip and dislocation movements that are associated with yielding, and the Hill Criterion predicts that failure will never occur under a hydrostatic state of stress $\sigma_1 = \sigma_2 = \sigma_3$, and $\tau_{12} = \tau_{23} = \tau_{31} = 0$. Due to shear coupling, however, a hydrostatic state of stress in an anisotropic material can produce shear strains and failure. Hoffman's equation [33], by virtue of its linear terms, could predict failure for the hydrostatic state of stress. However, all of these theories turn out to be special cases of a more general quadratic interaction criterion, which will be discussed next.

In 1971, Tsai and Wu [34] proposed an improved and simplified version of a tensor polynomial failure theory for anisotropic materials that had been suggested earlier by Gol'denblat and Kopnov [35]. In the Tsai–Wu general quadratic interaction criteria, the failure surface in stress space is described by the tensor polynomial:

$$F_i\sigma_i + F_{ij}\sigma_i\sigma_j = 1 \tag{4.15}$$

where the contracted notation $i, j = 1, 2, \ldots, 6$ is used, and F_i and F_{ij} are experimentally determined strength tensors of the second and fourth rank, respectively. In order to avoid failure, the left-hand side of equation (4.15) must be < 1, and failure is predicted when the left-hand side is ≥1. For the case of plane stress with $\sigma_3 = \sigma_{33} = 0$, $\sigma_4 = \tau_{23} = 0$, and $\sigma_5 = \tau_{31} = 0$, equation (4.15) becomes

$$F_{11}\sigma_1^2 + F_{22}\sigma_2^2 + F_{66}\sigma_6^2 + F_1\sigma_1 + F_2\sigma_2 + 2F_{12}\sigma_1\sigma_2 = 1 \tag{4.16}$$

where the linear terms in the shear stress $\sigma_6 = \tau_{12}$ have been dropped because the shear strength along the principal material axes is not affected by the sign of the shear stress. Thus, only a quadratic term in the shear stress σ_6 remains. However, the linear terms in the normal stresses $\sigma_1 = \sigma_{11}$ and $\sigma_2 = \sigma_{22}$ are retained because they take into account the different strengths in tension and compression. In addition, the term $2F_{12}\sigma_1\sigma_2$ takes into account interaction between the normal stresses. With the exception of F_{12}, all the strength tensors in equation (4.16) can be expressed in terms of the uniaxial and shear strengths using the same approach that was used with the Hill Criterion. For example, for the tension and compression tests with uniaxial stresses $\sigma_1 = s_L^{(+)}$ and $\sigma_1 = s_L^{(-)}$, respectively, simultaneous solution of the two equations resulting from equation (4.16) yields:

$$F_{11} = \frac{1}{s_L^{(+)}s_L^{(-)}} \quad \text{and} \quad F_1 = \frac{1}{s_L^{(+)}} - \frac{1}{s_L^{(-)}} \tag{4.17}$$

where the numerical value of $s_L^{(-)}$ is assumed to be positive as in table 4.1. From similar uniaxial and shear tests, it can be shown that

$$F_{22} = \frac{1}{s_T^{(+)} s_T^{(-)}}; \quad F_2 = \frac{1}{s_T^{(+)}} - \frac{1}{s_T^{(-)}}; \quad F_{66} = \frac{1}{s_{LT}^2} \tag{4.18}$$

where the numerical value of $s_T^{(-)}$ is assumed to be positive.

In order to find the interaction parameter, F_{12}, it is necessary to use a biaxial test involving both σ_1 and σ_2. For example, an expression for F_{12} can be obtained by substituting the biaxial stress conditions $\sigma_1 = \sigma_2 = P$ and $\sigma_6 = 0$ into equation (4.16), where P is the biaxial failure stress [34]. Thus, in order to find F_{12} for this condition, we need to know P in addition to the previously defined uniaxial and shear failure stresses. There is no a priori reason that σ_1 must equal σ_2, however. Indeed, as pointed out by Hashin [3], F_{12} can have four different values, because there are four different failure pairs σ_1, σ_2. Wu [5,36] has suggested that in order to determine F_{12} accurately, the biaxial ration $B = \sigma_1/\sigma_2$ must be optimized to account for the sensitivity of F_{12} to experimental scatter in the applied stresses. The optimization procedure is complicated, however, and the reader is referred to the articles by Wu [5,36] for details. The Tsai–Wu failure surface for graphite/epoxy shown in figure 4.3 was based on such an optimization procedure for F_{12}. In figure 4.3 the agreement with experimental data seems to be much better for the Tsai–Wu failure surface than for the others, particularly in the fourth quadrant.

More recently, Tsai and Hahn [37] have proposed the equation

$$F_{12} = \frac{(F_{11}F_{22})^{1/2}}{2} \tag{4.19}$$

which causes equation (4.16) to take on the form of a generalized von Mises Criteron for the yielding of isotropic materials. It is also interesting to note that equation (4.16) reduces to equation (4.14), the Tsai–Hill Criterion, when the tensile and compressive strengths are assumed to be equal and

$$F_{12} = -\frac{1}{2s_L^2} \tag{4.20}$$

On the basis of the quantitative evaluation procedure used in the previously mentioned WWFE [13–23], the organizers of the exercise selected what they considered to be the best five of the original 19 failure theories with regard to recommended use by designers. The predicted failure

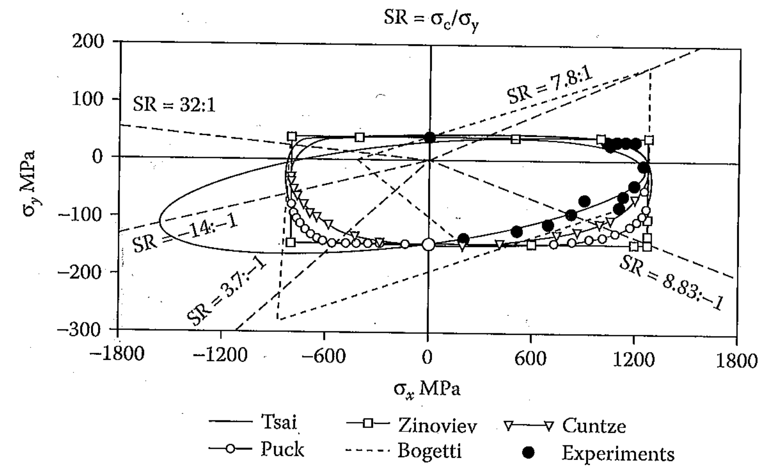

FIGURE 4.6
Comparison of predicted and measured biaxial failure surface for unidirectional E-glass/epoxy laminae under combined normal stresses in directions parallel (σ_x) and perpendicular (σ_y) to the fibers. (From Soden, P.D., Kaddour, A.S., and Hinton, M.J. 2004. *Composites Science and Technology*, 64(3–4), 589–604. With permission.)

surfaces for the five selected criteria are compared with experimental test results for unidirectional E-glass/epoxy materials under the biaxial normal stresses σ_x and σ_y in figure 4.6 and under combined transverse normal stresses σ_y and in-plane shear stresses τ_{xy} in figure 4.7. In figure 4.6 and figure 4.7, the notations Zinoviev, Bogetti, Tsai, Puck, and Cuntze refer to the following five failure criteria:

- Zinoviev et al. [38,39] used the Maximum Stress Criterion (i.e., equations [4.2]) to predict failure of a single lamina. Linear elastic behavior was assumed up to initial failure. For laminate failure prediction, additional features were included after first ply failure.
- Bogetti et al. [40,41] employed a three-dimensional version of the Maximum Strain Criterion (i.e., equations 4.5 are for the two-dimensional version only). Linear elastic behavior was assumed up to initial failure in the normal stress–normal strain relationships, but nonlinear shear stress–shear strain behavior was assumed. Additional features including progressive lamina failure were included for laminate analysis.
- Tsai et al., [42,43] used the Tsai–Wu Criterion (i.e, equation 4.16) and assumed linear elastic behavior up to initial ply failure. For

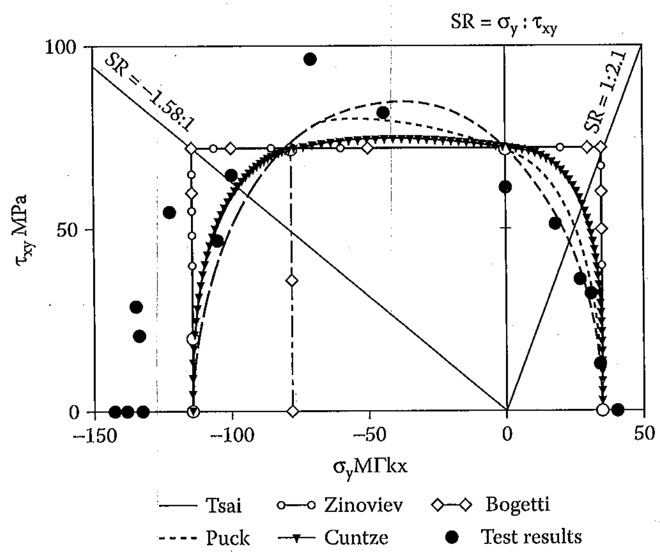

FIGURE 4.7
Comparison of predicted and measured failure surfaces for unidirectional E-glass/epoxy laminae under combined in-plane shear stress (τ_{xy}) and normal stress perpendicular to the fibers (σ_y). (From Soden, P.D., Kaddour, A.S., and Hinton, M.J. 2004. *Composites Science and Technology*, 64(3–4), 589–604. With permission.)

laminate failure prediction, a progressive failure analysis feature was added.

- Puck and Schurmann [44,45] and Cuntze et al. [46,47] employed similar three-dimensional progressive failure theories, which are beyond the scope of this book.

From figure 4.6 and figure 4.7, the organizers of the WWFE observed that the predictions of Tsai, Puck, and Cuntze gave the best overall agreement with available experimental data [19]. However, the Tsai predictions were believed to be potentially unconservative in the compression-compression quadrant of figure 4.6 where there is a lack of experimental data. The Puck predictions appeared to be unconservative in the tension–compression of figure 4.6, but fared better overall in figure 4.7. The predictions of Zinoviev and Bogetti were observed to be unconservative in several regions of both figure 4.6 and figure 4.7. Finally, it was recommended that the combined theories of Tsai, Puck, and Cuntze be used in such a way that, for a given quadrant of the failure surface, the theory that produces the innermost portion of the failure surface in that quadrant should be selected for the purpose of lamina design.

The development of improved multiaxial strength criteria for composites continues to be the subject of numerous publications. For example, Hashin [3,4] has suggested that for a given composite, each failure mode and its contributing stresses should be identified, and that each of these failure modes should be modeled separately by a quadratic criterion. Tennyson et al. [48] have extended the tensor polynomial criterion to include cubic terms. Obviously, the evaluation of the strength parameters in such an equation is a formidable task. It was shown, however, that in the particular case of failure in laminated tubes under internal pressure loading, the cubic criterion is more accurate than the quadratic criterion. Although considerable progress has been made, there is still a need for systematic experimental verification of the various theories for a variety of stress conditions. Finally, the theories discussed in this section are based on the macromechanical behavior of the composite without regard for the micromechanical behavior of fiber and matrix materials. In the next section, several micromechanical models for predicting composite strength will be presented.

EXAMPLE 4.3

The filament wound pressure vessel described in example 2.3 is fabricated from E-glass/epoxy having the lamina strengths listed in table 4.1. Determine the internal pressure p, which would cause failure of the vessel according to (a) the Maximum Stress Criterion and (b) the Tsai–Hill Criterion.

Solution. The first step in the application of both theories is to determine the stresses along the principal material axes. From the results of example 2.3, $\sigma_1 = 20.5p$, $\sigma_2 = 17.0p$, and $\sigma_{12} = 6.0p$ (all in MPa). Note that both normal stresses are positive, so that the tensile strengths should be used in the failure theories.

(a) For the Maximum Stress Criterion, the three possible values of p at failure are found as follows:

$\sigma_1 = 20.5p = s_L^{(+)} = 1103$ MPa; therefore, $p = 53.8$ MPa
$\sigma_2 = 17.0p = s_T^{(+)} = 27.6$ MPa; therefore, $p = 1.62$ MPa
$\sigma_{12} = 6.0p = s_{LT} = 82.7$ MPa; therefore, $p = 13.78$ MPa

Thus, the transverse tensile failure governs, and failure occurs first at $p = 1.62$ MPa.

(b) For the Tsai–Hill Criterion, equation (4.14) yields

$$\left(\frac{20.5p}{1103}\right)^2 - \frac{(10.5p)(17.0p)}{(1103)^2} + \left(\frac{17.0p}{27.6}\right)^2 + \left(\frac{6.0p}{82.7}\right)^2 = 1$$

Solving for p, we find that $p = 1.61$ MPa. Thus, for this case, the two criteria yield approximately the same result. This is not always true, however.

EXAMPLE 4.4

Using the Maximum Strain Criterion, determine the uniaxial failure stress, σ_x, for off-axis loading of the unidirectional lamina in figure 4.4 if the material is AS/3501 carbon/epoxy and the angle $\theta = 30°$.

Solution. First, the strains along the principal material axes must be found in terms of the applied stress, σ_x. Upon substituting the stress transformation (eqs. [4.3]) in the lamina stress–strain equations (2.24) and (2.25), we find that

$$\varepsilon_1 = \frac{1}{E_1}\left(\cos^2\theta - \nu_{12}\sin^2\theta\right)\sigma_x$$

$$\varepsilon_2 = \frac{1}{E_2}\left(\sin^2\theta - \nu_{21}\cos^2\theta\right)\sigma_x$$

and

$$\gamma_{12} = -\frac{1}{G_{12}}\left(\sin\theta\cos\theta\right)\sigma_x$$

Assuming linear elastic behavior up to failure and using the stress–strain relations in equation (4.1), the Maximum Strain Criterion (eq. [4.5]) becomes

$$\sigma_x < \frac{s_L^{(+)}}{\cos^2\theta - \nu_{12}\sin^2\theta}$$

$$\sigma_x < \frac{s_T^{(+)}}{\sin^2\theta - \nu_{21}\cos^2\theta}$$

$$\sigma_x < \frac{s_{LT}}{\sin\theta\cos\theta}$$

where only the tensile strengths have been used because σ_x is positive. Using the AS/3501 data in table 2.2 and table 4.1, we find that in order to avoid longitudinal tensile failure

$$\sigma_x < \frac{1448}{(0.886)^2 - 0.3(0.5)^2}\,\text{MPa} \quad \text{or} \quad \sigma_x < 2145\,\text{MPa}$$

In order to avoid transverse tensile failure,

$$\sigma_x < \frac{48.3}{(0.5)^2 - 0.0195(0.866)^2}\,\text{MPa} \quad \text{or} \quad \sigma_x < 205\,\text{MPa}$$

and in order to avoid shear failure,

$$\sigma_x < \frac{62.1}{0.886(0.5)}\,\text{MPa} \quad \text{or} \quad \sigma_x < 143\,\text{MPa}$$

Thus, according to the Maximum Strain Criterion, the mode of failure is shear, and the applied stress at failure is $\sigma_x = 143$ MPa. The reader is encouraged to check that for compressive loading or other loading angles both the mode of failure and the failure stress may be different. The off-axis tensile test has been used to check the validity of the various failure criteria [27,28].

4.3 Micromechanics Models for Lamina Strength

In this section, the use of elementary mechanics of materials approaches to micromechanical modeling of lamina strength will be described. We should not expect such simple models for strength to be as accurate as those for stiffness, because the strength is affected more than the stiffness by material and geometric nonhomogeneity and the resulting local perturbations in the stress and strain distributions. As shown in chapter 3, the effects of such local stress and strain perturbations on stiffness are reduced due to the smoothing effect of integration in the effective modulus theories. On the other hand, material failure is often initiated at the sites of such stress and strain concentrations, so the effect on strength is much greater. For example, as shown in figure 4.8 from ref. [49], the variability of strength in reinforcing fibers alone may be quite significant, and statistical methods must be used for accurate analysis. In addition, differences between tensile and compressive modes of failure make it necessary to develop different micromechanics models for tensile strengths and compressive strengths.

4.3.1 Longitudinal Strength

Simple micromechanics models for composite longitudinal tensile strength can be developed from the rule of mixtures for longitudinal stress (eq. [3.19]), and the representative stress–strain curves for fiber, matrix, and composite materials are shown in figure 4.9(a) and figure 4.9(b). In figure 4.9(a), the matrix failure strain, $e_{m1}^{(+)}$, is assumed to be greater than the fiber failure strain, $e_{f1}^{(+)}$, which is typical for many polymer matrix composites. A model for this case by Kelly and Davies [50] will be summarized here. Figure 4.9(b) shows the case where the fiber failure strain is greater than the matrix-failure strain, which is typical for ceramic matrix composites. A model based

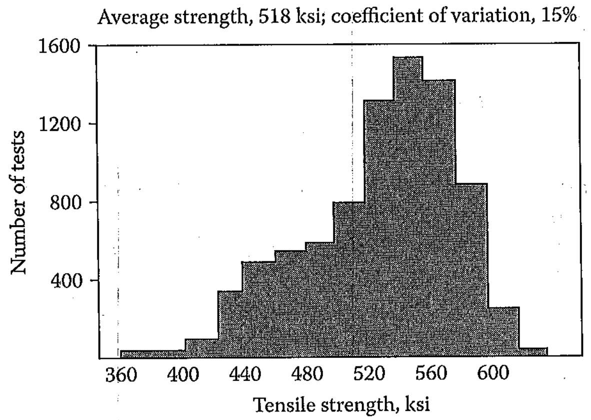

FIGURE 4.8
Statistical distribution of tensile strength for boron filaments. (From Weeton, J.W., Peters, D.M., and Thomas, K.L., eds. 1987. *Engineers' Guide to Composite Materials*. ASM International, Materials Park, OH. Reprinted by permission of ASM International.)

on the one proposed by Hull [51] will be described for this case. For both cases shown in figure 4.9, the analyses will be developed on the assumptions of (1) equal strengths in all fibers, (2) linear elastic behavior up to failure, and (3) equal longitudinal strains in composite, fiber, and matrix (recall eqs. [3.22]).

For the case described in figure 4.9(a), the composite must fail at a strain level corresponding to the fiber tensile failure strain, $e_{f1}^{(+)} = s_{f1}^{(+)}/E_{f1}$. Theoretically, if the matrix could support the full applied load after fiber failure, the strain could be increased to the matrix failure strain. For all practical purposes, however, fiber failure means composite failure Thus, when the fiber longitudinal stress reaches the fiber tensile strength, $s_{f1}^{(+)}$, the matrix longitudinal stress reaches a value $s_{mf1}^{(+)} = E_m e_{f1}^{(+)}$, the composite longitudinal stress reaches the composite tensile strength, $s_L^{(+)}$, and equation (3.19) becomes

$$s_L^{(+)} = s_{f1}^{(+)}\upsilon_f + s_{mf1}^{(+)}\upsilon_m = s_{f1}^{(+)}\upsilon_f + s_{mf1}^{(+)}(1-\upsilon_f) \tag{4.21}$$

However, equation (4.21) only has a meaning if the fiber volume fraction is sufficiently large. As shown in figure 4.9(a) and figure 4.10(a), if the fiber volume fraction $\upsilon_f < \upsilon_{fcrit}$, the composite strength from equation (4.21) is less than the matrix strength, where

$$\upsilon_{fcrit} = \frac{s_{m1}^{(+)} - s_{mf1}^{(+)}}{s_{f1}^{(+)} - s_{mf1}^{(+)}} \tag{4.22}$$

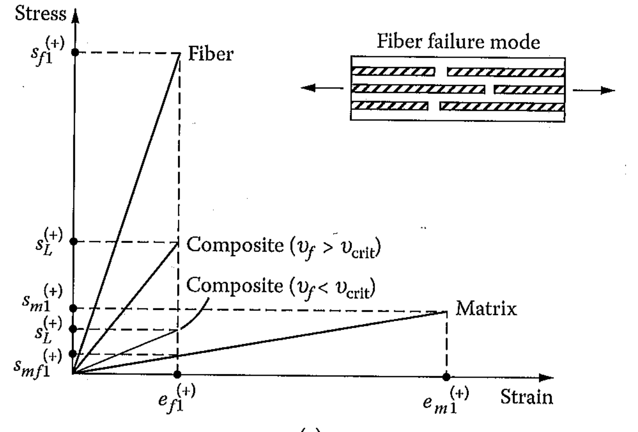

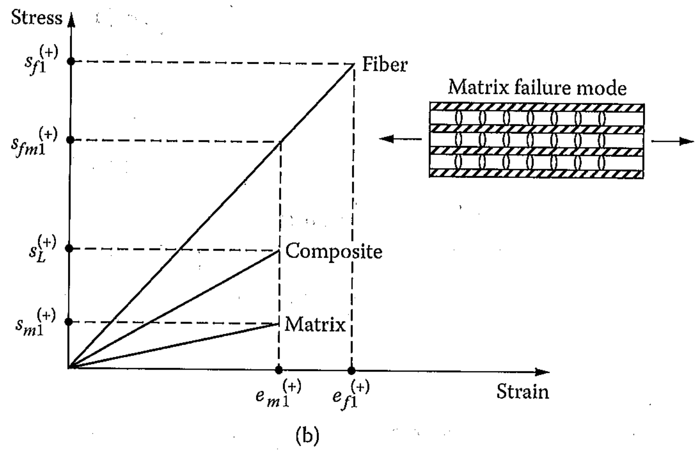

FIGURE 4.9
Representative stress–strain curves for typical fiber, matrix, and composite materials. (a) Matrix failure strain greater than fiber failure strain; (b) fiber failure strain greater than matrix failure strain.

Once the fibers fail in composites having $\upsilon_f < \upsilon_{fcrit}$, however, the remaining cross-sectional area of matrix that can support the load is such that

$$s_L^{(+)} = s_{m1}^{(+)}\upsilon_m = s_{m1}^{(+)}(1-\upsilon_f) \tag{4.23}$$

As shown in figure 4.10(a), equation (4.21) and equation (4.23) intersect at

$$\upsilon_{fmin} = \frac{s_{m1}^{(+)} - s_{mf1}^{(+)}}{s_{f1}^{(+)} - s_{mf1}^{(+)} + s_{m1}^{(+)}} \tag{4.24}$$

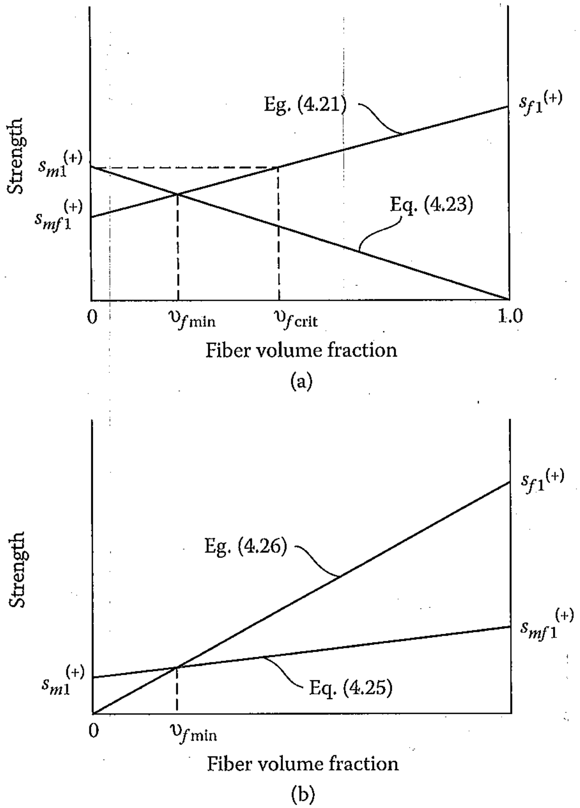

FIGURE 4.10
Variation of composite longitudinal tensile strength with fiber volume fraction for composite having: (a) Matrix failure strain greater than fiber failure strain; (b) fiber failure strain greater than matrix failure strain.

For practical composites, however, $\upsilon_{f\text{crit}}$, is generally less than 5%. Since $\upsilon_{f\min} < \upsilon_{f\text{crit}}$, both of these values must be much smaller than the actual fiber volume fraction of the composite, and the composite longitudinal strength for the case of figure 4.9(a) would therefore be given by equation (4.21).

For the case described in figure 4.9(b), composite failure may be defined in two ways, depending on whether we choose to use fiber failure or matrix failure as the criterion. If matrix failure is the criterion, composite failure will occur at the strain level corresponding to the matrix tensile failure strain, $e_{ml}^{(+)}$. Thus, when the matrix stress reaches the matrix tensile

strength, $s_{ml}^{(+)}$, the fiber stress reaches the value $s_{fm1}^{(+)} = E_{f1}e_{m1}^{(+)}$, the composite stress reaches the composite strength, $s_L^{(+)}$, and equation (3.19) becomes

$$s_L^{(+)} = s_{fm1}^{(+)}\upsilon_f + s_{m1}^{(+)}(1-\upsilon_f) \tag{4.25}$$

As with equation (4.21), this equation only has a physical meaning for a certain range of fiber volume fractions. As shown in figure 4.9(b), if the fibers could still withstand additional loading after matrix failure, the fiber strain may reach the fiber failure strain, $e_{f1}^{(+)}$. Due to the matrix failure, however, the remaining load-bearing area of fibers is such that the composite strength is now given by

$$s_L^{(+)} = s_{f1}^{(+)}\upsilon_f \tag{4.26}$$

As shown in figure 4.10(b), and equations (4.25) and (4.26) intersect at

$$\upsilon_{f\min} = \frac{s_{m1}^{(+)}}{s_{f1}^{(+)} - s_{fm1}^{(+)} + s_{m1}^{(+)}} \tag{4.27}$$

Thus, for $\upsilon_f < \upsilon_{f\min}$, the composite strength would be given by equation (4.25), and for $\upsilon_f > \upsilon_{f\min}$ the composite strength would be given by equation (4.26). For practical composites, however, $\upsilon_{f\min}$ is much smaller than the actual fiber volume fraction, so the composite longitudinal strength for the case of figure 4.9(b) would be given by equation (4.26).

Of the three assumptions made at the beginning of this section, the weakest one is that all fibers in the composite have the same strength, $s_{f1}^{(+)}$. As shown in figure 4.8, fiber strength is not uniform, and some fibers fail at stresses well below the ultimate composite strength. In addition, fiber strength decreases with increasing fiber length due to the increased probability of imperfections in the fiber. Various statistical models have been proposed for the sequence of events beginning with the first fiber failure and culminating with overall composite failure [52,53]. Such analyses are beyond the scope of this book, however, and the reader is referred to the article by Rosen [54] for a review of the various models.

While the assumption regarding linear elastic behavior up to failure is not valid for many ductile matrix materials, the errors generated by this assumption are believed to be small. For example, the contribution of the matrix strength to the composite strength in equation (4.21) is small, and the matrix strength does not appear at all in equation (4.26). If the matrix has yielded before or during fiber failure, the term s_{mfi} in equation (4.21), equation (4.22), and equation (4.24) can be replaced by the matrix yield strength, s_y. Excellent agreement has been reported between equation (4.21) modified in this way, and experimental results for a tungsten fiber/copper matrix system over a wide range of fiber volume fractions [55].

It has long been assumed that the models for longitudinal tensile strength cannot be used for longitudinal compressive strength, because the modes of failure are different. This assumption has been supported by observed differences in measured tensile and compressive strengths, as shown in table 4.1. Accurate measurement of the intrinsic compressive strength has proved to be very difficult, however, and test results to date typically depend on specimen geometry and/or test method. Whitney [56] has pointed out that the failure mode is the key issue because different compression test methods may produce different failure modes. Whether the failure mode in the test is the same as the failure mode in the composite structure being designed is another question. There appears to be three basic longitudinal compression failure modes, which are shown schematically in figure 4.11:

1. Microbuckling of fibers in either shear or extensional mode
2. Transverse tensile rupture due to Poisson strains
3. Shear failure of fibers without buckling

Variations on these basic mechanisms have also been observed. For example, the shear mode of fiber microbuckling (fig. 4.11) often leads to "shear crippling" due to kink band formation [51,57]. Although these problems make it difficult to assess the accuracy of various micromechanics models for compressive strength, several representative models will be summarized.

Mechanics of materials models for local buckling or microbuckling of fibers in the matrix have been developed by Rosen [58] and Schuerch [59]. It is assumed that fiber buckling occurs in either the extensional mode, where fibers buckle in an out-of-phase pattern and the matrix is extended or compressed, or the shear mode, where fibers buckle in an in-phase pattern and the matrix is sheared (fig. 4.11). Two-dimensional models were used, with the fibers represented as plates separated by matrix blocks. By the energy method, the work done by external forces during deformation, W, is equal to the corresponding change in the strain energy of the fibers, ΔU_f, plus the change in the strain energy of the matrix, ΔU_m:

$$\Delta U_f + \Delta U_m = W \tag{4.28}$$

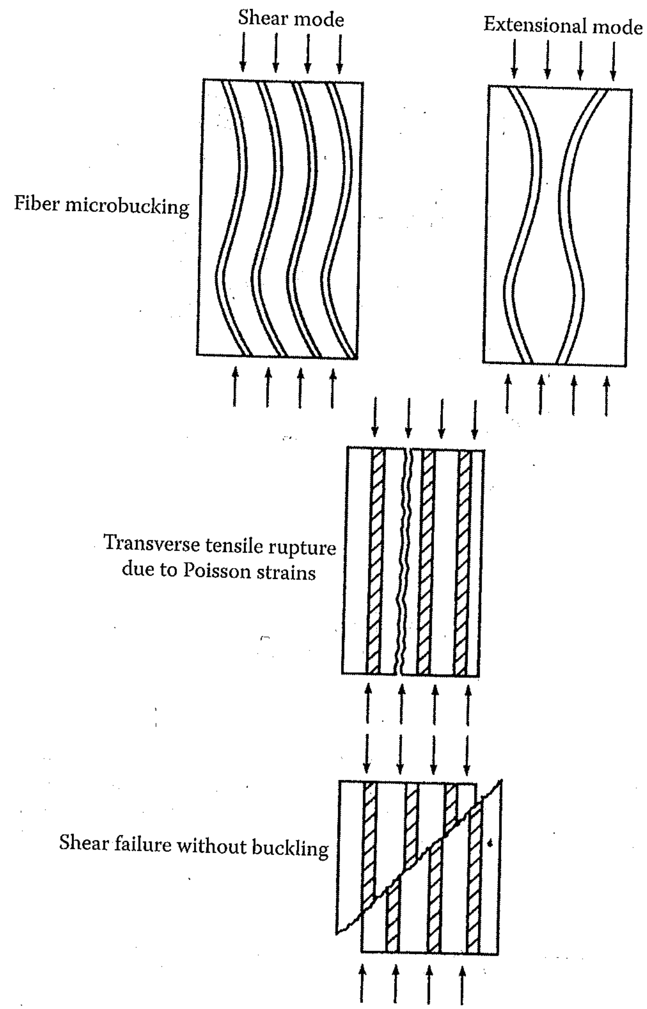

FIGURE 4.11
Three possible failure modes for longitudinal compressive loading of a unidirectional composite.

Assuming a sinusoidally buckled shape, the buckling stress (or compressive strength) for the extensional, or out-of-phase mode, was found to be

$$s_L^{(-)} = 2\upsilon_f[\upsilon_f E_m E_f / 3(1-\upsilon_f)]^{1/2} \tag{4.29}$$

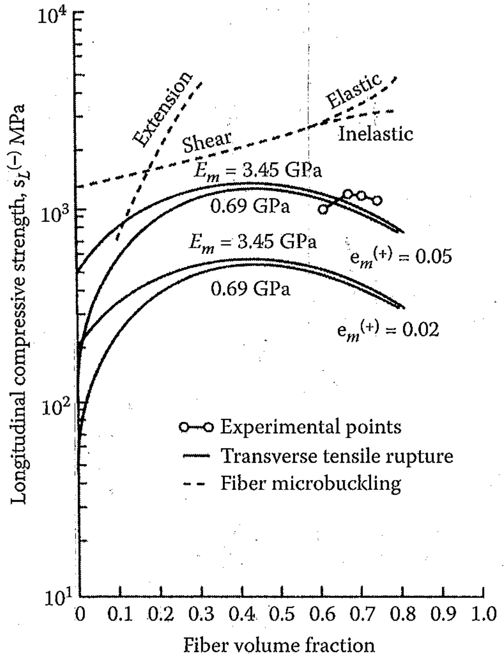

FIGURE 4.12
Variation of predicted compressive strength of glass/epoxy with fiber volume fraction for fiber microbuckling and transverse tensile rupture modes of failure. (From Agarwal, B.D. and Broutman, L.J. 1990. *Analysis and Performance of Fiber Composites*, 2d ed., John Wiley & Sons, Inc., New York. Copyright 1990, John Wiley & Sons, Inc. Reprinted by permission of John Wiley & Sons, Inc.)

whereas the buckling stress for the shear, or in-phase mode, was found to be

$$s_L^{(-)} = G_m/(1-\upsilon_f) \tag{4.30}$$

The extensional mode turns out to be important only for very low fiber volume fractions, where it predicts the lowest buckling stress and is not important for practical composites (fig. 4.12). While the shear mode gives the lowest buckling stress over the range of practical fiber volume fractions, it overpredicts considerably by comparison with test results. One way to reduce the buckling stress predicted by equation (4.30) is to take into account the possible inelastic deformation of the matrix material by using a reduced value of the matrix shear modulus, G_m, but predictions still tend to be too high. The nonlinear model of Hahn and Williams [57]

includes the effects of initial fiber curvature and material nonlinearity, and reasonable predictions of compressive strength for graphite/epoxy were reported. Greszczuk [60] has shown that if the matrix shear modulus is high enough, the mode of failure shifts from microbuckling to compressive failure of the reinforcement. Since advanced composites tend to have high modulus matrix materials, this may explain why attempts to apply microbuckling failure theories to these materials have not succeeded. For such cases Greszczuk recommended that equation (4.21) be used with $s_{f1}^{(-)}$ in place of $s_{f1}^{(+)}$. It should be added, however, that this conclusion was based on tests of laminates consisting of aluminum strips bonded together with urethane or epoxy resins. The difficulty in measurement of fiber compressive strength, $s_{f1}^{(-)}$, may preclude the use of this model for fiber composites.

A model for transverse tensile rupture due to Poisson strains (fig. 4.11) has been presented by Agarwal and Broutman [61]. The model is based on the application of the Maximum Strain Criterion to the tensile transverse Poisson strain under longitudinal compressive loading. Under the applied longitudinal stress, σ_1, the resulting transverse Poisson strain is

$$\varepsilon_2 = -\nu_{12}\varepsilon_1 = -\nu_{12}\frac{\sigma_1}{E_1} \tag{4.31}$$

Thus, when the Poisson strain $\varepsilon_2 = e_T^{(+)}$, the corresponding longitudinal stress is $\sigma_1 = s_L^{(-)}$, and the compressive strength is

$$s_L^{(-)} = \frac{E_1 e_T^{(+)}}{\nu_{12}} \tag{4.32}$$

As shown in figure 4.12, equation (4.32) shows better agreement with measured compressive strengths of glass/epoxy than the microbuckling theories do [61].

Failure of the fibers in direct shear due to the maximum shear stress $\tau_{max} = s_L^{(-)}/2$ at an angle of 45° to the loading axis is a third possible failure mode under longitudinal compression (fig. 4.11). Hull [51] reports good agreement with experimental data for graphite/epoxy when the maximum shear stress is given by a rule of mixtures, so that the compressive strength is

$$s_L^{(-)} = 2(s_{f12}\upsilon_f + s_{m12}\upsilon_m) \tag{4.33}$$

where s_{f12} and s_{m12} are the shear strengths of fiber and matrix, respectively. The direct shear mode of failure for graphite/epoxy has been several other publications as well [62,63]. For example, Crasto and Kim [63] have used a novel minisandwich beam to attain shear failure of the fibers in the composite facing without buckling — the resulting compressive strengths are much higher than those obtained with conventional compression testing.

A number of other factors have been shown to affect longitudinal compressive strength, and this continues to be a very active research area. For example, although the fiber/matrix interfacial strength does not appear in any of the equations presented here, it would appear to be very important in the case of transverse tensile rupture due to Poisson strains. The experiments of Madhukar and Drzal [64] have shown that the compressive strength of graphite/epoxy is strongly related to the interfacial shear strength, and that fiber surface treatments that improve the interfacial shear strength also improve the compressive strength.

4.3.2 Transverse Strength

Since failure of the lamina under transverse tension occurs at such low stresses (table 4.1), this mode of failure is generally the first to occur. In laminates, the so-called "first ply failure" is generally due to transverse tension. The low value of the transverse tensile strength, $s_T^{(+)}$, and the corresponding transverse failure strain, $e_T^{(+)}$, are due to strain concentration in the matrix around the fibers, as shown in equation (4.34):

$$e_T^{(+)} = \frac{e_{m2}^{(+)}}{F} = \frac{e_m^{(+)}}{F} \tag{4.34}$$

where $e_{m2}^{(+)} = e_m^{(+)}$, the matrix tensile failure strain (matrix is assumed to be isotropic) and F is the strain concentration factor ($F > 1$).

Thus, the strain concentration causes the composite transverse tensile failure strain to be less than the matrix failure strain. The strain concentration factor is more appropriate than the stress concentration factor here because the stress–strain relationships for transverse loading are often nonlinear, reflecting the nonlinear behavior of many matrix materials. However, if linear behavior to failure can be assumed, the corresponding transverse strength is

$$s_T^{(+)} = \frac{E_2 s_m^{(+)}}{E_m F} \tag{4.35}$$

It is assumed here that the fiber is perfectly bonded to the matrix, so in composites having poor interfacial strength, the composite transverse

strength would be less than that predicted by equation (4.35). For example, de Kok and Peijs [65] conducted experiments and incorporated an interfacial model in a finite element micromechanics model to show that, although the fiber/matrix interface does not affect the transverse modulus, it has a significant effect on the transverse strength. More specifically, it was found that the transverse strength increases in proportion to the interfacial bond strength when the interfacial bond failure is the dominant mode of failure, but this proportionality does not hold when matrix failure dominates.

A mechanics of materials approximation for the strain concentration factor has been developed by Kies [66], who considered an element in a transversely loaded lamina, as shown in figure 4.13(a). For the shaded

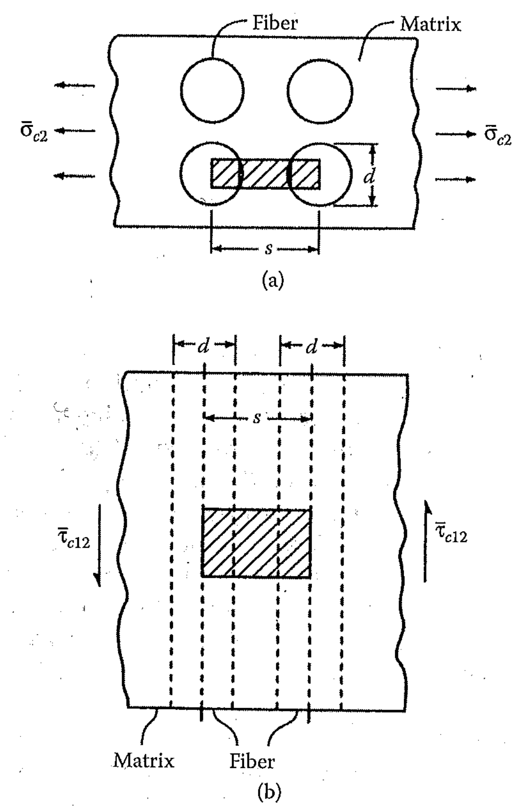

FIGURE 4.13
(a) Mechanics of materials model for strain concentration under transverse loading. (b) Mechanics of materials model for strain concentration under in-plane shear loading.

strip shown in figure 4.13(a), the total elongation is found by summing the deformations in the fiber and matrix

$$\bar{\delta}_{c2} = \bar{\delta}_{f2} + \bar{\delta}_{m2} = s\bar{\varepsilon}_{c2} = d\bar{\varepsilon}_{f2} + (s-d)\bar{\varepsilon}_{m2} \tag{4.36}$$

where the symbols are defined in section 3.2.2 and figure 4.13(a). For the series arrangement of fiber and matrix materials in the shaded strip, it is assumed that the stresses in composite, matrix, and fiber are equal and that each material satisfies Hooke's law (eqs. [3.34]), as in section 3.2.2. Equation (4.36) can then be written as

$$s\bar{\varepsilon}_{c2} = \left(d\frac{E_{m2}}{E_{f2}} + s - d \right)\bar{\varepsilon}_{m2} \tag{4.37}$$

which can be rearranged to give the expression for the strain concentration factor

$$F = \frac{\bar{\varepsilon}_{m}}{\bar{\varepsilon}_{c2}} = \frac{1}{\frac{d}{s}\left[\frac{E_m}{E_{f2}} - 1\right] + 1} \tag{4.38}$$

where the subscript "2" for matrix properties has been dropped due to the assumption of isotropy. Recall from equation (3.10) and equation (3.12) that the ratio of fiber diameter to fiber spacing, d/s, is related to the fiber volume fraction, υ_f. For example, from substitution of the properties listed in equations (3.29) in equation (3.12) and equation (4.38), the strain concentration factor for a triangular array of E-glass fibers in an epoxy matrix ($\upsilon_f = 0.45$) is $F = 3.00$. This value is in good agreement with experimentally determined values based on the ratio of matrix failure strain to transverse composite failure strain or the ratio of matrix yield strain to transverse composite yield strain [67]. A slightly higher value is predicted by a finite difference solution of the theory of elasticity model [68].

It is important to note that according to equation (4.38), the strain concentration factor increases with increasing υ_f and increasing E_{f2}. For example, the variation of F with fiber volume fraction is shown in figure 4.14 for $E_m/E_{f2} << 1$ [69]. The sharp rise in F for $\upsilon_f > 0.6$ is particularly noteworthy. Thus, as we strive to improve the composite longitudinal properties by using higher fiber volume fractions and higher modulus fibers, we pay the penalty of lower composite transverse strength!

The same method outlined above can be used to estimate the transverse compressive strength, $s_T^{(-)}$, by replacing the tensile strains or strengths

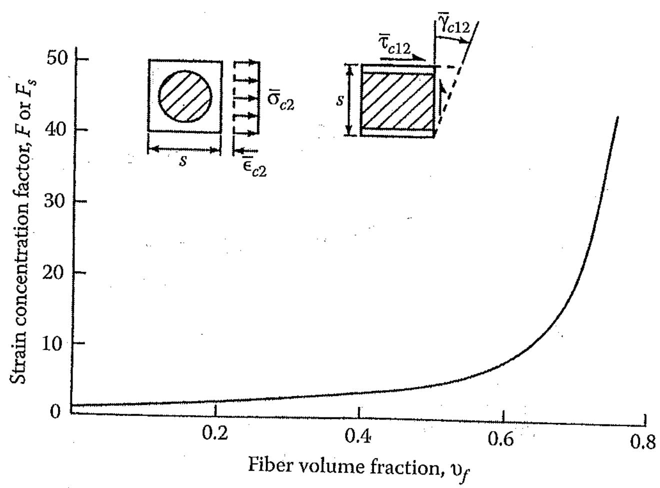

FIGURE 4.14
Variation of strain concentration factor F or F_s with fiber volume fraction. Valid for F when E_m/E_{f2} « 1 and for F_s when G_m/G_{f12} « 1. (From Chamis, C.C 1974. In Broutman, L.J. ed., *Composite Materials*, vol. 5, *Fracture and Fatigue*, Chapter 3. Academic Press, New York. With permission.)

with the corresponding compressive strains or strengths. Alternatively, the corresponding matrix strength can be used as an upper bound on the composite strength, but the actual composite strength would be lower because of fiber/matrix interfacial bond failure, strain concentrations around fibers and/or voids, or longitudinal fiber splitting [70].

While substitution of equation (4.38) in equation (4.35) shows that $s_T^{(+)}$ decreases with increasing υ_f, there is some evidence in the literature that $s_T^{(+)}$ increases slightly with increasing υ_f. For example, de Kok and Meijer [71] studied the effect of fiber volume fraction on the transverse strength of glass/epoxy using experiments and finite element micromechanical models. Experiments and a finite element micromechanical model based on the von Mises failure criterion for the epoxy matrix showed that the transverse strength of the composite increased slightly with increasing fiber volume fraction (fig. 4.15), but since the transverse modulus, E_2, also increases with increasing υ_f, the transverse failure strain decreased with increasing υ_f (fig. 4.16). According to the von Mises yield criterion, yielding occurs in the matrix when the equivalent axial stress or von Mises stress

$$\sigma_{eq} = \frac{1}{\sqrt{2}}\sqrt{(\sigma_a - \sigma_b)^2 + (\sigma_b - \sigma_c)^2 + (\sigma_c - \sigma_a)^2} \tag{4.39}$$

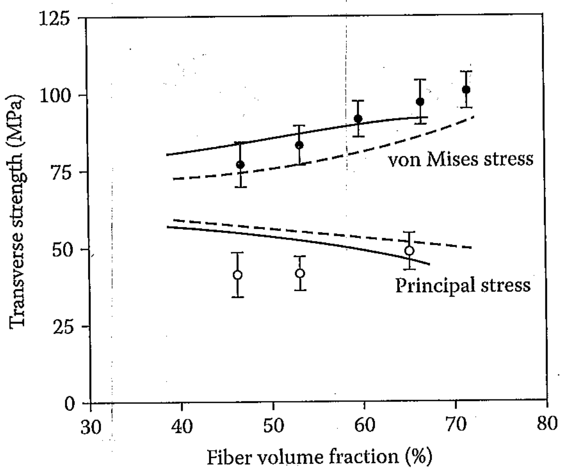

FIGURE 4.15
Transverse strength of E-glass/epoxy composite as a function of fiber volume fraction, as measured in tension (o) and three point bending (•), and predicted with the square (solid lines) and hexagonal (dotted lines) fiber packing models, using a von Mises criterion and an ultimate stress criterion. (From de Kok, J.M.M. and Meijer, H.E.H. 1999. *Composites Part A: Applied Science and Manufacturing*, 30, 905–916. With permission.)

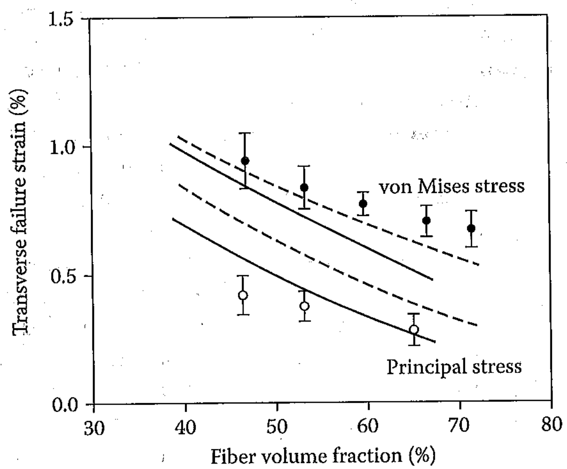

FIGURE 4.16
Transverse failure strain of E-glass/epoxy composite as a function of fiber volume fraction, as measured in tension (o) and three point bending (•), and predicted with the square (solid lines) and hexagonal (dotted lines) fiber packing models, using a von Mises criterion and an ultimate stress criterion. (From de Kok, J.M.M. and Meijer, H.E.H. 1999. *Composites Part A: Applied Science and Manufacturing*, 30, 905–916. With permission.)

reaches the uniaxial yield strength of the matrix material, where σ_a, σ_b, and σ_c are the three principal stresses in the matrix. The corresponding predicted transverse strength decreased with increasing v_f when only the ultimate principal stress in the matrix was considered in the micromechanics model. In addition, the predicted transverse strength based on the von Mises criterion was significantly higher than that predicted by the ultimate principal stress model (fig. 4.15). So it appears that the predicted transverse strength based on the 1-D stress model described in equation (4.34) to equation (4.38) is conservative by comparison with the corresponding prediction based on the actual triaxial state of stress and the von Mises failure criterion.

4.3.3 In-Plane Shear Strength

The in-plane shear strength, s_{LT}, can also be estimated using the procedure outlined in the previous section. For the shaded element shown in figure 4.13(b), the expression analogous to equation (4.36) for the in-plane shear strain is

$$s\bar{\gamma}_{c12} = d\bar{\gamma}_{f12} + (s-d)\bar{\gamma}_{m12} \tag{4.40}$$

and the in-plane shear strain concentration factor is

$$F_s = \frac{\bar{\gamma}_{m12}}{\bar{\gamma}_{c12}} = \frac{1}{\dfrac{d}{s}\left[\dfrac{G_{m12}}{G_{f12}} - 1\right] + 1} \tag{4.41}$$

where

$\bar{\gamma}_{m12}$ = average matrix in-plane shear strain
$\bar{\gamma}_{c12}$ = average composite in-plane shear strain
$\bar{\gamma}_{f12}$ = average fiber in-plane shear strain
G_{f12} = fiber in-plane shear modulus

Note that this equation has the same form as equation (4.38). Thus, figure 4.14 also gives the variation of F_s with υ_f when $G_m/G_{f12} << 1$, and the previous comments regarding the effect of υ_f on F are also valid for F_s. The other necessary equations are obtained by replacing the tensile strains or strengths in equation (4.34) and equation (4.35) with the corresponding in-plane shear strains or strengths. Again, the matrix shear strength can be used as an upper bound on the composite shear strength, as the actual composite strength would be lower for the same reasons mentioned in the previous section.

4.3.4 Multiaxial Strength

Section 4.3.1 to section 4.3.3 have summarized micromechanical models for prediction of the five basic unidirectional lamina strengths, and most of the micromechanical strength modeling efforts have been focused in these areas. However, micromechanical models have also been used to evaluate multiaxial failure criteria such as those described in section 4.2. For example, Zhu, Sankar, and Marrey [72] developed finite element unit cell micromechanics models and used them to evaluate the maximum stress and Tsai–Wu criteria as well as the combination of Tsai–Wu and maximum stress criteria for several biaxial loading conditions on a unidirectional composite. The approach was referred to as a direct micromechanics method (DMM). Two types of failure criteria for the fiber and matrix materials were employed in the DMM for predicting failure in each element of the model: (a) maximum principal stress criterion and (b) von Mises criterion, while fiber/matrix interfacial failure at the element level was modeled using the maximum tensile interfacial stress and the maximum interfacial shear stress. Failure envelopes were generated using the DMM and compared with the corresponding failure envelopes that were generated using the applied macromechanical stresses in the Tsai–Wu criterion, the Maximum Stress Criterion, the Maximum Strain Criterion, and the combined Tsai–Wu and maximum stress criteria. Figure 4.17 shows a comparison of failure envelopes from DMM with those from the Tsai–Wu and maximum stress and maximum strain criteria. For the case shown in figure 4.17, the DMM prediction agrees best with the Tsai–Wu prediction. From all the different cases examined, it was found that the combination of the Tsai–Wu and maximum stress criteria led to the most conservative failure envelope in the biaxial stress space, and that the failure criteria for the matrix and the fiber/matrix interface played dominant roles in the failure criteria for the composite. For off-axis tensile test models, the Tsai–Wu criterion showed the best agreement with the DMM approach for fiber orientations in the range $0 < \theta < 30°$, the Maximum Stress Criterion gave the best agreement in the range $60° < \theta < 90°$, and the criterion that gave the lowest strength prediction of the two criteria worked best in the range $30° < \theta < 60°$.

In conclusion, only the basics of micromechanical strength prediction have been discussed here. More detailed micromechanics analyses of strength under other types of loading such as interlaminar shear and

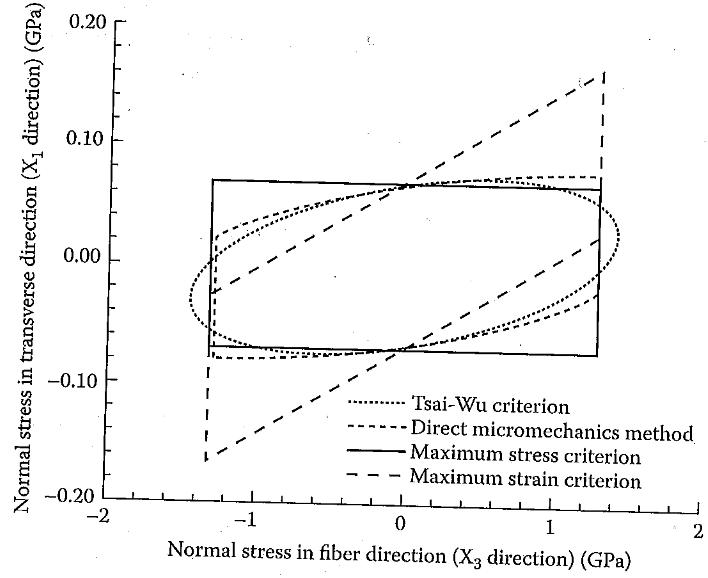

FIGURE 4.17
Comparison of results from DMM, Tsai–Wu criterion, Maximum Stress Criterion, and Maximum Strain Criterion in the prediction of failure envelopes for a unidirectional composite under biaxial loading. (From Zhu, H., Sankar, B.V., and Marrey, R.V. 1998. *Journal of Composite Materials*, 32, 766–782. With permission.)

flexure as well as micromechanical effects of voids and residual stresses on strength have been summarized by Chamis [69].

EXAMPLE 4.5

Determine the longitudinal and transverse tensile strengths of the carbon/epoxy material described in example 3.1, example 3.2, and example 3.4 if the tensile strengths of fiber and matrix materials are 2413 and 103 MPa, respectively.

Solution. The fiber tensile failure strain is

$$e_{f1}^{(+)} = \frac{s_{f1}^{(+)}}{E_{f1}} = \frac{2.413}{220} = 0.011$$

The matrix tensile failure strain is

$$e_m^{(+)} = \frac{s_m^{(+)}}{E_m} = \frac{0.103}{3.45} = 0.03$$

Thus, the material fails as described in figure 4.9(a) at a strain level of $e_{f1}^{(+)} = 0.011$. Since $\upsilon_f = 0.506$ and $\upsilon_m = 0.482$, from example 3.1, the composite longitudinal tensile strength is given by equation (4.21):

$$\begin{aligned} s_L^{(+)} &= s_{f1}^{(+)}\upsilon_f + s_{mf1}\upsilon_m \\ &= s_{f1}^{(+)}\upsilon_f + E_m e_{f1}^{(+)}\upsilon_m \\ &= 2413(0.506) + 3450(0.011)(0.482) \\ &= 1239 \text{ MPa } (180{,}000 \text{ psi}) \end{aligned}$$

Note that the matrix contribution here is only 18.3 MPa out of 1239 MPa or about 1.5%.

The strain concentration factor for the calculation of the transverse tensile strength is given by the equation (4.38):

$$F = \frac{1}{\frac{d}{s}\left[\frac{E_m}{E_{f2}} - 1\right] + 1} = \frac{1}{\frac{0.0127}{0.0158}\left[\frac{3.45}{13.79} - 1\right] + 1} = 2.52$$

If linear elastic behavior to failure can be assumed, the transverse tensile strength is given by equation (4.35).

$$s_T^{(+)} = \frac{E_2 S_m^{(+)}}{E_m F} = \frac{5.65(103)}{3.45(2.52)} = 66.9 \text{MPa } (9703 \text{ psi})$$

4.4 Problems

1. An orthotropic lamina has the following properties:

$E_1 = 160$ GPa $\quad s_L^{(+)} = 1800$ MPa
$E_2 = 10$ GPa $\quad s_L^{(-)} = 1400$ MPa
$\nu_{12} = 0.3$ $\quad s_T^{(+)} = 40$MPa
$G_{12} = 7$ GPa $\quad s_T^{(-)} = 230$ MPa
$s_{LT} = 100$ MPa

Construct the failure surfaces in the $\sigma_1 - \sigma_2$ stress space for this material according to the (a) Maximum Stress Criterion, (b) Maximum Strain Criterion, and (c) Tsai–Hill Criterion.

2. Using the material properties from problem 1 and assuming that the stiffnesses are the same in tension and compression, determine the allowable off-axis shear stress, τ_{xy}, at $\theta = 45°$ (refer to fig. 4.5) according to the *(a)* Maximum Stress Criterion, *(b)* Maximum Strain Criterion, and *(c)* Tsai–Hill Criterion. Compare and discuss the results and check both positive and negative values of τ_{xy}.

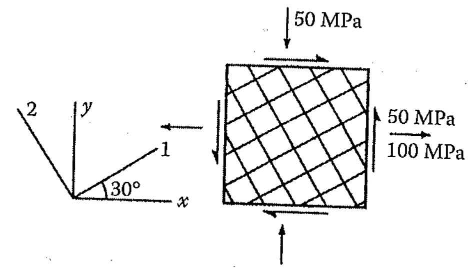

FIGURE 4.18
Stresses acting on element of balanced orthotropic lamina.

3. An element of a balanced orthotropic lamina is under the state of stress shown in figure 4.18. The properties of the lamina are:

$E_1 = E_2 = 70$ GPa $\quad s_L^{(+)} = s_L^{(-)} = s_T^{(+)} = s_T^{(-)} = 560$ MPa
$\nu_{12} = \nu_{21} = 0.25$ $\quad s_{LT} = 25$MPa
$G_{12} = 5$ GPa

Using the Maximum Strain Criterion, determine whether or not failure will occur.

4. If some of the compliances and strengths of an orthotropic lamina satisfy certain conditions, the Maximum Strain Criterion failure surface will intercept the horizontal axis at a point like $(\sigma_1, 0)$ instead of at $(s_L^{(-)}, 0)$ as shown in figure 4.19. Express these conditions in terms of an inequality.
5. An element of an orthotropic lamina having the properties given in problem 1 is subjected to an off-axis tensile test, as shown in figure 4.4. Using the Maximum Strain Criterion, determine the values of σ_x at failure and the mode of failure for each of the following values of the angle θ: *(a)* 2°, *(b)* 30°, *(c)* 75°.
6. Repeat problem 5 for an off-axis *compression* test.
7. A material having the properties given in problem 1 is subjected to a biaxial tension test, and the biaxial failure stress is found to be $\sigma_1 = \sigma_2 = 35$ MPa. Determine the Tsai–Wu interaction parameter F_{12} and then use the Tsai–Wu Criterion to determine...

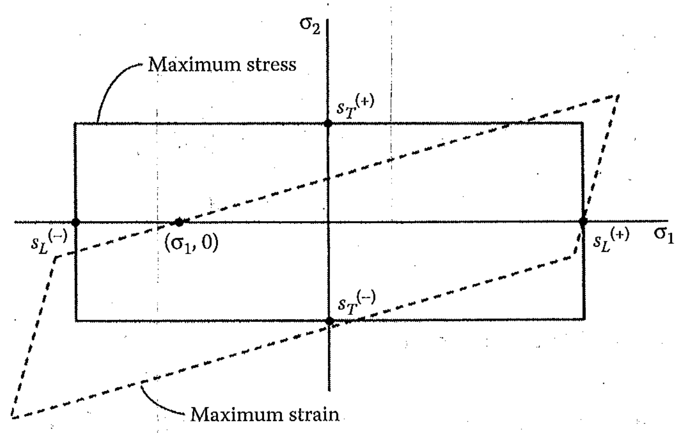

FIGURE 4.19
Example showing that intercepts for Maximum Strain Criterion failure surface are not always the same as those for Maximum Stress Criterion.

or not failure will occur for the stress condition σ_1 = 100 MPa, σ_2 = –50 MPa, τ_{12} = 90 MPa.

8. The Tsai–Wu interaction parameter F_{12} is determined from biaxial failure stress data. One way to generate a biaxial state of stress is by using a uniaxial 45° off-axis tension test. Derive the expression for F_{12} based on such a test, assuming that all the uniaxial and shear strengths are known.
9. Determine the longitudinal tensile strength of the hybrid carbon/aramid/epoxy composite described in problem 3 of chapter 3 and figure 3.19.
10. Compare and discuss the estimated longitudinal compressive strengths of Scotchply 1002 E-glass/epoxy based on (*a*) fiber microbuckling and (*b*) transverse tensile rupture. Assume linear elastic behavior to failure. For the epoxy matrix, assume E_m = 3.79 GPa, ν_m = 0.35.
11. An element of an orthotropic lamina is subjected to an off-axis shear stress, τ_{xy}, as shown in figure 4.5(a). Using the Tsai–Hill Criterion and assuming that the lamina strengths are the same in tension and compression, develop an equation relating the allowable value of τ_{xy} to the lamina strengths, s_L, s_T, and s_{LT}, and the fiber orientation θ.
12. A uniaxial off-axis tensile test is conducted as shown in figure 4.4. (a) Using the Tsai–Hill criterion and assuming that the lamina strengths are the same in tension and compression, develop an equation relating the applied stress, σ_x, to the lamina strengths s_L, s_T, and s_{LT}, and the lamina orientation, θ, and (b) using the result from part (a), for a unidirectional composite having strengths s_L = 1500 MPa, s_T = 100 MPa, s_{LT} = 70 MPa, and fiber orientation θ = 60°, determine whether or not an applied stress σ_x = 200 MPa would cause failure according to the Tsai–Hill criterion.
13. Using the Maximum Strain criterion and micromechanics, set up the equations for predicting the averaged isotropic strength of a randomly oriented continuous fiber composite. Your answer should be expressed in terms of the appropriate fiber and matrix properties and volume fractions, the variable fiber orientation angle θ, and the appropriate strengths of the corresponding unidirectional lamina that consists of the same fiber and matrix materials and volume fractions. In the micromechanics analysis, assume that the matrix failure strain is greater than the fiber failure strain (i.e., that the materials behave as shown in fig. 4.9[a]). Define all parameters used, but do not try to solve the equation.
14. Assuming that the failure mode for longitudinal compression of unidirectional E-glass/epoxy with v_f = 0.6 is transverse tensile rupture due to Poisson strains, (a) estimate the longitudinal compressive strength of this material, and (b) if the volume fraction of the material in part (a) is varied, what effect would this have on the longitudinal compressive strength?

References

1. Chamis, C.C. 1987. Simplified composite micromechanics thermal and moisture-related properties, in Weeton, J.W., Peters, D.M., and Thomas, K.L. eds. *Engineers' Guide to Composite Materials*, pp. 3-8–3-24. ASM International, Materials Park, OH.
2. Daniel, I.M. and Ishai, O. 1994. *Engineering Mechanics of Composite Materials.* Oxford University Press, New York.
3. Hashin, Z. 1983. Analysis of composite materials — A survey. *Journal of Applied Méchanics*, 50, 481–505.
4. Hashin, Z. 1980. Failure criteria for unidirectional fiber composites. *Journal of Applied Mechanics*, 47, 329–334.
5. Wu, E.M. 1974. Phenomenological anisotropic failure criterion, in Sendeckyj, G.P. ed., *Composite Materials*, vol. 2, *Mechanics of Composite Materials*, pp. 353–431. Academic Press, New York.
6. Sendeckyj, G.P. 1972. A brief survey of empirical multiaxial strength criteria for composites. *Composite Materials: Testing and Design (Second Conference)*, ASTM STP 497, pp. 41–51. American Society for Testing and Materials, Philadelphia, PA.

7. Chamis, C.C. 1969. Failure criteria for filamentary composites. *Composite Materials: Testing and Design*, ASTM STP 460, pp. 336–351. American Society for Testing and Materials, Philadelphia, PA.
8. Kaminski, B.E. and Lantz, R.B. 1969. Strength theories of failure for anisotropic materials. *Composite Materials: Testing and Design*, ASTM STP 460, pp. 160–169. American Society for Testing and Materials, Philadelphia, PA.
9. Franklin, H.G. 1968. Classical theories of failure of anisotropic materials. *Fiber Science and Technology*, 1(2), 137–150.
10. Tsai, S.W. 1984. A survey of macroscopic failure criteria for composite materials. *Journal of Reinforced Plastics and Composites*, 3, 40–62.
11. Christensen, R.M. 1997. Stress based yield/failure criteria for fiber composites. *International Journal of Solids and Structures*, 34(5), 529–543.
12. Zhu, H., Sankar, B.V., and Marrey, R.V. 1998. Evaluation of failure criteria for fiber composites using finite element micromechanics. *Journal of Composite Materials*, 32(8), 766–782.
13. Soden, P.D., Hinton, M.J., and Kaddour, A.S. 1998. A comparison of the predictive capabilities of current failure theories for composite laminates. *Composites Science and Technology*, 58(7), 1125–1254.
14. Soden, P.D., Hinton, M.J., and Kaddour, A.S. 1998. Lamina properties, lay-up configurations and loading conditions for a range of fibre-reinforced composite laminates. *Composites Science and Technology*, 58(7), 1011–1022.
15. Hinton, M.J. and Soden, P.D. 1998. Predicting failure in composite laminates: the background to the exercise. *Composites Science and Technology*, 58(7), 1001–1010.
16. Hinton, M.J., Kaddour, A.S., and Soden, P.D. 2002. A comparison of the predictive capabilities of current failure theories for composite laminates, judged against experimental evidence. *Composites Science and Technology*, 62(12–13), 1725–1797.
17. Soden, P.D., Hinton, M.J., and Kaddour, A.S. 2002. Biaxial test results for strength and deformation of a range of E-glass and carbon fibre reinforced composite laminates: Failure exercise benchmark data. *Composites Science and Technology*, 62(12–13), 1489–1514; Hinton, M.J., Kaddour, A.S., and Soden, P.D. 2002. Evaluation of failure prediction in composite laminates: background to 'part B' of the exercise. *Composites Science and Technology*, 62(12–13), 1481–1488.
18. Hinton, M.J., Kaddour, A.S., and Soden, P.D. 2002. Evaluation of failure prediction in composite laminates: background to 'part B' of the exercise. *Composites Science and Technology*, 62(12–13), 1481–1488.
19. Soden, P.D., Kaddour, A.S., and Hinton, M.J. 2004. Recommendations for designers and researchers resulting from the world-wide failure exercise. *Composites Science and Technology*, 64(3–4), 589–604.
20. Hinton, M.J., Kaddour, A.S., and Soden, P.D. 2004. A further assessment of the predictive capabilities of current failure theories for composite laminates: Comparison with experimental evidence. *Composites Science and Technology*, 64(3–4), 549–588.
21. Kaddour, A.S., Hinton, M.J., and Soden, P.D. 2004. A comparison of the predictive capabilities of current failure theories for composite laminates: Additional contributions. *Composites Science and Technology*, 64(3–4), 449–476.

22. Hinton, M.J., Kaddour, A.S., and Soden, P.D. 2004. Evaluation of failure prediction in composite laminates: Background to 'part C' of the exercise. *Composites Science and Technology*, 64(3–4), 321–327.
23. Hinton, M.J., Soden, P.D., and Kaddour, A.S. 2004. *Failure Criteria in Fibre-Reinforced Polymer Composites*. Elsevier, London.
24. Jenkins, C.F. 1920. Report on materials of construction used in aircraft and aircraft engines. Great Britain Aeronautical Research Committee.
25. Higdon, A., Ohlsen, E.H., Stiles, W.B., Weese, J.A., and Riley, W.F. 1976. *Mechanics of Materials*, 3d ed. John Wiley & Sons, New York.
26. Burk, R.C. 1983. Standard failure criteria needed for advanced composites. *Astronautics and Aeronautics*, 21(6), 58–62.
27. Pipes, R.B. and Cole, B.W. 1973. On the off-axis strength test for anisotropic materials. *Journal of Composite Materials*, 7, 246–256.
28. Jones, R.M. 1999. *Mechanics of Composite Materials*, 2nd ed. Taylor & Francis, Philadelphia, PA.
29. Waddoups, M.E. 1967. Advanced composite material mechanics for the design and stress analyst. General Dynamics. Fort Worth Division Report FZM-4763, Fort Worth, TX.
30. Hill, R. 1948. A theory of the yielding and plastic flow of anisotropic metals, in *Proceedings of the Royal Society of London, Series A*, 193, 281–297.
31. Azzi, V.D. and Tsai, S.W. 1965. Anisotropic strength of composites, in *Proceedings of the Society for Experimental Stress Analysis*, XXII(2), 283–288.
32. Tsai, S.W. 1968. Strength theories of filamentary structures, in Schwartz, R.T. and Schwartz, H.S. eds., *Fundamental Aspects of Fiber Reinforced Plastic Composites*, chapter 1, pp. 3–11. Wiley Interscience, New York.
33. Hoffman, O. 1967. The brittle strength of orthotropic materials. *Journal of Composite Materials*, 1, 200–206.
34. Tsai, S.W. and Wu, E.M. 1971. A general theory of strength for anisotropic materials. *Journal of Composite Materials*, 5, 58–80.
35. Goldenblat, I. and Kopnov, V.A. 1965. Strength of glass reinforced plastics in the complex stress state. *Mekhanika Polimerov*, 1, 70–78 (English translation: *Polymer Mechanics*, 1, 54–60 [1966]).
36. Wu, E.M. 1972. Optimal experimental measurements of anisotropic failure tensors. *Journal of Composite Materials*, 6, 472–489.
37. Tsai, S.W. and Hahn, H.T. 1980. *Introduction to Composite Materials*. Technomic Publishing Co., Lancaster, PA.
38. Zinoviev, P., Grigoriev, S.V., Lebedeva, O.V., and Tairova, L.R. 1998. Strength of multilayered composites under plane stress state. *Composites Science and Technology*, 58(7), 1209–1224.
39. Zinoviev, P.A., Lebedeva, O.V., and Tairova, L.R. 2002. Coupled analysis of experimental and theoretical results of the deformation and failure of laminated composites under a plane state of stress. *Composites Science and Technology*, 62(12–13), 1711–1723.
40. Bogetti, T.A., Hoppel, C.P.R., Harik, V.M., Newill, J.F., and Burns, B.P. 2004. Predicting the nonlinear response and progressive failure of composite laminates. *Composites Science and Technology*, 64(3–4), 329–342.
41. Bogetti, T.A., Hoppel, C.P.R., Harik, V.M., Newill, J.F., and Burns, B.P. 2004. Predicting the nonlinear response and progressive failure of composite

laminates: Correlation with experimental results. *Composites Science and Technology*, 64(3–4), 477–485.
42. Liu, K.S. and Tsai, S.W. 1998. A progressive quadratic failure criterion for a laminate. *Composites Science and Technology*, 58(7), 1023–1032.
43. Kuraishi, A., Tsai, S.W., and Liu, K.S. 2002. A progressive quadratic failure criterion. Part B. *Composites Science and Technology*, 62(12–13), 1683–1695.
44. Puck, A. and Schurmann, H. 1998. Failure analysis of FRP laminates by means of physically based phenomenological models. *Composites Science and Technology*, 58(7), 1045–1067.
45. Puck, A. and Schurmann, H. 2002. Failure analysis of FRP laminates by means of physically based phenomenological models. *Composites Science and Technology*, 62(12–13), 1633–1662.
46. Cuntze, R.G. and Freund, A. 2004. The predictive capability of failure mode concept-based strength criteria for multidirectional laminates. *Composites Science and Technology*, 64(3–4), 343–377.
47. Cuntze, R.G. 2004. The predictive capability of failure mode concept-based strength criteria for multidirectional laminates — part B. *Composites Science and Technology*, 64(3–4), 487–516.
48. Tennyson, R.C., MacDonald, D., and Nanyaro, A.P. 1978. Evaluation of the tensor polynomial failure criterion for composite materials. *Journal of Composite Materials*, 12, 63–75.
49. Weeton, J.W., Peters, D.M., and Thomas, K.L. eds. 1987. *Engineers' Guide to Composite Materials*. ASM International, Materials Park, OH.
50. Kelly, A. and Davies, G.J. 1965. The principles of the fibre reinforcement of metals. *Metallurgical Review*, 10, 1–77.
51. Hull, D. 1981. *An Introduction to Composite Materials*. Cambridge University Press, Cambridge, MA.
52. Rosen, B.W. 1964. Tensile failure of fibrous composites. *AIAA Journal*, 2, 1985–1991.
53. Zweben, C. and Rosen, B.W. 1970. A statistical theory of material strength with applications to composite materials. *Journal of Mechanics and Physics of Solids*, 18, 180–206.
54. Rosen, B.W. 1987. Composite materials analysis and design, in Reinhart, T.J. ed., *Engineered Materials Handbook*, vol. 1, *Composites*, Section 4. ASM International, Materials Park, OH.
55. Holister, G.S. and Thomas, C. 1966. *Fibre Reinforced Materials*. Elsevier Publishing Co., Ltd., New York.
56. Whitney, J.M. 1991. Failure modes in compression testing of composite materials, *How Concept Becomes Reality, Proceedings of 36th International SAMPE Symposium*, 36, pp. 1069–1078. Society for Advancement of Material and Process Engineering, Covina, CA.
57. Hahn, H.T. and Williams, J.G. 1986. Compression failure mechanisms in unidirectional composites, in Whitney, J.M. ed., *Composite Materials: Testing and Design (Seventh Conference)*, ASTM STP 893, pp. 115–139. American Society for Testing and Materials, Philadelphia, PA.
58. Rosen, B.W. 1965. Mechanics of composite strengthening. *Fiber Composite Materials*. American Society for Metals, Metals Park, OH.

59. Schuerch, H. 1966. Prediction of compressive strength in uniaxial boron fiber metal matrix composites. *AIAA Journal*, 4, 102–106.
60. Greszczuk, L.B. 1974. Microbuckling of lamina-reinforced composites, in Berg, C.A. et al. eds., *Composite Materials: Testing and Design (Third Conference)*, ASTM STP 546, pp. 5–29. American Society for Testing and Materials, Philadelphia, PA.
61. Agarwal, B.D. and Broutman, L.J. 1990. *Analysis and Performance of Fiber Composites*, 2d ed. John Wiley & Sons, Inc., New York.
62. Hancox, N.L. 1975. The compression strength of unidirectional carbon fibre reinforced plastics. *Journal of Materials Science*, 10(2), 234–242.
63. Crasto, A.S. and Kim, R.Y. 1991. Compression strengths of advanced composites from a novel mini-sandwich beam. *SAMPE Quarterly*, 22(3), 29–39.
64. Madhukar, M.S. and Drzal, L.T. 1990. Effect of fiber-matrix adhesion on longitudinal compressive properties of graphite/epoxy composites, in *Proceedings of the American Society for Composites Fifth Technical Conference*, pp. 849–858. Technomic Publishing Co., Lancaster, PA.
65. de Kok, J.M.M. and Peijs, T. 1999. Deformation, yield and fracture of unidirectional composites in transverse loading: 2. Influence of fibre-matrix adhesion. *Composites Part A: Applied Science and Manufacturing*, 30(7), 917–932.
66. Kies, J.A. 1962. Maximum strains in the resin of fiber glass composites. U.S. Naval Research Laboratory Report No. 5752.
67. Gibson, R.F. 1975. Elastic and dissipative properties of fiber reinforced composite materials in flexural vibration. Ph.D. Dissertation, University of Minnesota.
68. Adams, D.F. and Doner, D.R. 1967. Transverse normal loading of a unidirectional composite. *Journal of Composite Materials*, 1, 152–164.
69. Chamis, C.C 1974. Micromechanics strength theories, in Broutman, L.J. ed., *Composite Materials*, vol. 5, *Fracture and Fatigue*, Chapter 3. Academic Press, New York.
70. Piggott, M.R. 1980. *Load Bearing Fibre Composites*. Pergamon Press Ltd., Oxford, England.
71. de Kok, J.M.M. and Meijer, H.E.H. 1999. Deformation, yield and fracture of unidirectional composites in transverse loading: 1. Influence of fibre volume fraction and test temperature. *Composites Part A: Applied Science and Manufacturing*, 30(7), 905–916.
72. Zhu, H., Sankar, B.V., and Marrey, R.V. 1998. Evaluation of failure criteria for fiber composites using finite element micromechanics. *Journal of Composite Materials*, 32, 766–782.

5

Analysis of Lamina Hygrothermal Behavior

5.1 Introduction

The analytical models for composite mechanical behavior presented up to now have been based on the assumption of constant environmental conditions. Composites are usually subjected to changing environmental conditions during both initial fabrication and final use, however, and it is important to be able to include the effects of such changes in the analysis. Among the many environmental conditions that may influence composite mechanical behavior, changes in temperature and moisture content are singled out for discussion here because of the particularly important effects they have on polymer matrix materials and those properties of polymer composites that are matrix dominated. Effects of temperature are usually referred to as "thermal" effects, whereas those of moisture are often referred to as "hygroscopic" effects. The word "hygrothermal" has evolved as a way of describing the combined effects of temperature and moisture.

There are two principal effects of changes in the hygrothermal environment on mechanical behavior of polymer composites:

1. Matrix-dominated properties such as stiffness and strength under transverse, off-axis, or shear loading are altered. Increased temperature causes a gradual softening of the polymer matrix material up to a point. If the temperature is increased beyond the so-called "glass transition" region (indicating a transition from glassy behavior to rubbery behavior), however, the polymer becomes too soft for use as a structural material (fig. 5.1). Plasticization of the polymer by absorbed moisture causes a reduction in the glass transition temperature, T_g, and a corresponding degradation of composite properties. As shown in figure 5.1, the glass transition temperature of the dry material is characterized by T_{go} (i.e., the "dry" T_g), and when the material is fully saturated with moisture content M_m, it is characterized by T_{gw} (the "wet" T_g). Saturation moisture contents of 3% to 4%

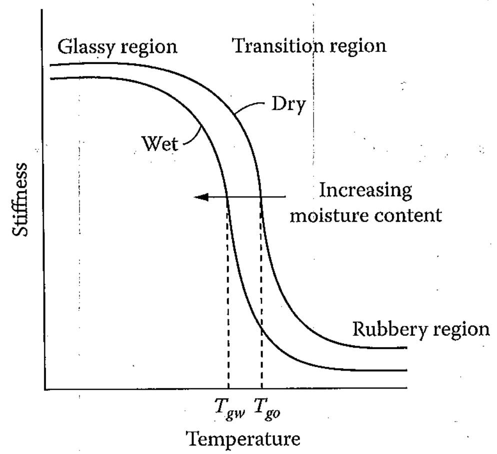

FIGURE 5.1
Variation of stiffness with temperature for a typical polymer showing the glass transition temperature, T_g, and the effect of absorbed moisture on T_g. Note: T_{g0} = "dry" T_g and T_{gw} = "wet" T_g.

by weight, and moisture-induced reductions in T_g on the order of 20% are typical for polymer matrix materials, as shown by the numerical data in table 5.1. Note also in table 5.1 that the maximum service temperature is typically well below the T_g, as properties such as stiffness become undesirably sensitive to temperature if the service temperature gets too close to the glass transition region.

2. Hygrothermal expansions or contractions change the stress and strain distributions in the composite. Increased temperature and/or moisture content causes swelling of the polymer matrix, whereas reduced temperature and/or moisture content causes contraction. Since the fibers are typically not affected as much by hygrothermal conditions, the swelling or contraction of the matrix is resisted by the fibers and residual stresses develop in the composite. A similar effect at the laminate level is due to differential expansions or contractions of constituent laminae.

This chapter is therefore concerned with analytical modeling of hygrothermal degradation of matrix-dominated properties and modification of the lamina stress–strain relationships to include hygrothermal effects. Micromechanical prediction of mechanical and thermophysical properties will also be discussed because of its importance in the analytical modeling of both effects.

TABLE 5.1
Hygrothermal Properties for Various Polymer Matrix Materials

Material	Supplier	Saturation Moisture Content, M_m (Weight %)	T_{go} (Dry) [°F (°C)]	T_{gw} (Wet) [°F (°C)]	Maximum Service Temperature (Dry) [°F (°C)]
Hexply® F655 bismaleimide	Hexcel	4.1	550(288)	400(204)	400(204)
Hexply 8551-7 epoxy	Hexcel	3.1	315(157)	240(116)	200(93)
Hexply 8552 epoxy	Hexcel	—	392(200)	309(154)	250(121)
Hexply 954-3A cyanate	Hexcel	—	400(204)	—	—
CyCom® 2237 polyimide	Cytec	4.4	640(338)	509(265)	550(208)
CyCom 934 epoxy	Cytec	—	381(194)	320(160)	350(177)
Avimid® R polyimide	Cytec	2.8	581(305)	487(253)	550(288)
Derakane® 411-350 vinylester	Ashland	1.5	250(120)	—	220(105)
Ultem® 2300 polyetherimide	General Electric	0.9	419(215)	—	340(171)
Victrex 150G polyetherether-ketone	Victrex plc	0.5	289(143)	—	356(180)

5.2 Hygrothermal Degradation of Properties

As evidence of hygrothermal degradation of properties, consider the data of Browning et al. [1], who tested graphite/epoxy composites and their epoxy matrix materials under various hygrothermal conditions. Figure 5.2 shows the stress–strain curves for a typical epoxy matrix material under the various combinations of temperature and absorbed moisture. The corresponding stress–strain curves for the graphite/epoxy composite under transverse loading are shown in figure 5.3. Note that the imposed hygrothermal conditions cause substantial reductions of both strength and stiffness in both cases, with the so-called "hot–wet" conditions (combined high temperature and high moisture content) generating the most severe degradation. Similar degradation was observed in the case of in-plane shear loading of the composite since the behavior is matrix dominated in both cases. On the other hand, the corresponding

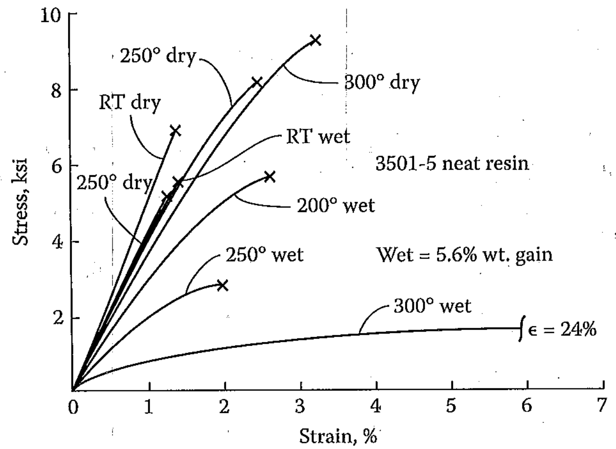

FIGURE 5.2
Stress–strain curves for 3501–5 epoxy resin at different temperatures and moisture contents. (From Browning, C.E., Husman, G.E., and Whitney, J.M. 1977. *Composite Materials: Testing and Design: Fourth Conference*, ASTM STP 617, pp. 481–496. American Society for Testing and Materials, Philadelphia, PA. Copyright, ASTM. Reprinted with permission.)

stress–strain curves for the composite under longitudinal loading showed little effect because longitudinal strength and stiffness are fiber dominated.

Another example of the hygrothermal sensitivity of matrix-dominated composite properties are the data of Gibson et al. [2], who used a vibrating beam method to measure the flexural moduli of several E-glass/polyester sheet-molding compounds after soaking at various times in a water bath. Table 5.2 gives a description of the materials, figure 5.4 shows the percent weight gain due to moisture pickup, and figure 5.5 shows the variation in modulus with soaking time. Composites having some continuous fibers and high fiber contents absorbed little moisture and showed negligible change in modulus with soaking time. On the other hand, composites having matrix-dominated behavior (those with chopped fibers only and low fiber contents) exhibited the most moisture pickup and the greatest reduction in modulus.

Considerable insight into the physics of temperature and moisture distribution in a material is gained from the analysis of Shen and Springer [3], who considered the 1-D distribution of temperature, T, and moisture concentration, c, in a plate of thickness, h, which is suddenly exposed on both sides to an environment of temperature, T_a, and moisture concentration, c_a (fig. 5.6). The temperature and moisture concentration are assumed to vary only through the thickness along the z direction and the initial

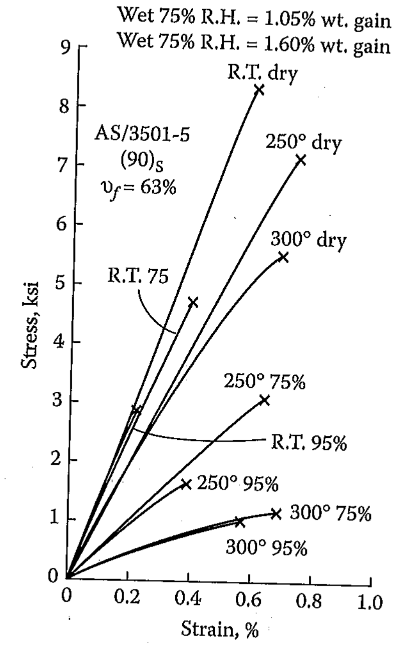

FIGURE 5.3
Stress–strain curves for AS/3501–5 graphite/epoxy composite under transverse loading at different temperatures and moisture contents. (From Browning, C.E., Husman, G.E., and Whitney, J.M. 1977. *Composite Materials: Testing and Design: Fourth Conference*, ASTM STP 617, pp. 481–496. American Society for Testing and Materials, Philadelphia, PA. Copyright, ASTM. Reprinted with permission.)

TABLE 5.2
Description of Composite Materials for Figure 5.4 and Figure 5.5

Material	Weight of Percentages of Constituents: Chopped E-Glass Fibers	Continuous E-Glass Fibers	Polyester Resin, Fillers, etc.
PPG SMC-R25[a]	25	0	75
PPG SMC-R65	65	0	35
PPG XMC-3	25	50 (±7.5°, X-pattern)	25
OCF SMC-R25[b]	25	0	75
OCF C20/R30	30	20 (aligned)	50

[a]Manufactured by PPG Industries, Fiber Glass Division, Pittsburgh, PA.
[b]Manufactured by Owens-Corning Fiberglas Corporation, Toledo, OH.
Source: From Gibson, R.F., Yau, A., Mende, E.W., and Osborn, W.E. 1982. *Journal of Reinforced Plastics and Composites*, 1(3), 225–241. With permission.

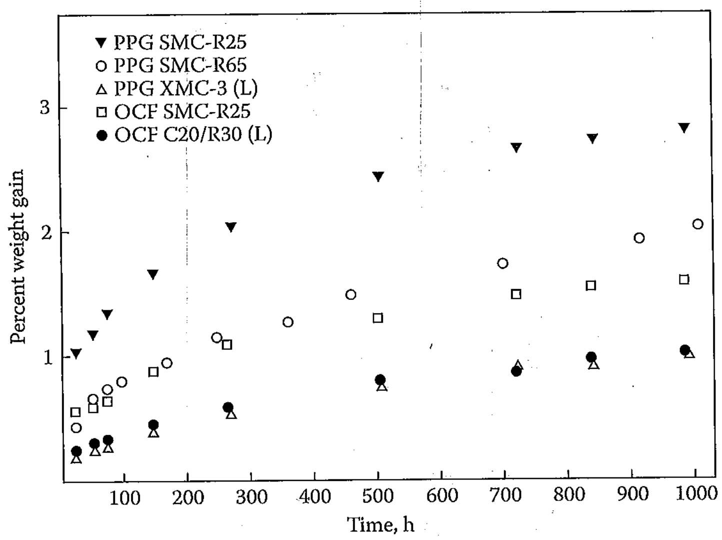

FIGURE 5.4
Percent weight gain due to moisture pickup vs. soaking time for several E-glass/polyester sheet-molding compounds. Materials described in table 5.2. (From Gibson, R.F., Yau, A., Mende, E.W., and Osborn, W.E. 1982. *Journal of Reinforced Plastics and Composites*, 1(3), 225–241. Reprinted by permission of Technomic Publishing Co.)

temperature, T_i, and initial moisture concentration, c_i, are assumed to be uniform. The temperature distribution is governed by the Fourier heat conduction equation:

$$\rho C\frac{\partial T}{\partial t}=\frac{\partial}{\partial z}K_z\frac{\partial T}{\partial z} \tag{5.1}$$

whereas the moisture distribution is governed by Fick's second law,

$$\frac{\partial c}{\partial t}=\frac{\partial}{\partial z}D_z\frac{\partial c}{\partial z} \tag{5.2}$$

where

ρ = density of material
C = specific heat of material
K_z = thermal conductivity of material along the z direction
D_z = mass diffusivity along the z direction
t = time

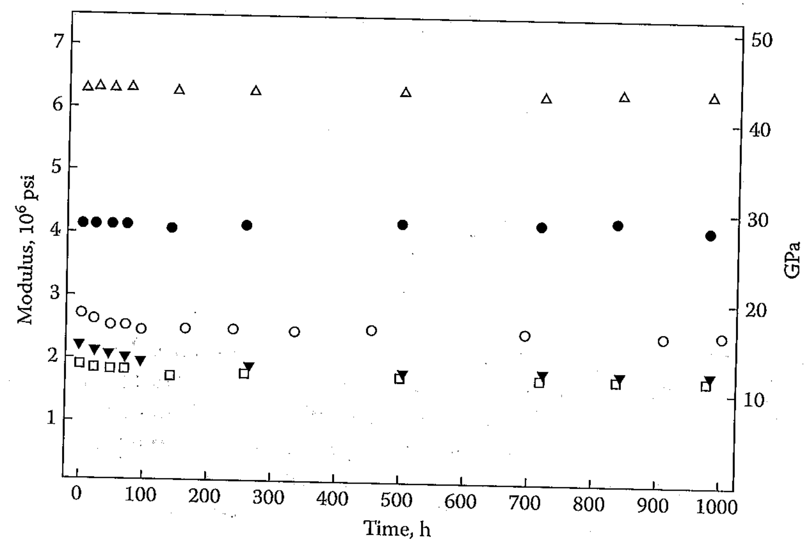

FIGURE 5.5
Variation of flexural modulus of several E-glass/polyester sheet-molding compounds with soaking time in distilled water at 21 to 24°C. Materials described in table 5.2 and in figure 5.4. (From Gibson, R.F., Yau, A., Mende, E.W., and Osborn, W.E. 1982. *Journal of Reinforced Plastics and Composites*, 1(3), 225–241. Reprinted by permission of Technomic Publishing Co.)

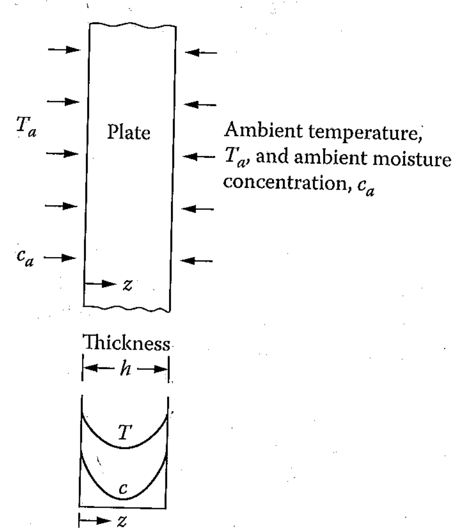

FIGURE 5.6
Schematic representation of temperature and moisture distributions through the thickness of a plate that is exposed to an environment of temperature, T_a, and moisture concentration, c_a, on both sides.

These equations are solved subject to the initial and boundary conditions,

$$\left.\begin{aligned} T &= T_i \\ c &= c_i \end{aligned}\right\} 0 < z < h, \quad t \le 0$$

$$\left.\begin{aligned} T &= T_a \\ c &= c_a \end{aligned}\right\} z = 0; \quad z = h; \quad t > 0$$

Shen and Springer [3] point out that, due to the numerical values of the thermophysical properties C, K_z, D_z, and ρ for typical composites, the temperature approaches equilibrium about 1 million times faster than the moisture concentration. Thus, the material temperature can usually be assumed to be the same as the ambient temperature, but the moisture distribution requires further analysis. If the diffusivity is assumed to be constant, Fick's second law becomes

$$\frac{\partial c}{\partial t} = D_z \frac{\partial^2 c}{\partial^2 z} \tag{5.3}$$

The solution to this equation subject to the previously stated initial and boundary conditions is [3,4]

$$\frac{c - c_i}{c_m - c_i} = 1 - \frac{4}{\pi} \sum_{j=0}^{\infty} \frac{1}{(2j+1)} \sin \frac{(2j+1)\pi z}{h} \times \exp\left[-\frac{(2j+1)^2 \pi^2 D_z t}{h^2}\right] \tag{5.4}$$

where the moisture concentration at the surface of the material, c_m, is related to the moisture content of the environment, c_a. Browning et al. [1] used equation (5.4) to predict moisture profiles for a graphite/epoxy plate after drying out for various periods of time, as shown in figure 5.7. While equation (5.4) gives the *local* moisture concentration, $c(z, t)$, we normally measure the *total* amount of moisture averaged over the sample. The average concentration is given by [4]

$$\bar{c} = \frac{1}{h} \int_0^h c(z,t)dz = (c_m - c_i) \times \left[1 - \frac{8}{\pi^2} \sum_{j=0}^{\infty} \frac{\exp\left[-(2j+1)^2 \pi^2 \left(D_z t / h^2\right)\right]}{(2j+1)^2}\right] + c_i \tag{5.5}$$

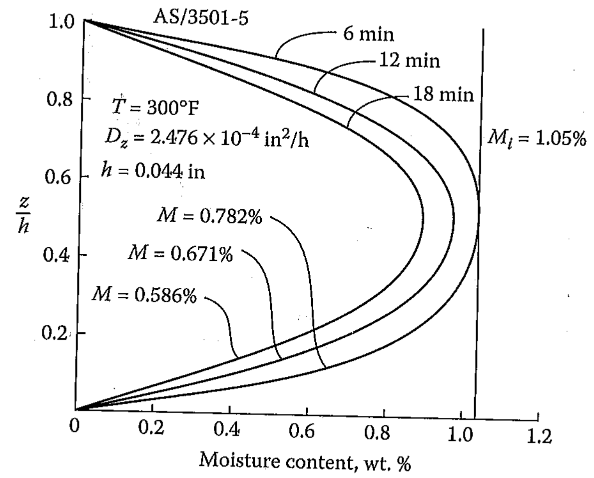

FIGURE 5.7
Predicted moisture profiles through the thickness of a graphite/epoxy plate after drying out for various periods of time. From Browning, C.E., Husman, G.E., and Whitney, J.M. 1977. *Composite Materials: Testing and Design: Fourth Conference*, ASTM STP 617, pp. 481–496. American Society for Testing and Materials, Philadelphia, PA. Copyright, ASTM. Reprinted with permission.)

The weight percent moisture, M, is the quantity that is normally measured, and since $\bar{c}$ is linearly related to M, we can write [3]

$$G = \frac{M - M_i}{M_m - M_i} = 1 - \frac{8}{\pi^2} \sum_{j=0}^{\infty} \frac{\exp\left[-(2j+1)^2 \pi^2 \left(D_z t / h^2\right)\right]}{(2j+1)^2} \tag{5.6}$$

where M_i is the initial weight percent of moisture in the material and M_m is the weight percent of moisture in the material when the material reaches fully saturated equilibrium with the ambient conditions. Thus, the parameter G describes the moisture weight gain as a function of time. Such data can be obtained experimentally by weighing the specimen at various times during exposure to a moist environment. Figure 5.8 from ref. [3] shows a comparison of measured and predicted values of G as a function of the dimensionless ratio $D_z t / h^2$ for graphite/epoxy. The agreement is seen to be excellent. Thus, the moisture diffusion process in these composites seems to follow Fick's law. Non-Fickian diffusion has also been observed in some cases where microcracking is developed as a result of the hygrothermal degradation [5]. The time-dependent viscoelastic response of polymers has also been found to lead to non-Fickian moisture

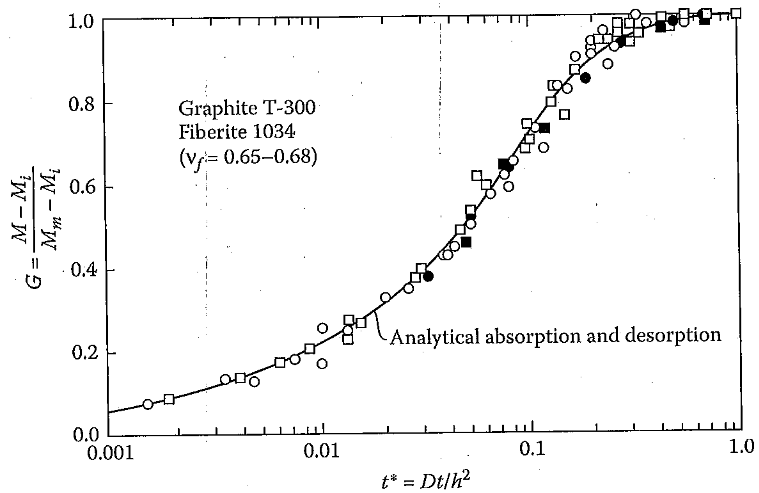

FIGURE 5.8
Comparison of predicted (eq. [5.6]) and measured moisture absorption and desorption of T300/1034 graphite/epoxy composites. Open symbols represent measured absorption and dark symbols represent measured desorption. (From Shen, C.H. and Springer, G.S. 1976. *Journal of Composite Materials*, 10, 2–20. Reprinted by permission of Technomic Publishing Co.)

diffusion in polymer composites [6]. For more information on these and various other moisture effects in polymer composites, the reader is referred to several review articles by Weitsman [7] and Weitsman and Elahi [8].

The hygrothermal degradation of composite strength and/or stiffness can be estimated by using an empirical equation to degrade the corresponding matrix property, then by using the degraded matrix property in the appropriate micromechanics equation. Chamis and Sinclair [9] and Chamis [10] have demonstrated such a procedure based on the equation

$$F_m = \frac{P}{P_o} = \left[\frac{T_{gw} - T}{T_{go} - T_o}\right]^{1/2} \tag{5.7}$$

where

F_m = matrix mechanical property retention ratio
P = matrix strength or stiffness after hygrothermal degradation
P_o = reference matrix strength or stiffness before degradation
T = temperature at which P is to be predicted (°F)
T_{go} = glass transition temperature for reference dry condition (°F)

T_{gw} = glass transition temperature for wet matrix material at moisture content corresponding to property P (°F) (fig. 5.1)
T_o = test temperature at which P_o was measured (°F)
(All temperatures are in °F.)

The form of equation (5.7) is based on the experimental observation that degradation is gradual until the temperature T approaches T_{gw}, whereupon the degradation accelerates. The value of T_{gw} can be obtained from experimental data on the glass transition temperature of the matrix resin as a function of absorbed moisture. For example, the data of DeIasi and Whiteside [11] show the reduction in T_{gw} with increasing moisture content for six epoxy resins (fig. 5.9). Chamis [10] suggests that T_{gw} can be estimated by using the following empirical equation:

$$T_{gw} = \left(0.005M_r^2 - 0.10M_r + 1.0\right)T_{go} \tag{5.8}$$

where M_r is the weight percent of moisture in the matrix resin and values of T_{go} for several matrix materials are found in table 3.2 and table 5.1. DeIasi and Whiteside [11] and Browning et al. [1] also found that data

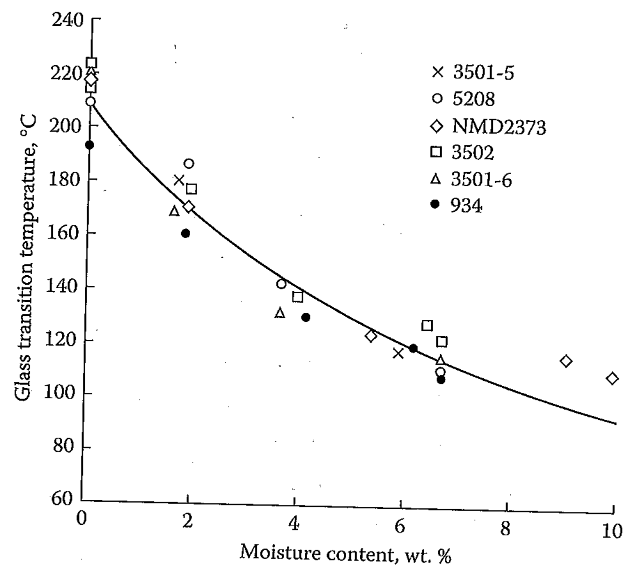

FIGURE 5.9
Variation of glass transition temperature with equilibrium moisture content for several epoxy resins. (From DeIasi, R. and Whiteside, J.B. 1987. In Vinson, J.R. ed., *Advanced Composite Materials — Environmental Effects*, ASTM STP 658, pp. 2–20. American Society for Testing and Materials, Philadelphia, PA. Copyright, ASTM. Reprinted with permission.)

such as that in figure 5.9 are in good agreement with predictions from the theory of polymer plasticization by diluents.

Once the mechanical property retention ratio is found from equation (5.7), it is used to degrade the matrix property in the appropriate micromechanics equation. For example, the rule of mixtures for the longitudinal modulus (eq. [3.23]) now becomes

$$E_1 = E_{f1}\upsilon_f + F_m E_{mo}\upsilon_m \tag{5.9}$$

where E_{mo} is the reference value of the matrix modulus in the dry condition. It is assumed that Poisson's ratio is not hygrothermally degraded [10].

Reasonably accurate predictions are also obtained when equation (5.7) is applied directly to matrix-dominated composite properties (i.e., P and P_o are taken to be matrix-dominated composite properties instead of matrix properties). For example, Chamis and Sinclair [9] found good agreement between the predictions of equation (5.7) and experimental data on hygrothermal degradation of transverse compression, transverse tension, and intralaminar shear strengths of boron/epoxy and graphite/epoxy composites (fig. 5.10). Thus, the hygrothermally degraded composite

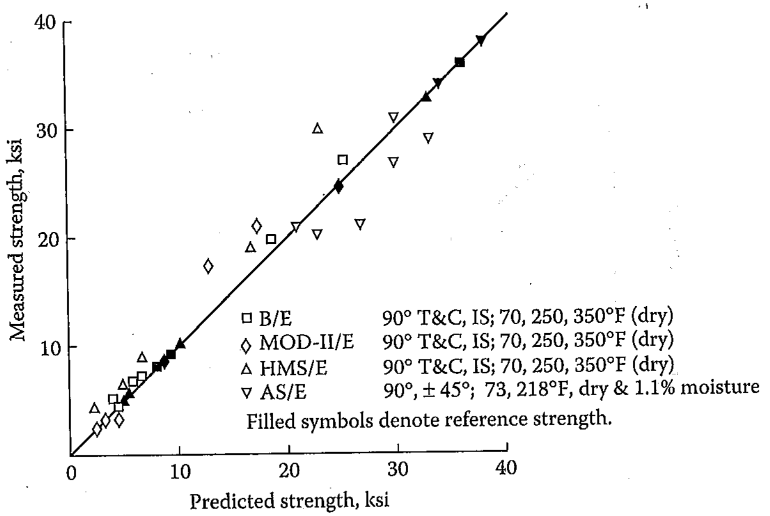

FIGURE 5.10
Comparison of predicted (eq. [5.7]) and measured strengths of several hygrothermally degraded composites. (From Chamis, C.C. and Sinclair, J.H. 1982. In Daniel, I.M. ed., *Composite Materials: Testing and Design (Sixth Conference)*, ASTM STP 787, pp. 498–512. American Society for Testing and Materials, Philadelphia, PA. Copyright, ASTM. Reprinted with permission.)

property may be estimated by applying equation (5.7) directly to the matrix-dominated composite property measured under reference conditions, or by applying equation (5.7) to matrix data measured under reference conditions, then substituting the result into the appropriate micromechanics equation.

Empirical equations such as equations (5.7) and equation (5.8) should always be used with caution. Curve-fitting parameters such as the exponent of 1/2 in equation (5.7) and the coefficients of M_r in equation (5.8) are based on experimental data for epoxy matrix materials. While the equations may be suitable for other composites as well, the user should check predictions against available experimental data where possible.

The procedure just outlined is based on the combined effects of temperature and moisture, and the two effects were seen to be coupled by the lowering of the glass transition temperature by absorbed moisture. There is another important connection between the two effects. Moisture absorption occurs by diffusion, which is known to be a thermally activated process. The diffusivity D that appears in Fick's law is related to temperature by the Arrhenius relationship:

$$D = D_o \exp(-E_a/RT) \tag{5.10}$$

where
D_o = material constant
E_a = activation energy for diffusion
R = universal gas constant
T = absolute temperature

Proof that this relationship holds for composites is given by the fact that plots of experimentally determined values of log D versus $1/T$ fall on a straight line, as shown in figure 5.11 from Loos and Springer [12]. The result of this relationship is that increased temperature causes an increase in the rate of moisture absorption, as shown in figure 5.12.

The applied stress also has an effect on moisture absorption in polymers and polymer composites [13–15]. For example, Fahmy and Hurt [13] have shown that the diffusivity of a polymer is increased under tensile stress and decreased under compressive stress. Thus, in a composite, the residual stresses due to differential thermal expansion of fiber and matrix materials may cause increased moisture absorption along a path running through a tensile stress field. Starting from the basic principles of continuum mechanics and irreversible thermodynamics, Weitsman [15] showed that, for both elastic and viscoelastic materials, both the diffusion process and the saturation moisture levels

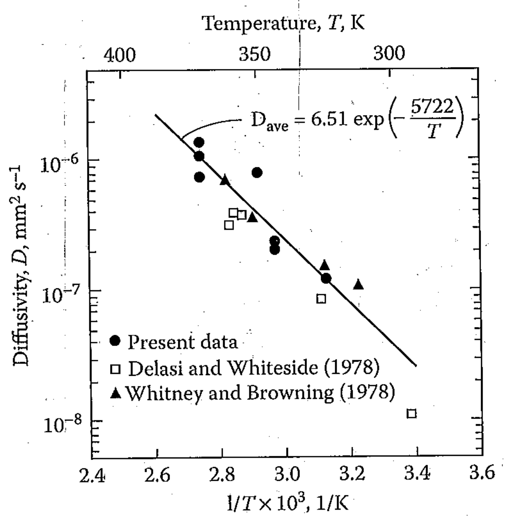

FIGURE 5.11
Variation of transverse diffusivity with temperature for AS/3501-5 graphite/epoxy composite. (From Loos, A.C. and Springer, G.S. 1981. In Springer, G.S. ed., *Environmental Effects on Composite Materials*, pp. 34–50. Technomic Publishing Co., Lancaster, PA. Reprinted by permission of Technomic Publishing Co.)

are stress dependent, and that the diffusion process is nonlinear with respect to stress.

EXAMPLE 5.1
An epoxy resin sample has a thickness $h = 5$ mm and a diffusivity $D = 3 \times 10^{-8}$ mm^2/s. Determine the moisture absorption of an initially dry sample after a time $t = 100$ days.

Solution. The moisture absorption is predicted by equation (5.6), which involves an infinite series. In order to examine the convergence characteristics of the series, we will look at the first four terms. Each term in the series contains the dimensionless ratio $\pi^2 Dt/h^2$, which has the numerical value

$$\frac{\pi^2 Dt}{h^2} = \frac{\pi^2(3\times10^{-8})(100)(60)(60)(24)}{(5)^2} = 0.012$$

Since the sample was initially dry, the initial weight of moisture in the material is $M_i = 0$. Thus, equation (5.6) reduces to the ratio M/M_m, which is the ratio of the weight percent of moisture at time t to the weight percent

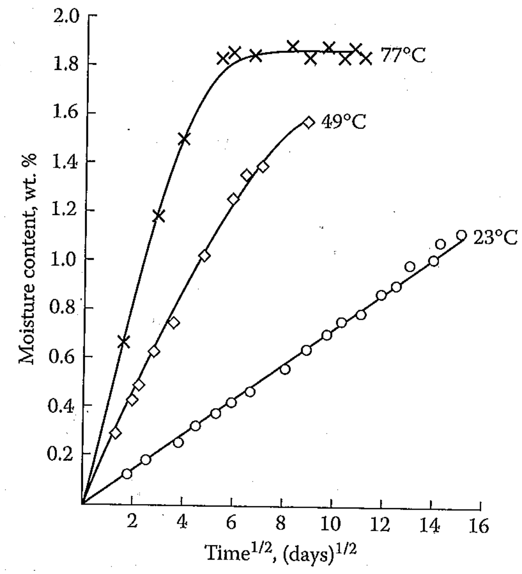

FIGURE 5.12
Effect of temperature on rate of moisture absorption in AS/3501–5 graphite/epoxy composite. (From DeIasi, R. and Whiteside, J.B. 1987. In Vinson, J.R. ed., *Advanced Composite Materials — Environmental Effects*, ASTM STP 658, pp. 2–20. American Society for Testing and Materials, Philadelphia, PA. Copyright, ASTM. Reprinted with permission.)

of moisture in the fully saturated equilibrium condition. The first four terms are

$$\frac{M}{M_m} = 1 - \frac{8}{\pi^2}\left[\exp(-0.102) + \frac{\exp(-9(0.102))}{9} + \frac{\exp(-25(0.102))}{25} + \frac{\exp(-49(0.102))}{49} + \cdots\right]$$

The values of M/M_m corresponding to the different number of terms are: 0.267 (one term), 0.230 (two terms), 0.228 (three terms), and 0.228 (four terms). Thus, the series has converged after three terms. Rapid convergence is a characteristic of this solution, and in many cases, only one term is sufficient [4].

EXAMPLE 5.2
The composite described in example 3.1, example 3.2, and example 3.4 is to be used in a "hot–wet" environment with temperature $T = 200°F$ (93°C) and resin moisture content $M_r = 3\%$. If the glass transition temperature of the dry matrix

resin is 350°F (177°C) and if the properties given in Example 3.1, example 3.2, and example 3.4 are for a temperature of 70°F (21°C), determine the hygrothermally degraded values of the longitudinal and transverse moduli.

Solution. From equation (5.8), the glass transition temperature in the wet condition is:

$$T_{gw} = [0.005(3)^2 - 0.1(3) + 1.0]350 = 261°F\ (127°C)$$

From equation (5.7), the hygrothermally degraded Young's modulus of the epoxy resin is

$$E_m = [(261-200)/(350-70)]^{1/2}(0.5)(10^6) = 0.233(10^6)\text{psi}\ (1.61\ \text{GPa})$$

From equation (5.9), the hygrothermally degraded longitudinal modulus is

$$E_1 = 32(10^6)(0.506) + 0.233(10^6)(0.482) = 16.3(10^6)\text{psi}\ (112\ \text{GPa})$$

Thus, the hygrothermally degraded value of E_1 is 99.2% of the reference value calculated in example 3.4. As stated earlier, the fiber-dominated properties are not affected much by temperature and moisture.

Similarly, using the degraded value of E_m in equation (3.36), we find that the hygrothermally degraded transverse modulus is estimated to be E_2 = $0.434(10^6)$ psi (3.0 GPa), which is only 53% of the reference value calculated in example 3.4. Thus, the matrix-dominated properties such as the transverse modulus are strongly affected by hygrothermal conditions.

5.3 Lamina Stress–Strain Relationships Including Hygrothermal Effects

In chapter 2, the lamina stress–strain relationships were developed for linear elastic behavior and constant environmental conditions. The thermal expansion or contraction of structural materials due to temperature change is a well-known phenomenon, however, and the thermal strains for an isotropic material are usually described by an equation of the form

$$\epsilon_i^T = \begin{cases} \alpha\Delta T, & \text{if } i = 1,2,3 \\ 0, & \text{if } i = 4,5,6 \end{cases} \tag{5.11}$$

where
$i = 1, 2, \ldots, 6$ (recall contracted notation)
ΔT = temperature change $(T - T_o)$
T = final temperature
T_o = initial temperature where $\epsilon_i^T = 0$ for all i
α = coefficient of thermal expansion (CTE)

This relationship is based on the experimental observation that a temperature change in an unrestrained isotropic material induces an equal expansion or contraction in all directions, with no distortion due to shear deformation. In this case $\alpha > 0$, because an increase in temperature causes an increase in strain. As we will see later, however, some anisotropic fiber materials have *negative* CTEs along the fiber axis and positive CTEs along the transverse direction. In general, the strain–temperature relationship is nonlinear, but the assumption of linearity is valid over a sufficiently narrow temperature range. Typical thermal expansion data for an epoxy resin are shown in figure 5.13. If operation over a wide temperature range is expected, the reader is referred to data such as that of Cairns and Adams [16], who have developed cubic polynomial expressions to fit experimental thermal expansion data for epoxy, glass/epoxy, and graphite/epoxy from –73 to 175°C. A procedure for estimating the hygrothermal degradation of matrix-dominated thermal properties will be discussed in section 5.4.

In polymeric materials, moisture has been shown to cause hygroscopic expansions or contractions analogous to thermal strains. For example, the

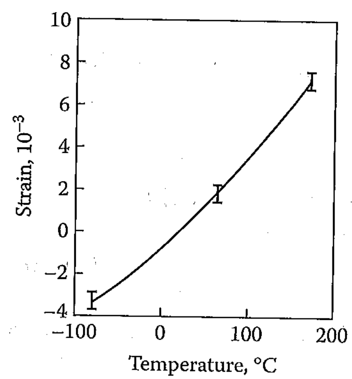

FIGURE 5.13
Thermal expansion vs. temperature for 3501-6 epoxy resin. (From Cairns, D.S. and Adams, D.F. 1984. In Springer, G.S. ed., *Environmental Effects on Composite Materials*, vol. 2, pp. 300–316. Technomic Publishing Co., Lancaster, PA. Reprinted by permission of Technomic Publishing Co.)

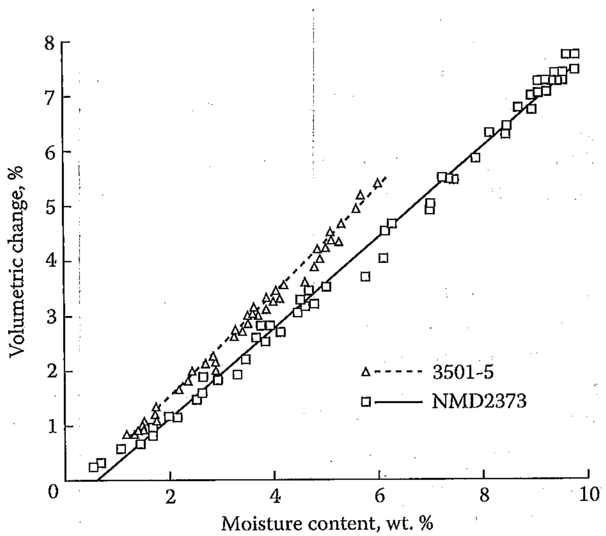

FIGURE 5.14
Hygroscopic expansion vs. moisture content for two epoxy resins. (From Delasi, R. and Whiteside, J.B. 1987. In Vinson, J.R. ed., *Advanced Composite Materials — Environmental Effects*, ASTM STP 658, pp. 2–20. American Society for Testing and Materials, Philadelphia, PA. Copyright, ASTM. Reprinted with permission.)

experimentally determined moisture-induced swelling of several epoxy resins is shown in figure 5.14. The experimental observation is that the moisture-induced strains in isotropic materials can be expressed as

$$\epsilon_i^M = \begin{cases} (\beta)c, & \text{if } i = 1,2,3 \\ 0, & \text{if } i = 4,5,6 \end{cases} \tag{5.12}$$

where

c = moisture concentration = (mass of moisture in unit volume/mass of dry material in unit volume)

β = coefficient of hygroscopic expansion (CHE)

The reference condition is assumed to be the moisture-free state $c = 0$, where $\epsilon_i^M = 0$. Hygroscopic strains are generally nonlinear functions of moisture content [16], but the linear relationship in equation (5.12) is valid if the range of moisture contents is not too wide. Thus, in an isotropic material, the total hygrothermal strain can be written as

$$\epsilon_i^H = \epsilon_i^T + \epsilon_i^M \tag{5.13}$$

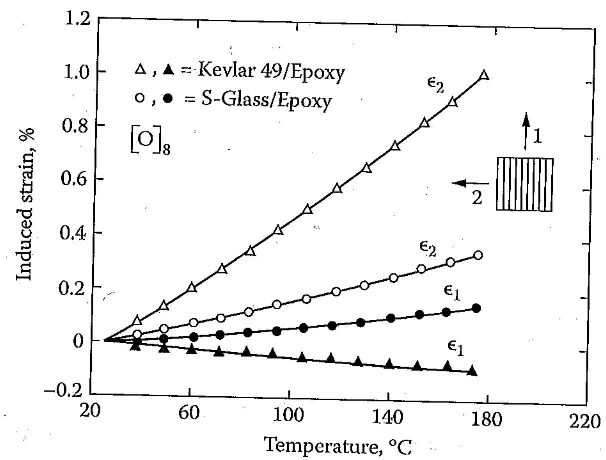

FIGURE 5.15
Variation of measured longitudinal and transverse thermal strains for unidirectional Kevlar 49/epoxy and S-glass/epoxy with temperature. (From Adams, D.F., Carlsson, L.A., and Pipes, R.B., 2003. *Experimental Characterization of Advanced Composite Materials*. CRC Press, Boca Raton, FL. With permission.)

Because fibers usually have CTEs and CHEs that are quite different from those of matrix materials, the hygrothermal strains in a composite lamina are different in longitudinal and transverse directions. For example, the experimental thermal strain versus temperature data in figure 5.15 (from ref. [18]) shows the large differences between longitudinal (ε_1) and transverse (ε_2) thermal strains for unidirectional Kevlar 49/epoxy and S-glass/epoxy composites. Notice that the longitudinal thermal strains ε_1 for Kevlar 49/epoxy are negative, while the corresponding transverse thermal strains ε_2 are positive, which implies that the longitudinal CTE, α_1, is negative and the transverse CTE, α_2, is positive for this material. Carbon fiber–reinforced composites often have similar characteristics. Notice also in table 3.1 that the longitudinal CTEs of some other fibers are negative, whereas the transverse CTEs are positive. As shown later, this leads to the interesting possibility of designing a composite with a CTE of near zero. Thus, subscripts are needed for α and β, and the hygrothermal strains associated with the 12 principal material axes in the specially orthotropic lamina should be expressed as

$$\epsilon_i^H = \begin{cases} \alpha_i \Delta T + \beta_i c, & \text{if } i = 1,2,3 \\ 0, & \text{if } i = 4,5,6 \end{cases} \tag{5.14}$$

TABLE 5.3
Typical Thermal and Hygroscopic Expansion Properties

Material	Thermal Expansion Coefficients ([10^{-6} m/m]/°C)		Hygroscopic Expansion Coefficients (m/m)	
	α_1	α_2	β_1	β_2
AS carbon/epoxy	0.88	31.0	0.09	0.30
E-glass/epoxy	6.3	20.0	0.014	0.29
AF-126-2 adhesive	29.0	29.0	0.20	0.20
1020 steel	12.0	12.0	—	—

Source: From Graves, S.R. and Adams, D.F. 1981. *Journal of Composite Materials*, 15, 211–224. With permission.

If the material is transversely isotropic, $\alpha_2 = \alpha_3$ and $\beta_2 = \beta_3$. Typical values of α_i, and β_i for several composites are given in table 5.3 from ref. [17]. Notice that the negative longitudinal CTE of graphite fibers leads to a very small longitudinal CTE for the lamina. Notice also the large differences between longitudinal and transverse hygrothermal coefficients.

The total strains along the principal material axes in the specially orthotropic lamina are found by summing the mechanical strains due to applied stresses (eq. [2.24]) and the hygrothermal strains (eq. [5.14]):

$$\begin{Bmatrix} \epsilon_1 \\ \epsilon_2 \\ \gamma_{12} \end{Bmatrix} = \begin{bmatrix} S_{11} & S_{12} & 0 \\ S_{21} & S_{22} & 0 \\ 0 & 0 & S_{66} \end{bmatrix} \begin{Bmatrix} \sigma_1 \\ \sigma_2 \\ \tau_{12} \end{Bmatrix} + \begin{Bmatrix} \alpha_1 \\ \alpha_2 \\ 0 \end{Bmatrix} \Delta T + \begin{Bmatrix} \beta_1 \\ \beta_2 \\ 0 \end{Bmatrix} c \tag{5.15}$$

or, in more concise matrix notation,

$$\{\epsilon\} = [S]\{\sigma\} + \{\alpha\}\Delta T + \{\beta\}c \tag{5.16}$$

whereupon the stresses are given by

$$\{\sigma\} = [S]^{-1}(\{\epsilon\} - \{\alpha\}\Delta T - \{\beta\}c) \tag{5.17}$$

Note that if the material is unrestrained during the hygrothermal exposure, there are no stresses generated and the strains are given by

$$\{\epsilon\} = \{\alpha\}\Delta T + \{\beta\}c \tag{5.18}$$

If the material is completely restrained during hygrothermal exposure, however, the total strain must be zero. Thus,

$$\{\epsilon\} = 0 = [S]\{\sigma\} + \{\alpha\}\Delta T + \{\beta\}c \tag{5.19}$$

and the resulting hygrothermal stresses are given by

$$\{\sigma\} = [S]^{-1}(-\{\alpha\}\Delta T - \{\beta\}c) \tag{5.20}$$

Note that there are no hygrothermal shear strains or shear stresses along the principal material axes. This is not true for the generally orthotropic (off-axis) case, however. For an arbitrary set of axes xy oriented at an angle θ to the 12 axes, the stress–strain relationships can be transformed as in chapter 2. The complete stress–strain relations for the generally orthotropic lamina are

$$\begin{Bmatrix} \epsilon_x \\ \epsilon_y \\ \gamma_{xy} \end{Bmatrix} = \begin{bmatrix} \bar{S}_{11} & \bar{S}_{12} & \bar{S}_{16} \\ \bar{S}_{12} & \bar{S}_{22} & \bar{S}_{26} \\ \bar{S}_{16} & \bar{S}_{26} & \bar{S}_{66} \end{bmatrix} \begin{Bmatrix} \sigma_x \\ \sigma_y \\ \tau_{xy} \end{Bmatrix} + \begin{Bmatrix} \alpha_x \\ \alpha_y \\ \alpha_{xy} \end{Bmatrix} \Delta T + \begin{Bmatrix} \beta_x \\ \beta_y \\ \beta_{xy} \end{Bmatrix} c \tag{5.21}$$

In the transformations, it must be remembered that the CTEs and the CHEs transform like *tensor strains* (recall eqs. [2.33]), so that

$$\begin{Bmatrix} \alpha_x \\ \alpha_y \\ \alpha_{xy}/2 \end{Bmatrix} = [T]^{-1} \begin{Bmatrix} \alpha_1 \\ \alpha_2 \\ 0 \end{Bmatrix} \tag{5.22}$$

and a similar equation is used for the CHEs. Notice that the hygrothermal effects *do* induce shear strains in the off-axis case due to α_{xy} and β_{xy}, the shear coefficients of thermal and hygroscopic expansion, respectively. This is quite different from the case of isotropic materials, where hygrothermal effects do not cause shear strains along any axes. The variations of α_x, α_y, and α_{xy} with lamina orientation according to equations (5.22) are shown in figure 5.16. The same curves could also be used for β_x, β_y, and β_{xy}. The hygrothermal shear coefficients α_{xy} and β_{xy} have their maximum values at $\theta = 45°$ and are proportional to the differences $(\alpha_1 - \alpha_2)$ and $(\beta_1 - \beta_2)$, respectively. Thus, the greater the degree of anisotropy (i.e., the larger the ratio α_1/α_2 or β_1/β_2), the greater the hygrothermally induced shear strains. It is important to note that if $\alpha_1 < 0$ and $\alpha_2 > 0$, it is possible to find an angle θ where $\alpha_x = 0$. Thus, we can design a laminate consisting of plies of such a material, so that the CTE along a particular direction is zero.

EXAMPLE 5.3

An orthotropic lamina forms one layer of a laminate which is initially at temperature T_o. Assuming that the lamina is initially stress free, that adjacent lamina are rigid, that the properties do not change as a result of the temperature

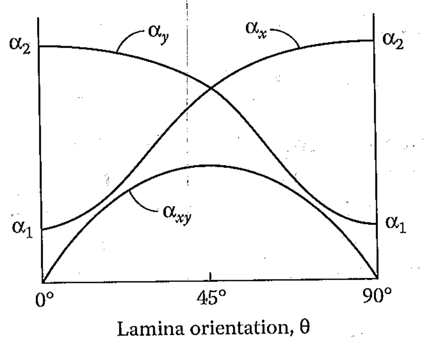

FIGURE 5.16
Variation of lamina thermal expansion coefficients with lamina orientation for a lamina having $\alpha_2 > \alpha_1 > 0$.

change, and that the lamina picks up no moisture, determine the maximum temperature that the lamina can withstand according to the Maximum Stress Criterion.

Solution. Due to the assumption that adjacent laminae are rigid, deformation is prevented and the total strains must all be zero. The resulting hygrothermal stresses are therefore given by equation (5.20) with $c = 0$,

$$\{\sigma\} = -[S]^{-1}\{\alpha\}(T - T_o) = -[Q]\{\alpha\}(T - T_o)$$

Thus, for the Maximum Stress Criterion, it is necessary to check each of the following conditions:

For tensile stresses

$$-(Q_{11}a_1 + Q_{12}a_2)(T - T_o) = s_L^{(+)}$$

$$-(Q_{12}a_1 + Q_{22}a_2)(T - T_o) = s_T^{(+)}$$

For compressive stresses

$$-(Q_{11}a_1 + Q_{12}a_2)(T - T_o) = s_L^{(-)}$$

$$-(Q_{12}a_1 + Q_{22}a_2)(T - T_o) = s_T^{(-)}$$

(*Note:* There are no hygrothermal shear stresses along the 12 axes.)

After substituting numerical values for the initial temperature, T_o, the lamina stiffness, Q_{ij}, the coefficients of thermal expansion, α_i, the strengths $s_L^{(+)}$, etc., in the above equations, the equation that yields the lowest temperature T would be the condition governing failure. It is worthwhile to note that adjacent laminae are not really rigid, but we will need to use laminate theory later to consider deformations of adjacent laminae. It is also worthwhile to note that if hygrothermal degradation of properties is to be taken into account, equation (5.7) could be used to express the hygrothermally degraded lamina strengths and stiffnesses in terms of the temperature T. In this case T would appear on both sides of the above equations and the problem would be more difficult to solve.

EXAMPLE 5.4

A sample of a unidirectional E-glass/epoxy lamina is completely unrestrained as it is heated from 20° to 70°C. Determine all components of stress and strain associated with the 1,2 axes and the x,y axes if the x,y axes are oriented at θ = 45°. See table 5.3 for the required properties of E-glass/epoxy.

Solution. Since the lamina is unrestrained during heating, there are no stresses along either the 1,2 or the x,y axes, but the thermal strains are found as follows:

From equation (5.15) with no stresses or hygroscopic strains, the thermal strains along the 1,2 axes for $\Delta T = 50°C$ are

$$\begin{Bmatrix} \varepsilon_1 \\ \varepsilon_2 \\ \gamma_{12} \end{Bmatrix} = \begin{Bmatrix} \alpha_1 \\ \alpha_2 \\ 0 \end{Bmatrix} \Delta T = \begin{Bmatrix} 6.3(10^{-6}) \\ 20.0(10^{-6}) \\ 0 \end{Bmatrix} (50) = \begin{Bmatrix} 0.000315 \\ 0.001 \\ 0 \end{Bmatrix}$$

From the inverted form of equation (2.33), with θ = 45°, the thermal strains along the x,y axes can be found directly as

$$\begin{Bmatrix} \varepsilon_x \\ \varepsilon_y \\ \dfrac{\gamma_{xy}}{2} \end{Bmatrix} = [T]^{-1} \begin{Bmatrix} \varepsilon_1 \\ \varepsilon_2 \\ \gamma_{12}/2 \end{Bmatrix} = \begin{bmatrix} 0.5 & 0.5 & -0.5 \\ 0.5 & 0.5 & 0.5 \\ 0.5 & -0.5 & 0 \end{bmatrix} \begin{Bmatrix} 0.000315 \\ 0.001 \\ 0 \end{Bmatrix} = \begin{Bmatrix} 0.00066 \\ 0.00066 \\ -0.00034 \end{Bmatrix}$$

Alternatively, the same result for the thermal strains along the x,y axes can be obtained by first transforming the CTE values from the 1,2 axes to the

x,y axes using equation (5.22), then substituting the transformed CTEs in equation (5.21) to calculate the thermal strains along the x,y axes. Note that, although there was no thermal shear strain along the 1,2 axes, there is an off-axis thermal shear strain along the x,y axes. Thus, there will be thermal distortion associated with the off-axis directions, and this is another example of the shear coupling phenomenon.

5.4 Micromechanics Models for Hygrothermal Properties

We have seen in chapter 3 and chapter 4 that the mechanical properties of a composite lamina can be estimated from the corresponding properties of the constituent materials using micromechanics models. Similarly, micromechanics equations for the thermophysical properties that appear in hygrothermal analysis can be developed. Various theoretical approaches ranging from elementary mechanics of materials to energy methods have been proposed.

An equation for the longitudinal coefficient of thermal expansion, α_1, can be developed using the elementary mechanics of materials approach from chapter 3. Recall that in the derivation of the rule of mixtures for the longitudinal modulus (eq. [3.23]), the 1-D forms of the stress–strain relationships along the 1 direction for the lamina, fiber, and matrix materials (eq. [3.20]) were substituted in the rule of mixtures for longitudinal stress, equation (3.19). The corresponding 1-D form of the stress–strain relationship including the thermal effect is

$$\epsilon_1 = \frac{\sigma_1}{E_1} + \alpha_1 \Delta T \tag{5.23}$$

or

$$\alpha_1 = E_1(\epsilon_1 - \alpha_1 \Delta T) \tag{5.24}$$

If we now substitute equations similar to equation (5.24) for composite, fiber, and matrix, respectively, into equation (3.19), the result is

$$E_1(\bar{\epsilon}_1 - \alpha_1 \Delta T) = E_{f1}(\bar{\epsilon}_{f1} - \alpha_{f1}\Delta T)\upsilon_f + E_{m1}(\bar{\epsilon}_{m1} - \alpha_{m1}\Delta T)\upsilon_m \tag{5.25}$$

where α_{f1} and α_{m1} are the longitudinal CTEs of fiber and matrix materials, respectively (see table 3.1 and table 3.2), and the remaining terms are defined in chapter 3. By combining equation (5.25), equation (3.22), and

equation (3.23), we get a modified rule of mixtures for the longitudinal CTE:

$$\alpha_1 = \frac{E_{f1}\alpha_{f1}\upsilon_f + E_{m1}\alpha_{m1}\upsilon_m}{E_1} = \frac{E_{f1}\alpha_{f1}\upsilon_f + E_{m1}\alpha_{m1}\upsilon_m}{E_{f1}\upsilon_f + E_{m1}\upsilon_m} \tag{5.26}$$

For the case of isotropic constituents, the above equation becomes

$$\alpha_1 = \frac{E_f\alpha_f\upsilon_f + E_m\alpha_m\upsilon_m}{E_f\upsilon_f + E_m\upsilon_m} \tag{5.27}$$

This equation, derived by a mechanics of materials approach, turns out to be the same as the result obtained by Schapery [19], who used a more rigorous energy method. Hashin [20] derived a more complicated expression for the case of orthotropic constituents. Schapery [19] derived the following expression for the transverse CTE of a composite with isotropic constituents:

$$\alpha_2 = (1 + \nu_m)\alpha_m\upsilon_m + (1 + \nu_f)\alpha_f\upsilon_f - \alpha_1\nu_{12} \tag{5.28}$$

where α_1 is the longitudinal CTE given by equation (5.27) and ν_{12} is the major Poisson's ratio given by equation (3.41). The variations of α_1 and α_2 with fiber-volume fraction for a typical graphite/epoxy composite are shown in figure 5.17. Rosen [21] has observed that for such composites having high fiber-volume fractions, the predicted α_1 is practically zero. Measurements of the CTEs for such materials by Ishikawa et al. [22] have confirmed that α_1 is so small as to fluctuate between positive and negative values due to small changes in temperature or fiber-volume fraction. Over the range of practical fiber-volume fractions, α_2 is much greater than α_1. It is also interesting to note that at low fiber-volume fractions, α_2 can be greater than α_m.

By substituting the 1-D forms of the stress–strain relationships with hygroscopic effects into equation (3.19) and following the procedure outlined in the derivation of equation (5.26), a similar relationship is found for the longitudinal CHE:

$$\beta_1 = \frac{E_{f1}\beta_{f1}\upsilon_f + E_{m1}\beta_{m1}\upsilon_m}{E_{f1}\upsilon_f + E_{m1}\upsilon_m} \tag{5.29}$$

In polymer matrix composites, the amount of moisture absorbed by the fibers is usually negligible in comparison with the moisture absorbed

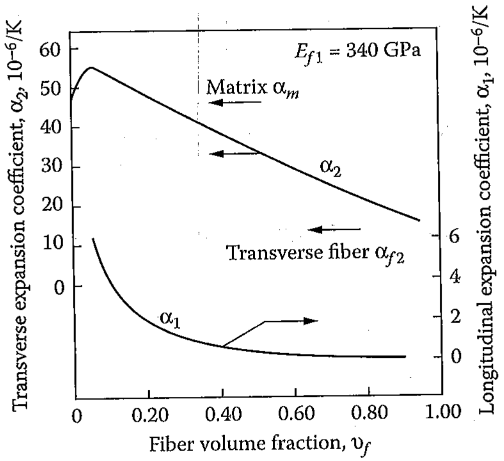

FIGURE 5.17
Variation of predicted longitudinal and transverse coefficients of thermal expansion with fiber-volume fraction for typical unidirectional graphite/epoxy composite. (From Rosen, B.W. 1987. In Reinhart, T.J. ed., *Engineered Materials Handbook*, vol. 1, *Composites*, Sec. 4. ASM International, Materials Park, OH. Reprinted by permission of ASM International.)

by the matrix, so that the term involving β_{f1} can be ignored. For isotropic constituents, the equation for β_1 would be analogous to equation (5.27). According to Ashton et al. [23], the equations derived by Schapery (i.e., eq. [5.27] and eq. [5.28]) can be used for any expansional coefficients such as the CTE or the CHE. Thus, the transverse CHE would be given by

$$\beta_2 = (1+\nu_m)\beta_m \upsilon_m + (1+\nu_f)\beta_f \upsilon_f - \beta_1 \nu_{12} \tag{5.30}$$

where β_1 is given by the isotropic form of equation (5.29).

Recall that in the equations governing the temperature and moisture distributions (eq. [5.1] and eq. [5.2]), thermophysical properties such as specific heat, thermal conductivity, and diffusivity appeared. According to Chamis [10], the composite specific heat is given by

$$C_c = \frac{1}{\rho_c}(\rho_f C_f \upsilon_f + \rho_m C_m \upsilon_m) \tag{5.31}$$

where C_f and C_m are the specific heats of fiber and matrix, respectively; the composite density, ρ_c, is given by equation (3.6), and the remaining

terms are defined in chapter 3. Ashton et al. [23] and Shen and Springer [3] have observed that the rule of mixtures formulations,

$$K_1 = K_f \upsilon_f + K_m \upsilon_m \tag{5.32}$$

and

$$D_1 = D_f \upsilon_f + D_m \upsilon_m \tag{5.33}$$

can be used to find the longitudinal thermal conductivity and mass diffusivity, respectively, as well as other transport properties. Equations for the transverse thermal conductivity and diffusivity based on the method of subregions (see section 3.3) have been presented by Hopkins and Chamis [24] and Chamis [10]. These equations can be formed by substituting the appropriate properties (thermal conductivities or diffusivities instead of transverse moduli) in an equation of the form shown in equation (3.50). Ashton et al. [23] have suggested that the Halpin–Tsai equations (see section 3.5) can also be used for transverse transport properties such as thermal conductivity and mass diffusivity. Off-axis properties can be found by recognizing that thermal conductivity and diffusivity are both second-order tensor quantities that transform according to the form shown in equations (2.30).

Finally, a procedure for estimating hygrothermal degradation of matrix properties such as α, β, K, and C has been proposed by Chamis [10]. Based on the observation that the effect of increased temperature on these properties is opposite to the corresponding effect on strength and stiffness, Chamis suggests that the matrix hygrothermal property retention ratio can be approximated by

$$F_h = \frac{R}{R_o} = \left[\frac{T_{go} - T_o}{T_{gw} - T}\right]^{1/2} \tag{5.34}$$

where
R = matrix hygrothermal property after hygrothermal degradation
R_o = reference matrix hygrothermal property before degradation

Following a procedure similar to that outlined in section 5.2, the matrix hygrothermal property is degraded according to equation (5.34). Then the degraded matrix property is used in a micromechanics equation such as equation (5.26) through equation (5.33) to estimate the hygrothermally degraded composite property.

EXAMPLE 5.5

A composite lamina is to be designed to have a specified coefficient of thermal expansion along a given direction. Outline a procedure to be used in the design.

Solution. First, it is necessary to use micromechanics equations such as equation (5.27) and equation (5.28) to find a combination of fiber and matrix materials having constituent CTEs and moduli and volume fractions, so that the specified CTE lies between the values of α_1 and α_2. As shown by equations (5.22) and figure 5.16, the value of the specified α_x along the direction defined by the angle must lie between the values of α_1 and α_2. The required angle θ is then found by setting α_x equal to the specified value and solving the first of equations (5.22). In a practical design problem, other constraints would have to be considered as well.

EXAMPLE 5.6

Develop an analytical model for determination of the coefficient of hygroscopic expansion, β, for a randomly oriented continuous fiber composite in terms of fiber and matrix properties and volume fractions. Assume that the composite is planar isotropic, and find the β for in-plane hygroscopic expansion.

Solution. For the planar isotropic case, β is independent of orientation in the plane, and it is appropriate to use an averaging approach similar to that used in example 2.5. Thus, the isotropic β is found by first using a transformation equation similar to equation (5.22) to find the β_x for the orthotropic lamina of the same material along the x direction as

$$\beta_x = \beta_1 \cos^2\theta + \beta_2 \sin^2\theta$$

This value is now averaged over all possible angles between $\theta = 0$ to $\theta = \pi$ to get the isotropic property as

$$\beta = \frac{\int_0^\pi \beta_x d\theta}{\int_0^\pi d\theta} = \frac{\int_0^\pi \left(\beta_1 \cos^2\theta + \beta_2 \sin^2\theta\right) d\theta}{\pi}$$

$$= \frac{\beta_1}{\pi}\left[\frac{\sin 2\theta}{4} + \frac{\theta}{2}\right]_0^\pi + \frac{\beta_2}{\pi}\left[\frac{-\sin 2\theta}{4} + \frac{\theta}{2}\right]_0^\pi = \frac{\beta_1 + \beta_2}{2}$$

where the orthotropic properties β_1 and β_2 may be estimated from fiber and matrix properties and volume fractions by using micromechanics equations such as equation (5.29) and equation (5.30).

5.5 Problems

1. Using equation (5.6) for moisture diffusion, derive an equation for the time required for an initially dry material to reach 99.9% of its fully saturated equilibrium moisture content. The series in equation (5.6) converges rapidly, so for the purposes of this problem, it is necessary only to consider the first term. The answer should be expressed in terms of the thickness, h, and the diffusivity, D_z.
2. The dependence of the transverse (through-the-thickness) diffusivity of unidirectional AS/3501-5 graphite/epoxy composite on temperature is given in figure 5.11. For a temperature of 77°C and a thickness of 2.54 mm, use the results from figure 5.11 and problem 5.1 to estimate the time required for this material to reach 99.9% of its fully saturated equilibrium moisture content from an initially dry condition. Compare your estimate with the experimental data in figure 5.12. Does the estimate seem to be reasonable?
3. For the material described in problems 1 and 2 above at a temperature of 77°C, determine the time required for drying the material from 99.9% to 50% of its fully saturated equilibrium moisture content.
4. Using only the linear part of the moisture absorption curve for a temperature of 77°C in figure 5.12, and assuming a thickness of 2.54 mm, estimate the diffusivity D_z. Compare this value with the estimate from figure 5.11.
5. For the composite properties and environmental conditions described in examples 3.3, 4.5, and 5.2, determine the hygrothermally degraded values of the longitudinal and transverse tensile strengths. Compare with the reference values of these strengths from example 4.5.
6. For the composite properties and environmental conditions described in examples 3.4, 4.5, and 5.2, compare the reference and hygrothermally degraded values of the longitudinal compressive strength. Assume $v_{12} = 0.3$. Compare and discuss the different effects that hygrothermal conditions have on longitudinal tensile and compressive strengths.
7. The filament wound E-glass/epoxy pressure vessel described in example 4.3 is to be used in a hot–wet environment with temperature $T = 100°F$ (38°C) and moisture content $M_m = 4\%$. The glass transition temperature of the dry epoxy resin is 250°F (121°C), and the lamina strengths listed in table 4.1 are for a temperature of 70°F (21°C) and a moisture content of zero. Determine the internal pressure p that would cause failure of the vessel according

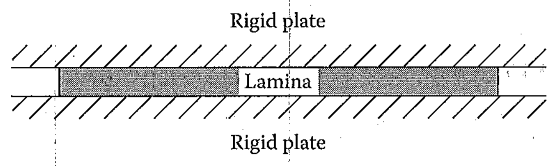

FIGURE 5.18
Lamina clamped between rigid plates in a mold.

to the Maximum Stress Criterion. Compare with the result from example 4.3.

8. A carbon/epoxy lamina is clamped between rigid plates in a mold (fig. 5.18) while curing at a temperature of 125°C. After curing, the lamina/mold assembly (still clamped together) is cooled from 125 to 25°C. The cooling process occurs in moist air and the lamina absorbs 0.5% of its weight in moisture. The lamina has the following properties:

$$E_1 = 140\,\text{GPa} \qquad \alpha_1 = -0.3\times10^{-6}\,/\,\text{K}$$
$$E_2 = 10\,\text{GPa} \qquad \alpha_2 = 28\times10^{-6}\,/\,\text{K}$$
$$\nu_{12} = 0.3 \qquad \beta_1 = 0$$
$$G_{12} = 7\,\text{GPa} \qquad \beta_2 = 0.44$$

Assuming that the lamina properties do not change over this temperature range and that the lamina is initially dry and stress free, determine the residual hygrothermal stresses in the lamina at 25°C for angles $\theta = 0°$ and 45°.

9. A unidirectional continuous fiber composite is to be made from T300 graphite fibers in a high-modulus (HM) epoxy matrix, and the composite is to have a longitudinal coefficient of thermal expansion of zero. Using the fiber and matrix properties in tables 3.1 and 3.2, determine the required fiber-volume fraction. Is this a practical composite? Sketch a graph showing the longitudinal CTE of the composite versus the fiber-volume fraction, and show the range of fiber-volume fractions over which the longitudinal CTE would be negative.

10. A unidirectional graphite/epoxy lamina having the properties described in problem 8 is to be designed to have a coefficient of thermal expansion of zero along a particular axis. Determine the required lamina orientation for such a design.

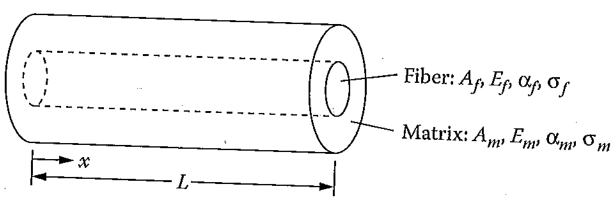

FIGURE 5.19
Representative volume element for problem 5.11.

11. A representative volume element (RVE) consisting of a cylindrical isotropic fiber embedded and perfectly bonded in a cylinder of isotropic matrix material is shown in figure 5.19. If the ends of the RVE at $x = 0$ and $x = L$ and the outer surface of the RVE are stress free and the RVE is subjected to a uniform temperature change ΔT, determine the fiber stress, σ_f, and the matrix stress, σ_m, along the fiber direction at the midpoint of the RVE (at $x = L/2$). Use a mechanics of materials approach and express answers in terms of the coefficients of thermal expansion α_f and α_m, the cross-sectional areas A_f and A_m, the Young's moduli E_f and E_m, and the temperature change, ΔT, where the subscripts f and m refer to fiber and matrix, respectively.

12. Samples of unidirectional Kevlar 49/epoxy and S-glass/epoxy composites are subjected to elevated temperatures in an oven and the resulting thermal strains are measured by using strain gages oriented along the 1 and 2 directions, as shown in figure 5.15. From the data in figure 5.15, estimate the longitudinal thermal expansion coefficient α_1 and the transverse thermal expansion coefficient α_2 for both materials.

13. A unidirectional 45° off-axis E-glass/epoxy composite lamina is supported on frictionless rollers between rigid walls as shown in figure 5.20. The lamina is fixed against displacements in the y direction, but is free to move in the x direction. Determine all of the lamina strains associated with the x,y axes if the lamina is heated from 20 to 120°C. The required properties for E-glass/epoxy are given in tables 2.2 and 5.3.

14. A hybrid unidirectional E-glass/T-300 carbon/IMHS epoxy composite is to be designed to have an overall longitudinal thermal expansion coefficient of zero in order to insure the best possible thermal stability under varying service temperatures. It is also required that in order to ensure that the material will be sufficiently stiff, the volume fraction of T-300 carbon fibers is to be twice the volume fraction of the E-glass fibers. (a) Using the

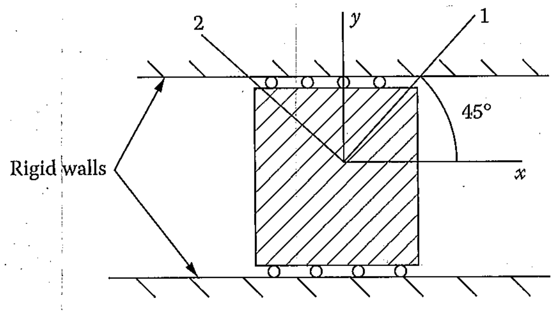

FIGURE 5.20
Off-axis composite lamina fixed between rigid walls for problem 5.13.

tables 3.1 and 3.2 and neglecting voids in the material, determine the required volume fractions of T-300 carbon fibers and E-glass fibers. (b) Assuming that the T-300 carbon fibers and E-glass fibers have approximately the same diameters, and that the fibers are packed in a triangular array, is the composite design of part (a) feasible?

15. An orthotropic lamina has thermal expansion coefficients $\alpha_1 = -4.0\ (10^{-6})$ m/m/K and $\alpha_2 = 79(10^{-6})$ m/m/K. Determine (a) the angle θ for which the thermal expansion coefficient $\alpha_y = 0$, and (b) the angle θ for which the thermal expansion coefficient α_{xy} has its maximum value.
16. A carbon/epoxy lamina having the properties listed in problem 8 is clamped between two rigid plates as shown in figure 5.18. If the lamina is heated from 20 to 120°C, determine the thermal stresses associated with the principal material axes of the lamina.

References

1. Browning, C.E., Husman, G.E., and Whitney, J.M. 1977. Moisture effects in epoxy matrix composites. *Composite Materials: Testing and Design: Fourth Conference*. ASTM STP 617, pp. 481–496, American Society for Testing and Materials, Philadelphia, PA.
2. Gibson, R.F., Yau, A., Mende, E.W., and Osborn, W.E. 1982. The influence of environmental conditions on the vibration characteristics of chopped fiber reinforced composite materials. *Journal of Reinforced Plastics and Composites*, 1(3), 225–241.
3. Shen, C.H. and Springer, G.S. 1976. Moisture absorption and desorption of composite materials. *Journal of Composite Materials*, 10, 2–20.

4. Jost, W. 1952. *Diffusion in Solids, Liquids, Gases*. Academic Press, Inc., New York.
5. Loos, A.C., Springer, G.S., Sanders, B.A., and Tung, R.W. 1981. Moisture absorption of polyester-E glass composites, in Springer, G.S. ed., *Environmental Effects on Composite Materials*, pp. 51–62. Technomic Publishing Co., Lancaster, PA.
6. Cai, L.W. and Weitsman, Y. 1994. Non-Fickian moisture diffusion in polymeric composites. *Journal of Composite Materials*, 28(2), 130-154.
7. Weitsman, Y. 2000. Effects of fluids on polymeric composites – A review, in Kelly, A. and Zweben, C. editors-in-chief, *Comprehensive Composite Materials*: Talreja, R. and Manson, J.-A.E. eds., *Polymeric Matrix Composites*, vol. 2, pp. 369–401. Elsevier Science Publishers, Amsterdam.
8. Weitsman, Y. and Elahi, M. 2000. Effects of fluids on the deformation, strength and durability of polymeric composites – An overview. *Mechanics of Time-Dependent Materials*, 4, 107–126.
9. Chamis, C.C. and Sinclair, J.H. 1982. Durability/life of fiber composites in hygrothermomechanical environments, in Daniel, I.M. ed., *Composite Materials: Testing and Design (Sixth Conference)*, ASTM STP 787, pp. 498–512. American Society for Testing and Materials, Philadelphia, PA.
10. Chamis, C.C. 1987. Simplified composite micromechanics equations for mechanical, thermal, and moisture-related properties, in Weeton, J.W. et al. eds., *Engineers' Guide to Composite Materials*, pp. 3-8–3-24. ASM International, Materials Park, OH.
11. DeIasi, R. and Whiteside, J.B. 1987. Effect of moisture on epoxy resins and composites, in Vinson, J.R. ed., *Advanced Composite Materials — Environmental Effects*, ASTM STP 658, pp. 2–20. American Society for Testing and Materials, Philadelphia, PA.
12. Loos, A.C. and Springer, G.S. 1981. Moisture absorption of graphite/epoxy composites immersed in liquids and in humid air, in Springer, G.S. ed., *Environmental Effects on Composite Materials*, pp. 34–50. Technomic Publishing Co., Lancaster, PA.
13. Fahmy, A.A. and Hurt, J.C. 1980. Stress dependence of water diffusion in epoxy resins. *Polymer Composites*, 1(2), 77–80.
14. Marom, G. and Broutman, L.J. 1981. Moisture penetration into composites under external stress. *Polymer Composites*, 2(3), 132–136.
15. Weitsman, Y. 1987. Stress assisted diffusion in elastic and viscoelastic materials. *Journal of the Mechanics and Physics of Solids*, 35(1), 73–94.
16. Cairns, D.S. and Adams, D.F. 1984. Moisture and thermal expansion properties of unidirectional composite materials and the epoxy matrix, in Springer, G.S. ed., *Environmental Effects on Composite Materials*, vol. 2, pp. 300–316. Technomic Publishing Co., Lancaster, PA.
17. Graves, S.R. and Adams, D.F. 1981. Analysis of a bonded joint in a composite tube subjected to torsion. *Journal of Composite Materials*, 15, 211–224.
18. Adams, D.F., Carlsson, L.A., and Pipes, R.B., 2003. *Experimental Characterization of Advanced Composite Materials*. CRC Press, Boca Raton, FL.
19. Schapery, R.A. 1968. Thermal expansion coefficients of composite materials based on energy principles. *Journal of Composite Materials*, 2(3), 380–404.

20. Hashin, Z. 1979. Analysis of properties of fiber composites with anisotropic constituents. *Journal of Applied Mechanics*, 46, 543–550.
21. Rosen, B.W. 1987. Composite materials analysis and design, in Reinhart, T.J. ed., *Engineered Materials Handbook*, vol. 1, *Composites*, Sec. 4. ASM International, Materials Park, OH.
22. Ishikawa, T., Koyama, K., and Kobayashi, S. 1978. Thermal expansion coefficients of unidirectional composites. *Journal of Composite Materials*, 12, 153–168.
23. Ashton, J.E., Halpin, J.C., and Petit, P.H. 1969. *Primer on Composite Materials: Analysis*. Technomic Publishing Co., Lancaster, PA.
24. Hopkins, D.A. and Chamis, C.C. 1988. A unique set of micromechanics equations for high temperature metal matrix composites, in DiGiovanni, P.R. and Adsit, N.R. eds., *Testing Technology of Metal Matrix Composites*, ASTM STP 964, pp. 159–176. American Society for Testing and Materials, Philadelphia, PA.

6

Analysis of a Discontinuous Fiber-Reinforced Lamina

6.1 Introduction

In chapter 2 to chapter 5, we have discussed the analysis of continuous fiber–reinforced composites. The effects of fiber discontinuity or fiber length on composite mechanical behavior were not taken into account in these analyses since it was assumed that the fibers extended from one end of the lamina to the other end. This chapter is concerned with the mechanical behavior of laminae having discontinuous fiber or short-fiber reinforcement.

Short fiber–reinforced composites are typically not as strong or as stiff as continuous fiber–reinforced composites and are not likely to be used in critical structural applications such as aircraft primary structures (but this may change as the full potential of new discontinuous reinforcements such as carbon nanotubes is realized). On the other hand, short fiber composites do have several attractive characteristics that make them worthy of consideration for other applications. For example, in components having complex geometrical contours, continuous fibers may not be practical because they may not conform to the desired shape without being damaged or distorted from the desired pattern. However, short fibers can be easily mixed with the liquid matrix resin, and the resin/fiber mixture can be injection or compression molded to produce parts having complex shapes. Such processing methods are also fast and inexpensive, which makes them very attractive for high-volume applications. Composites having randomly oriented, short fiber reinforcement are nearly isotropic, whereas unidirectional continuous fiber composites are highly anisotropic. In many applications the advantages of low cost, ease of fabricating complex parts, and isotropic behavior are enough to make short fiber composites the material of choice. This has been especially true since the 1991 discovery of carbon nanotubes (the "ultimate short fibers," which are currently believed to be the strongest materials that mankind is capable of producing), and much attention has been directed to their use as reinforcement in composites.

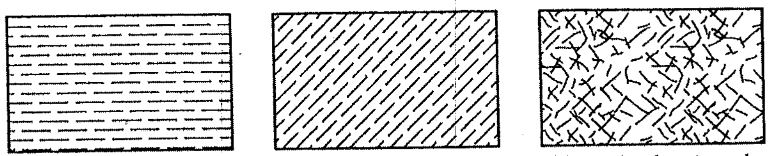

(a) Aligned discontinuous fibers (b) Off-axis aligned discontinuous fibers (c) Randomly oriented discontinuous fibers

FIGURE 6.1
Types of discontinuous fiber reinforcement.

Short fiber composites with three types of fiber reinforcement will be considered here, as shown in figure 6.1: aligned discontinuous fibers, off-axis aligned discontinuous fibers, and randomly oriented discontinuous fibers. Nanofibers and nanotubes can be used in any of these three arrangements, but because of their extremely tiny dimensions, they are most often randomly oriented in all three dimensions. Although the randomly oriented, short fiber composites are the most widely used of the three types, the development of the analytical models logically begins with the simplest case — aligned short fibers.

6.2 Aligned Discontinuous Fibers

The analysis of the specially orthotropic aligned discontinuous fiber composite in figure 6.1(a) begins with the selection of a representative volume element (RVE) consisting of a short fiber embedded in a cylinder of matrix material, as shown in figure 6.2. Several models are based on the simplified

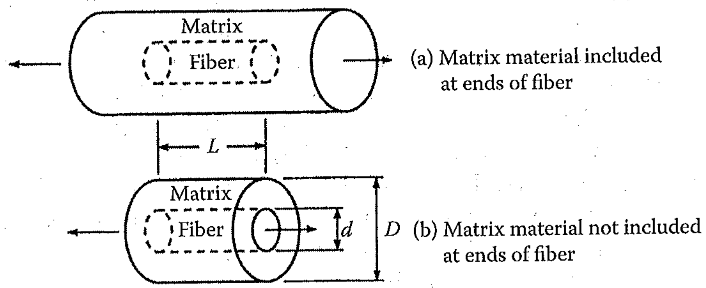

FIGURE 6.2
RVEs for aligned discontinuous fiber composite.

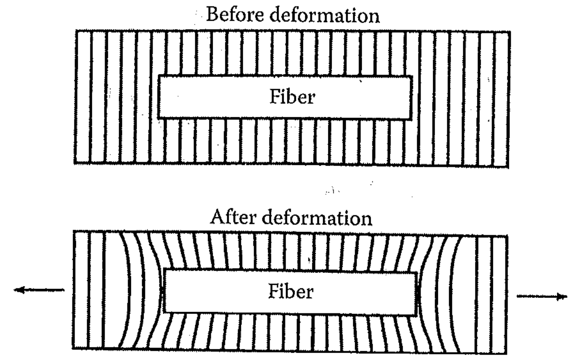

FIGURE 6.3
Schematic representation of matrix shear deformation in a short fiber composite.

RVE in figure 6.2(b), which does not include matrix material at the ends of the fiber as the model in figure 6.2(a) does. Before beginning the analysis, however, it is instructive to consider the geometry of deformation in the RVE of figure 6.2(a). As shown by the grid lines before and after deformation in figure 6.3, the stiffness mismatch between fiber and matrix ($E_f \gg E_m$) leads to large shear deformations near the fiber ends but no shear deformation at the middle of the fiber. That is, if $E_f = E_m$, there is no mismatch in stiffness between fiber and matrix, and no interfacial shear takes place. As we will see later, the stress transfer between matrix and fiber occurs primarily through interfacial shear, which is the greatest near the fiber ends. On the other hand, the normal stress in the fiber builds from a minimum at the fiber ends to a maximum at the middle of the fiber.

6.2.1 Stress and Strength Analysis

The above observations based on the geometry of deformation will now be confirmed by considering the free-body diagram of a differential element of the fiber from the RVE, as shown in figure 6.4. For static equilibrium of the forces along the x direction,

$$\sum F_x = (\sigma_f + d\sigma_f)\frac{\pi d^2}{4} - \sigma_f\frac{\pi d^2}{4} - \tau(\pi d)dx = 0 \tag{6.1}$$

where

σ_f = fiber normal stress along the x direction at a distance x from end of fiber

F_x = force along the x direction

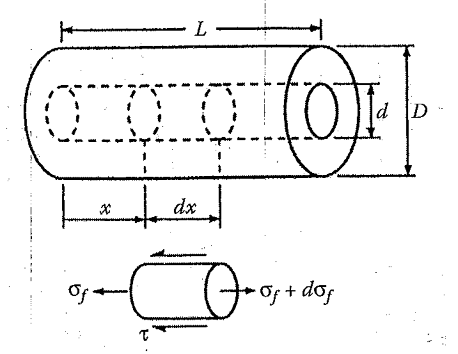

FIGURE 6.4
Stresses acting on a differential element of fiber.

τ = interfacial shear stress at a distance x from end of fiber
d = fiber diameter, a constant
dx = length of differential element
$d\sigma_f$ = differential change in stress σ_f

Simplifying and rearranging the above equation, we get the differential equation relating the rate of change of the fiber normal stress along the x direction to the interfacial shear stress:

$$\frac{d\sigma_f}{dx} = \frac{4\tau}{d} \tag{6.2}$$

Separating variables and integrating, we find that

$$\int_{\sigma_0}^{\sigma_f} d\sigma_f = \frac{4}{d}\int_0^x \tau dx \tag{6.3}$$

It is commonly assumed that essentially all of the stress transfer from matrix to fiber occurs by interfacial shear around the periphery of the fiber, and that the fiber normal stress, σ_0, which is transferred across the ends of the fiber, is negligible. With this assumption, equation (6.3) becomes

$$\sigma_f = \frac{4}{d}\int_0^x \tau dx \tag{6.4}$$

Thus, if we want to determine the fiber stress, σ_f, we must know the interfacial shear stress, τ, as a function of the distance x. Two basic

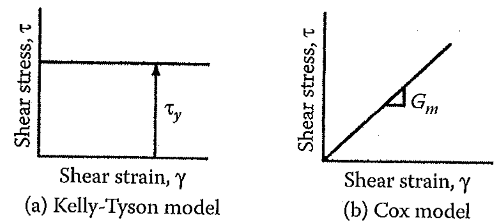

FIGURE 6.5
Assumed stress–strain curves for matrix material in the Kelly–Tyson and Cox models.

approaches have been proposed, both of which are based on assumptions regarding the behavior of the matrix material. Kelly and Tyson [1] assumed that the matrix is rigid plastic, as shown in the stress–strain curve in figure 6.5(a). Cox [2] assumed that the matrix is linear elastic, as shown in figure 6.5(b). Both models are based on the assumption of linear elastic fibers. We will consider both models, but it is convenient to use the Kelly–Tyson model for illustrative purposes at this point. The Kelly–Tyson model is much simpler than the Cox model because the interfacial shear stress, τ, is everywhere equal to the matrix yield stress in shear, τ_y. Thus, for the Kelly–Tyson model, the resulting fiber stress from equation (6.4) is now

$$\sigma_f = \frac{4}{d}\tau_y x \tag{6.5}$$

This equation tells us that the fiber stress varies linearly with the distance from the fiber end, but we also know that the fiber stress distribution must be symmetric about $x = L/2$. Since it has been assumed that $\sigma_f = \sigma_0 = 0$ at $x = 0$ and, by symmetry, at $x = L$, the fiber stress distribution and the corresponding shear stress distribution must be as shown in figure 6.6. The stress distributions in figure 6.6 are actually valid only for fibers having lengths less than a certain value, as we will see later. The maximum fiber stress for such a fiber occurs at $x = L/2$ and is given by

$$\sigma_{f\,max} = \frac{4}{d}\tau_y \frac{L}{2} = \frac{2\tau_y L}{d} \tag{6.6}$$

The maximum fiber stress cannot keep increasing indefinitely as the fiber length L is increased, however. If the fiber is assumed to be elastic, $\sigma_{f\,max}$ cannot exceed the value $E_{f1}\sigma_{c1}/E_1$, which is the fiber stress in a continuous fiber composite under longitudinal composite stress, σ_{c1} (recall sec. 3.2.1). Thus, as $\sigma_{f\,max}$ approaches the limiting value $E_{f1}\sigma_{c1}/E_1$, the fiber length, L,

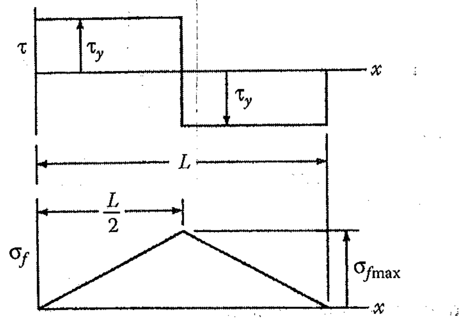

FIGURE 6.6
Variation of interfacial shear stress, τ, and fiber normal stress, σ_f, with distance along the fiber according to the Kelly–Tyson model.

approaches a value L_i, which has been referred to as the "ineffective length" [3], or the "load transfer length" [4]. The equation for L_i is therefore

$$L_i = \frac{dE_{f1}\sigma_{c1}}{2\tau_y E_1} \tag{6.7}$$

The effect of increasing fiber length on the fiber stress and shear stress distributions is shown graphically in figure 6.7. Note that no matter how long the fiber is, the load transfer between fiber and matrix (by virtue of the interfacial shear stress, τ) only occurs over the length, L_i. The length

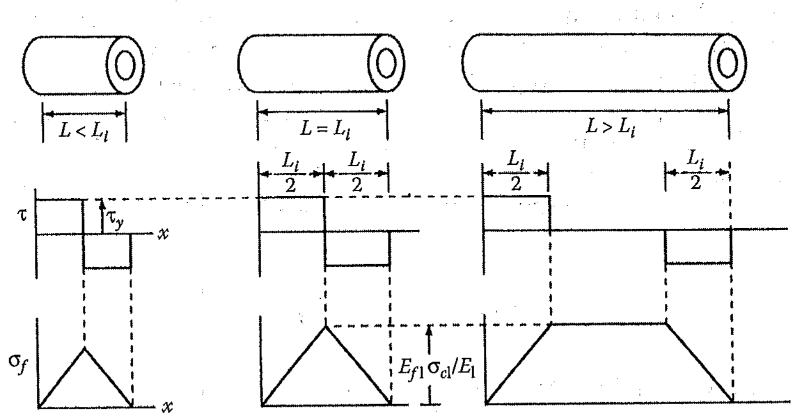

FIGURE 6.7
Effect of fiber length on stress distributions along the fiber according to the Kelly–Tyson model.

L_i has been referred to as the "ineffective length" because the fiber stress is less than its maximum value for this portion of the fiber. The term "load transfer length" comes from the fact that the load transfer between fiber and matrix only occurs over this portion of the fiber. Although these results are for the Kelly–Tyson model, similar results are obtained from the Cox model.

Another limiting value of the fiber stress occurs when $\sigma_{f\max}$ is equal to the fiber tensile strength, $s_{f1}^{(+)}$. In this case, the applied composite stress is such that

$$\frac{E_{f1}\sigma_{c1}}{E_1} = \sigma_{f\max} = s_{f1}^{(+)} \tag{6.8}$$

The corresponding fiber length now becomes $L = L_c$, where L_c is referred to as the "critical length." For this condition, substitution of equation (6.8) in equation (6.6) yields the equation for the critical length as

$$L_c = \frac{ds_{f1}^{(+)}}{2\tau_y} \tag{6.9}$$

The critical length has important implications for the calculation of longitudinal composite strength. Recall from equation (3.19) that the average longitudinal composite stress for loading along the fiber direction is given by

$$\bar{\sigma}_{c1} = \bar{\sigma}_{f1}v_f + \bar{\sigma}_{m1}v_m \tag{3.19}$$

Then equation (4.21) for longitudinal composite strength of a continuous fiber–reinforced lamina was developed from equation (3.19) by assuming that the continuous fibers were uniformly stressed along their entire lengths, and that the fibers failed before the matrix when the average fiber stress $\bar{\sigma}_{f1}$ reached the fiber tensile strength $s_{f1}^{(+)}$. However, in the case of discontinuous fibers, it should be clear from the previous developments in this section that the fibers are not uniformly stressed along their entire lengths, and that the fiber length must be taken into account. For the discontinuous fibers, the average longitudinal fiber stress in equation (3.19) may be found from

$$\bar{\sigma}_{f1} = \frac{\int_0^{L/2} \sigma_{f1}dx}{L/2} \tag{6.10}$$

Evaluation of this integral depends on the fiber length. From figure 6.7, it can be seen that for $L \leq L_i$, the fiber stress varies linearly with x as

$$\sigma_{f1} = \frac{\sigma_{f\,max} x}{L_i/2} \tag{6.11}$$

and equation (6.10) becomes

$$\bar{\sigma}_{f1} = \frac{\int_0^{L/2} [\sigma_{f\,max} x/(L_i/2)]dx}{L/2} = \frac{\sigma_{f\,max} L}{2L_i} \tag{6.12}$$

whereas for the case $L \geq L_i$, the corresponding average stress is

$$\bar{\sigma}_{f1} = \frac{\int_0^{L_i/2} [\sigma_{f\,max} x/(L_i/2)]dx + \int_{L_i/2}^{L/2} \sigma_{f\,max} dx}{L/2} = \left(1 - \frac{L_i}{2L}\right)\sigma_{f\,max} \tag{6.13}$$

It should be kept in mind here that L is the variable fiber length and L_i is the specific value of fiber length over which load transfer takes place. Therefore for the specific case of fiber failure and corresponding composite failure, substitution of the conditions $\sigma_{f\,max} = s_{f1}^{(+)}$, $\bar{\sigma}_{c1} = s_L^{(+)}$, $\bar{\sigma}_m = s_{mf1}^{(+)}$, and $L_i = L_c$ along with equation (6.12) in equation (3.19) gives the longitudinal composite strength as

$$s_L^{(+)} = \frac{s_{f1}^{(+)} L}{2L_c} v_f + s_{mf1}^{(+)}(1 - v_f) \quad \text{for } L \leq L_c \tag{6.14}$$

while similar substitution of the conditions $\sigma_{f\,max} = s_{f1}^{(+)}$, $\bar{\sigma}_{c1} = s_L^{(+)}$, $\bar{\sigma}_m = s_{mf1}^{(+)}$, and $L_i = L_c$ along with equation (6.13) in equation (3.19) gives the longitudinal composite strength as

$$s_L^{(+)} = \left(1 - \frac{L_c}{2L}\right) s_{f1}^{(+)} v_f + s_{mf1}^{(+)}(1 - v_f) \quad \text{for } L \geq L_c \tag{6.15}$$

It has been assumed in equation (6.14) and equation (6.15) that the average stress in the matrix at fiber failure is $\bar{\sigma}_m = s_{mf1}^{(+)}$ in accordance with figure 4.9(a) and equation (4.21). Note that, when $L \gg L_c$, equation (6.15) approaches equation (4.21) for continuous fibers.

Alternatively, equation (6.9) can be rearranged to give the interfacial shear strength, τ_y, corresponding to the critical length

$$\tau_y = \frac{d s_{f1}^{(+)}}{2L_c} \tag{6.16}$$

This equation has been used by Drzal et al. [5,6] and others to determine the interfacial shear strength from measurements of critical length. In such an experiment, a specimen consisting of a single fiber embedded in a strip of translucent matrix material is mounted under a microscope and then subjected to an increasing tensile load. Once the fiber stress reaches $s_{f1}^{(+)}$, the fiber breaks up into segments having a statistical distribution about the critical length, L_c, and the corresponding statistical parameters describing the interfacial shear strength are calculated using equation (6.9).

6.2.2 Modulus Analysis

Expressions for the longitudinal modulus of the aligned discontinuous fiber composite can be found using either the Kelly–Tyson model or the Cox model, but only the derivation of the Cox model, extended further by Kelly [7], will be discussed here. A similar model, which is often referred to as a "shear lag" model, was developed by Rosen [8]. For the RVE of figure 6.2(b), recall from equation (6.2) that the rate of change of the axial load in the fiber with respect to distance along the fiber is a linear function of the interfacial shear stress. Cox further assumed that the interfacial shear stress is proportional to the difference between u and υ, where u is the axial displacement at a point in the fiber and υ is the axial displacement the matrix would have at the same point in the RVE with no fiber present. Thus, the rate of change of the fiber axial load P is given by

$$\frac{dP}{dx} = H(u - \upsilon) \tag{6.17}$$

where H is a proportionality constant to be determined from geometrical and material property data. Differentiating equation (6.17) once, we find that

$$\frac{d^2P}{dx^2} = H\left(\frac{du}{dx} - \frac{d\upsilon}{dx}\right) = H\left(\frac{p}{A_f E_{f1}} - e\right) \tag{6.18}$$

where the expression

$$\frac{du}{dx} = \frac{P}{A_f E_{f1}}$$

is taken from elementary mechanics of materials and

$$\frac{d\upsilon}{dx} = e$$

is the matrix strain with no fiber present.

Equation (6.18) can be rearranged in the standard form of a second-order differential equation with constant coefficients as

$$\frac{d^2P}{dx^2} - \beta^2 P = -He \tag{6.19}$$

where

$$\beta^2 = \frac{H}{A_f E_{f1}}$$

The solution to equation (6.19) is of the form

$$P = P_p + P_h \tag{6.20}$$

where

P_p = particular solution = $A_f E_{f1} e$
P_h = homogeneous solution = $R \sinh \beta x + S \cosh \beta x$

The coefficients R and S must be determined from the boundary conditions $P = 0$ at $x = 0$ and $x = L$. After using trigonometric identities and further manipulation, the resulting fiber stress is

$$\sigma_f = \frac{P}{A_f} = E_{f1} e \left[1 - \frac{\cosh \beta(0.5L - x)}{\cosh(0.5\beta L)}\right] \tag{6.21}$$

The average fiber stress is then

$$\bar{\sigma}_f = \frac{\int_0^{L/2} \sigma_f dx}{L/2} = E_{f1} e \left[1 - \frac{\tanh(\beta L/2)}{\beta L/2}\right] \tag{6.22}$$

From the equilibrium of the composite for longitudinal loading, recall the rule of mixtures for stress (eq. [3.19]), which is also valid for the RVE of figure 6.2(b):

$$\bar{\sigma}_{c1} = \bar{\sigma}_{f1} \upsilon_f + \bar{\sigma}_m \upsilon_m \tag{6.23}$$

Substituting equation (6.22) in equation (6.23), dividing equation (6.23) by e, assuming that the applied composite stress produces a strain, e, in composite, fiber, and matrix, and using Hooke's law for composite and matrix, we find the equation for the longitudinal modulus of the Cox model:

$$E_{c1} = E_{f1} \left[1 - \frac{\tanh(\beta L/2)}{\beta L/2}\right] \upsilon_f + E_m \upsilon_m \tag{6.24}$$

Note that the assumption of equal strains in fiber and matrix here does not violate the original assumptions about u and υ being different, because υ is the displacement in a piece of unreinforced matrix material. The term inside the brackets represents the effect of fiber length on the composite modulus.

The parameter β in the above equations and the interfacial shear stress, τ, can be determined by considering the shear strain in the matrix, as shown by Kelly [7]. The results are

$$\beta^2 = \frac{2\pi G_m}{A_f E_{f1} \ln(D/d)} \tag{6.25}$$

and

$$\tau = \frac{d E_{f1} e \beta}{4} \left[\frac{\sinh[\beta(0.5L - x)]}{\cosh(0.5\beta L)}\right] \tag{6.26}$$

where G_m is the matrix shear modulus and D is the outside diameter of the RVE, as shown in figure 6.2. The predicted variations of the fiber stress and the interfacial shear stress from the Cox model when the fiber length $L < L_i$ are shown schematically in figure 6.8. Notice the difference between these stress distributions and the ones from the Kelly–Tyson model in figure 6.6. For the Cox stresses evaluated at the midpoint of the fiber ($x = L/2$), as $L \to L_i$, the term in brackets in equation (6.21) approaches the value 1.0, whereas the term in brackets in equation (6.26) approaches zero.

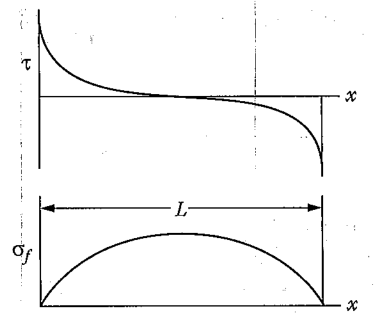

FIGURE 6.8
Variation of interfacial shear stress, τ, and fiber normal stress, σ_f, with distance along the fiber according to the Cox model.

Another variation on the Cox model was developed by Gibson et al. [9], who used the Cox stresses, σ_f and τ, in a strain method similar to that outlined in equation (3.24) and equation (3.25). The longitudinal modulus calculated by the energy method was found to agree closely with equation (6.24), and the predicted variation of E_{C1} with fiber aspect ratio, L/d, is shown for several composites in figure 6.9. Notice that as the fiber length $L \to \infty$, $E_{C1} \to E_{f1}\upsilon_f + E_m\upsilon_m$, and that as $L \to 0$, $E_{C1} \to E_m\upsilon_m$. It is also interesting to see that the fiber length does not have to be very large relative to the fiber diameter in order to bring the modulus E_{C1} very close to the limiting value given by the rule of mixtures.

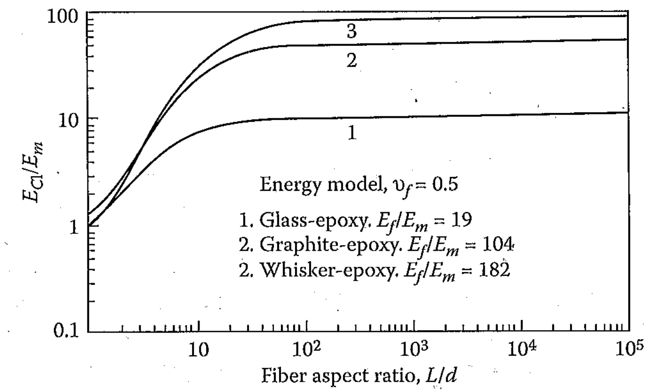

FIGURE 6.9
Variation of modulus ratio, E_{C1}/E_m, with fiber aspect ratio, L/d, for several composites. (From Gibson, R.F., Chaturvedi, S.K., and Sun, C.T. 1982. *Journal of Materials Science*, 17, 3499–3509. Reprinted by permission of Chapman & Hall.)

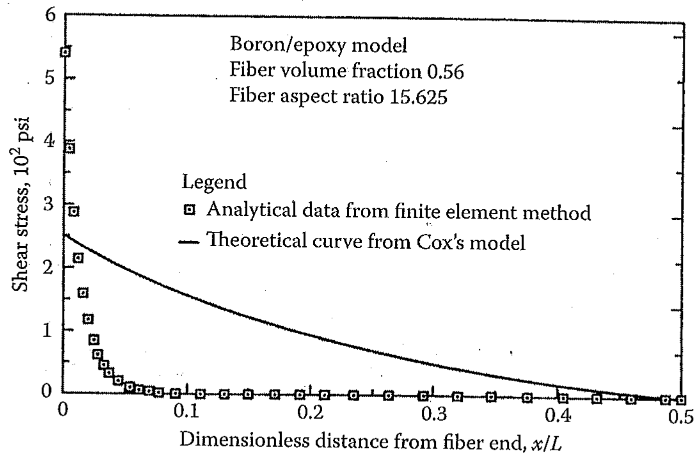

FIGURE 6.10
Predicted shear stress distributions along the fiber from finite element analysis and the Cox model. (From Hwang, S.J. 1985. Finite element modeling of damping in discontinuous fiber composites. M.S. Thesis, University of Idaho, Moscow, ID. With permission.)

Although the Kelly–Tyson model and the Cox model both provide valuable insight into the concepts of load transfer, fiber length effects, and strength and modulus analysis, neither model accurately predicts the stress distributions. For example, more recent results from finite element analyses [10,11] and experimental photoelasticity [7,12,13] indicate that both the magnitude and the rate of change of the interfacial shear stresses near the end of the fiber are much higher than those predicted by the Kelly–Tyson or Cox models. A typical comparison of predicted shear stress distributions along the fiber from finite element analysis and from the Cox model is shown in figure 6.10. The finite element predictions of Sun and Wu [11] also showed good agreement with experimental photoelasticity results. Finite element analyses have also been used to study the effects of different fiber end shapes on the stress distributions [10,11].

It is important to remember that both the Kelly–Tyson and the Cox models were derived for the RVE in figure 6.2(b), which does not include matrix material at the ends of the fiber. One result is that the actual modulus values are lower than predicted by equation (6.24). For example, the experimental results of Suarez et al. [14] on aligned discontinuous graphite/epoxy composites having various fiber aspect ratios, L/d, are shown in figure 6.11. The experimental modulus data at different fiber aspect ratios in figure 6.11 were obtained from the test specimens shown schematically in figure 6.12, which were manufactured using conventional

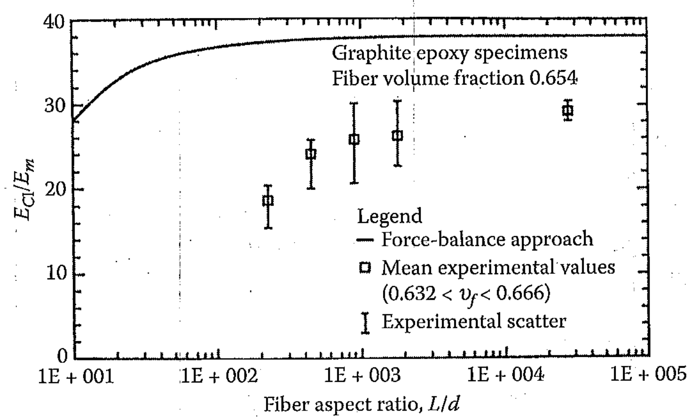

FIGURE 6.11
Comparison of measured and predicted (Cox model) longitudinal moduli of aligned discontinuous fiber graphite/epoxy for various fiber aspect ratios. $(L/d)_{eff} = L/d$. (From Suarez, S.A., Gibson, R.F., Sun, C.T., and Chaturvedi, S.K. 1986. *Experimental Mechanics*, 26(2), 175–184. With permission.)

unidirectional prepreg tape that had been cut at intervals of length L before being processed with a standard autoclave-style cure cycle. The measured moduli are seen to be well below the predicted curve from the Cox model. In order to shift the predicted curve to match the experimental results better, Suarez et al. introduced the concept of an "effective fiber

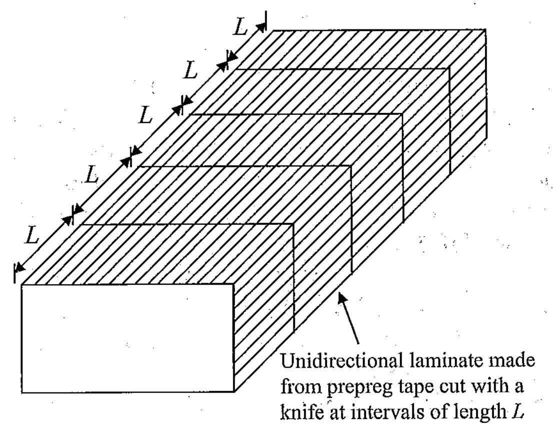

FIGURE 6.12
Aligned discontinuous fiber composite test specimen fabricated from unidirectional prepreg tape cut at intervals of length L before curing.

aspect ratio," $(L/d)_{eff}$, which would account for the fact that the reinforcement was not a single fiber but, rather, a bundle of fibers having an aspect ratio lower than that of a single fiber.

The effective fiber aspect ratio is defined as

$$(L/d)_{eff} = Z(L/d) \tag{6.27}$$

where Z is a curve-fitting parameter that accomplishes a horizontal shift of the curve of E_{C1} versus L/d. Before the horizontal shift, the predicted curve was shifted vertically by using a reduced fiber modulus to account for possible degradation of fiber properties or fiber misalignment during fabrication. The results of vertical and horizontal shifting of the graphite/epoxy curve of figure 6.11 are shown in figure 6.13, and the agreement is very good. Similar results were reported for aramid/epoxy and boron/epoxy. This approach did not take into account the matrix material between the fiber ends, however.

Hwang and Gibson [15] studied the effect of the fiber end gap on the composite modulus by using both finite element analysis and a modified Cox model. The modified Cox model consists of the Cox model (fig. 6.2[b]) with one piece of matrix material attached on each end, as shown schematically in figure 6.14. Following the development of equation (3.36) for the series arrangement of elements under longitudinal stress, with the

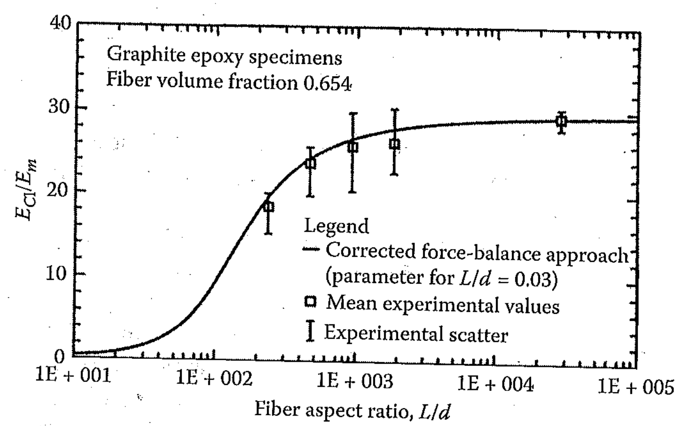

FIGURE 6.13
Comparison of measured and predicted (Cox model corrected for fiber aspect ratio) longitudinal moduli of aligned discontinuous fiber graphite/epoxy for various fiber aspect ratios. $(L/d)_{eff} = 0.03L/d$. (From Suarez, S.A., Gibson, R.F., Sun, C.T., and Chaturvedi, S.K. 1986. *Experimental Mechanics*, 26(2), 175–184. With permission.)

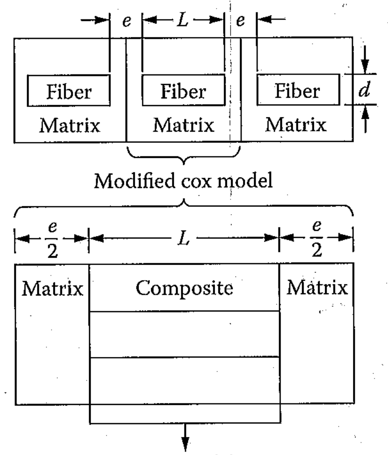

FIGURE 6.14
Modified Cox model including matrix material at ends of fiber. (From Hwang, S.J. and Gibson, R.F. 1987. *Journal of Engineering Materials and Technology*, 109, 47–52. Reprinted by permission of ASME.)

assumption of equal stresses in each element, the modified Cox modulus is

$$\frac{1}{E_{MC1}} = \frac{\upsilon_{C1}}{E_{C1}} + \frac{\upsilon_m}{E_m} = \frac{L/(L+e)}{E_{C1}} + \frac{e/(L+e)}{E_m} \tag{6.28}$$

where

E_{MC1} = longitudinal modulus of the modified Cox model
υ_{C1} = volume fraction of the Cox model in the modified Cox model
L = length of the Cox model
e = distance between fiber ends in the modified Cox model
$L + e$ = length of the modified Cox model

Figure 6.15 shows a comparison of predictions from a finite element model and the modified Cox model, with experimental data for boron/epoxy. Micromechanical predictions using the finite element method (FEM) in figure 6.15 were obtained using quarter domain models from RVEs of discontinuous aligned composites, as shown schematically in figure 6.16. The moduli of the finite element models having different fiber aspect ratios, L/d, and abutting fiber end separations, e, were calculated

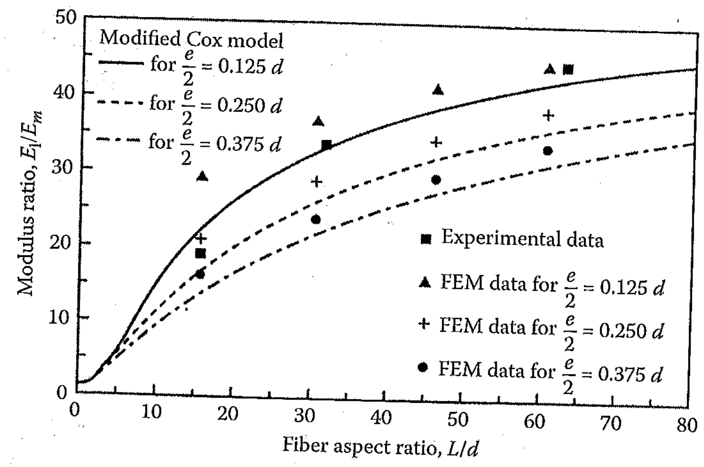

FIGURE 6.15
Comparison of predictions from the modified Cox model and finite element analysis with experimental data for boron/epoxy aligned discontinuous fiber composite at different fiber aspect ratios. (From Hwang, S.J. and Gibson, R.F. 1987. *Journal of Engineering Materials and Technology*, 109, 47–52. Reprinted by permission of ASME.)

using an equation similar to equation (3.58) and a procedure similar to that described in the discussion of equation (3.58). The modified Cox model shows good agreement with both the finite element analysis and experimental data.

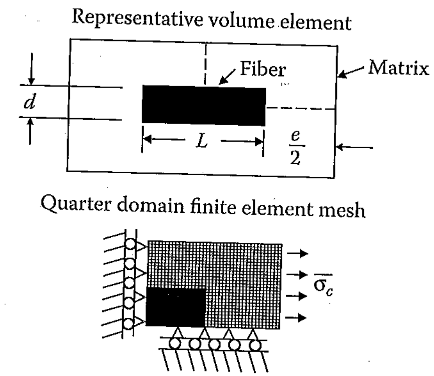

FIGURE 6.16
Quarter domain finite element model from RVE of discontinuous aligned fiber composite.

Halpin [16] has proposed a modification of the Halpin–Tsai equations (recall sec. 3.5) as another approach to estimating the longitudinal modulus of the aligned discontinuous fiber composite. The proposed equations are

$$\frac{E_1}{E_m} = \frac{1+\xi\eta\upsilon_f}{1-\eta\upsilon_f} \tag{6.29}$$

where

$$\eta = \frac{(E_{f1}/E_m)-1}{(E_{f1}/E_m)+\xi} \tag{6.30}$$

and the suggested value of the curve-fitting parameter is $\xi = 2L/d$. Figure 6.17 shows that the predictions from these equations give good agreement with experimental data. Halpin also concluded that E_2, G_{12}, and υ_{12} are not significantly affected by the fiber length [16]. Thus, equation (3.59) and equation (3.60) for E_2 in the continuous fiber case can also be used for the discontinuous fiber case. Similar equations can be used for G_{12}, as described in section 3.5, and equation (3.41) can be used for υ_{12}.

Other micromechanics equations for predicting stiffness of unidirectional short fiber composites are summarized in the review article by Tucker and Liang [17].

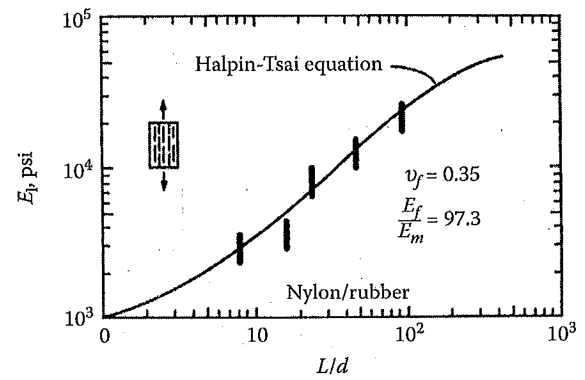

FIGURE 6.17
Dependence of longitudinal modulus on fiber aspect ratio for aligned discontinuous fiber nylon/rubber composite. Predictions from Halpin–Tsai equations are compared with experimental results. (From Halpin, J.C. 1969. *Journal of Composite Materials*, 3, 732–734. Reprinted by permission of Technomic Publishing Co.)

EXAMPLE 6.1

An aligned short fiber carbon/epoxy composite is to be fabricated so that it behaves as a continuous fiber composite with a composite modulus of $E_1 = 80$ GPa. The 0.01-mm-diameter fibers have a modulus of elasticity $E_{f1} = 240$ GPa and a tensile strength $s_{f1}^{(+)} = 2.5$ GPa. The epoxy matrix can be assumed to be a rigid–plastic material with a yield strength of 20 MPa in shear. Determine (a) the fiber length necessary to just reach the "continuous fiber stress" at the midpoint for a composite stress of 50 MPa and (b) the fiber length and the composite stress necessary to develop the ultimate tensile strength in the fiber.

Solution. (a) The "continuous fiber stress" is

$$\sigma_{f\,max} = E_{f1}\sigma_{c1}/E_1 = 240(50)/80 = 150 \text{ MPa}$$

and the corresponding fiber length from equation (6.6) is

$$L = d\sigma_{f\,max}/2\tau_y = 0.01(150)/2(20) = 0.0375 \text{ mm}$$

(b) The fiber length corresponding to a fiber stress $s_{f1}^{(+)}$ is found from equation (6.9):

$$L_c = d\sigma_{f1}^{(+)}/2\tau_y = 0.01(2500)/2(20) = 0.625 \text{ mm}$$

and the corresponding composite stress is

$$\sigma_{c1} = E_1\sigma_{f1}^{(+)}/E_{f1} = 80(2.5)/240 = 0.833 \text{ GPa} = 833 \text{ MPa}$$

EXAMPLE 6.2

The RVE for an aligned discontinuous fiber composite is shown in figure 6.14. Assume that the composite part of the RVE has length L and longitudinal coefficient of thermal expansion α_c, while the matrix material has total length e and longitudinal coefficient of thermal expansion α_m. Develop a micromechanical equation for predicting the effective longitudinal thermal expansion coefficient, α_{eff}, for the RVE, which has a total length $L + e$.

Solution. The overall thermal deformation of the RVE along the fiber direction due to a temperature change ΔT is given by

$$\delta_{total} = \alpha_{eff}(L+e)\Delta T$$

But for the series arrangement of the composite and matrix, geometric compatibility requires the total thermal expansion to be

$$\delta_{total} = \delta_c + \delta_m = \alpha_c L\Delta T + \alpha_m e\Delta T$$

where

δ_c = thermal deformation of composite part
δ_m = thermal deformation of matrix part

Equating the above two expressions for the total thermal deformation and solving for α_{eff}, it is seen that the effective thermal expansion coefficient for the RVE is

$$\alpha_{eff} = \frac{\alpha_c L + \alpha_m e}{L + e}$$

6.3 Off-Axis Aligned Discontinuous Fibers

6.3.1 Stress and Strength Analysis

The generally orthotropic aligned discontinuous fiber composite can be conveniently analyzed by using the RVE shown in figure 6.18, where the short fiber is oriented at an angle with the loading axis. Chon and Sun [18] used this RVE to develop a generalized shear-lag analysis of the off-axis

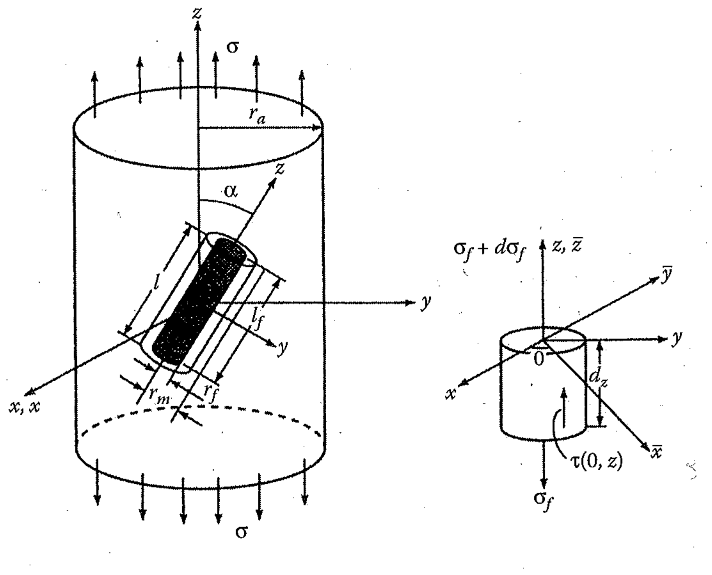

FIGURE 6.18
RVE for an off-axis short fiber composite. (From Chon, C.T. and Sun, C.T. 1980. *Journal of Materials Science*, 15, 931–938. Reprinted by permission of Chapman & Hall.)

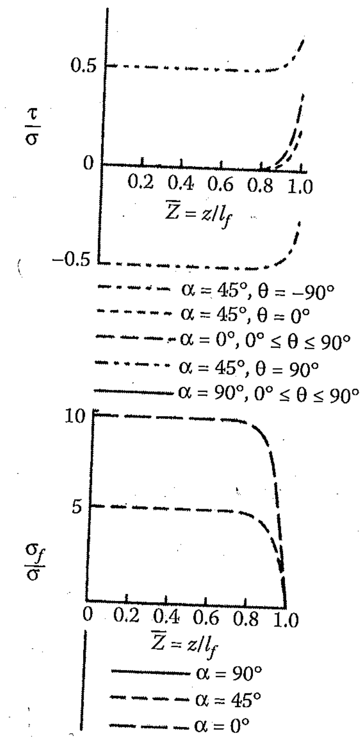

FIGURE 6.19
Variation of interfacial shear stress and fiber normal stress along the fiber for the Chon–Sun model at various off-axis angles. (From Chon, C.T. and Sun, C.T. 1980. *Journal of Materials Science*, 15, 931–938. Reprinted by permission of Chapman & Hall.)

short fiber composite. Only the key results will be summarized here as the equations are quite lengthy. The predicted variations of the interfacial shear stress and the fiber stress with the distance along the fiber for various angles are shown in figure 6.19. Note that the results from the Cox model (recall fig. 6.8) are recovered for the case of $\alpha = 0°$, and that the stress distribution curves are just shifted up or down as the angle α changes. Maximum values of shear stresses and fiber stresses normalized to the applied composite stress are shown for various angles α in figure 6.20. It is seen that the maximum interfacial shear stress, τ_{max}, occurs at some off-axis angle, that τ_{max} decreases with increasing E_f/G_m, and that the angle corresponding to τ_{max} increases with increasing E_f/G_m. Thus, the maximum interfacial shear stresses according to the Kelly–Tyson and Cox models are only maximum values for the case of $\alpha = 0°$. On the basis of these results, Chon and Sun suggest that if fiber failure is th

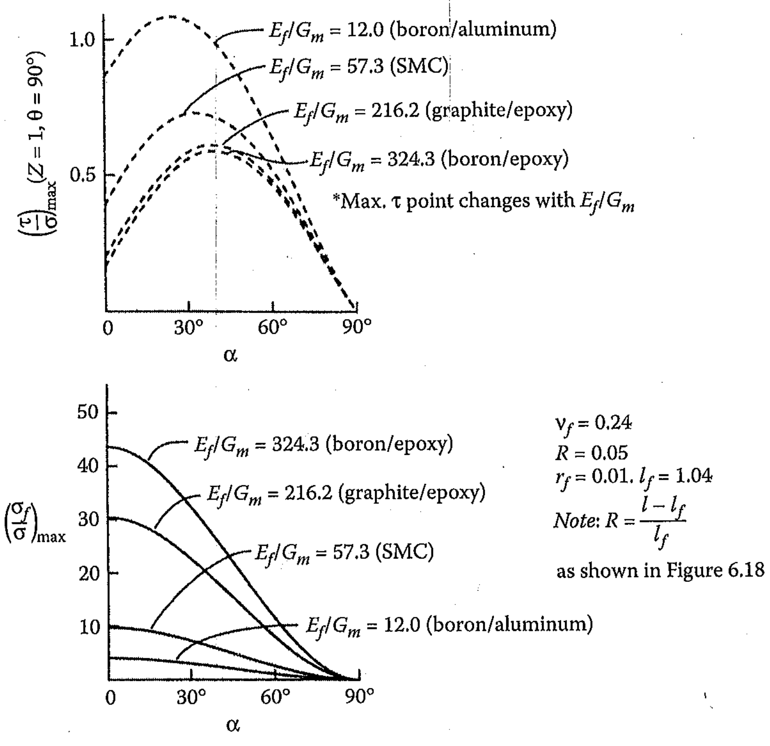

FIGURE 6.20
Variation of maximum interfacial shear stress and maximum fiber stress with off-axis angle from the Chon–Sun model. (From Chon, C.T. and Sun, C.T. 1980. *Journal of Materials Science*, 15, 931–938. Reprinted by permission of Chapman & Hall.)

failure mode, the matrix should be modified to reduce the ratio of E_f/G_m, but if failure is due to interfacial shear, E_f/G_m should be increased. In more recent work, finite element analyses of off-axis short fiber composites, including the effects of fiber angle and fiber end geometry, were conducted by Sun and Wu [11].

Calculation of the off-axis strength of an aligned discontinuous fiber composite can be accomplished by considering the off-axis uniaxial loading situation in figure 4.4, where the fibers are discontinuous. For example, if the corresponding off-axis stress state described in equations (4.3) is substituted in the Tsai–Hill criterion (eq. [4.14]), the result for the off-axis strength is

$$\sigma_x = \left[\frac{\cos^4\theta}{s_L^2} + \left(\frac{1}{s_{LT}^2} - \frac{1}{s_L^2}\right)\sin^2\theta\cos^2\theta + \frac{\sin^4\theta}{s_T^2}\right]^{-1/2} \tag{6.31}$$

In the evaluation of such equations for discontinuous fiber composites, it is often assumed that only the longitudinal strength, s_L, depends on fiber length, and that the other strengths are essentially independent of fiber length. In this case, depending on whether the fiber length is less than or greater than the critical length, either equation (6.14) or equation (6.15) can be used to estimate $s_L^{(+)}$, while the other strengths can be estimated using the micromechanical models for continuous fiber composites described in section 4.3.

6.3.2 Modulus Analysis

Elastic constants for the off-axis aligned discontinuous fiber composite may be estimated by using equations developed earlier in this chapter and in chapter 2 and chapter 3. Following the procedure outlined by Sun et al. [19] and Suarez et al. [14], the Cox model (eq. [6.24]) is used to find the longitudinal modulus along the 1 direction. The transverse modulus, E_2, the in-plane shear modulus, G_{12}, and the major Poisson's ratio, υ_{12}, are assumed to be independent of fiber length [16,17] and are calculated using the micromechanics equations developed in Chap. 3. The off-axis modulus of elasticity, E_x, is then found by substituting the Cox modulus, E_{C1}, for E_1 in the transformation equation (the first of eq. [2.39]), along with the calculated values of E_2, E_{12}, υ_{12}, and θ. The other off-axis properties E_y, G_{xy}, and υ_{xy} are found by using a similar approach. The resulting set of equations is of the form

$$\begin{aligned} E_x &= f_1(E_{C1}, E_2, G_{12}, \upsilon_{12}, \theta) \\ E_y &= f_2(E_{C1}, E_2, G_{12}, \upsilon_{12}, \theta) \\ G_{xy} &= f_3(E_{C1}, E_2, G_{12}, \upsilon_{12}, \theta) \\ \upsilon_{xy} &= f_4(E_{C1}, E_2, G_{12}, \upsilon_{12}, \theta) \end{aligned} \tag{6.32}$$

A comparison of the predicted off-axis modulus, E_x, for graphite/epoxy with experimental values for various angles, θ, is shown in figure 6.21. It should be mentioned that the good agreement between theory and experiment seen in figure 6.21 was not possible as long as the fibers were assumed to be isotropic. Once the orthotropic nature of the graphite fibers was taken into account (i.e., $E_{f1} >> E_{f2}$), the agreement between theory and experiment improved significantly. The same analysis was used to generate a tridimensional plot of the off-axis modulus, E_x, versus the fiber aspect ratio and the fiber orientation, as shown in figure 6.22. Due to the assumption that E_2, G_{12}, and υ_{12} are independent of the fiber aspect ratio, L/d has little effect on the calculated E_x for fiber orientations other than those near θ = 0°

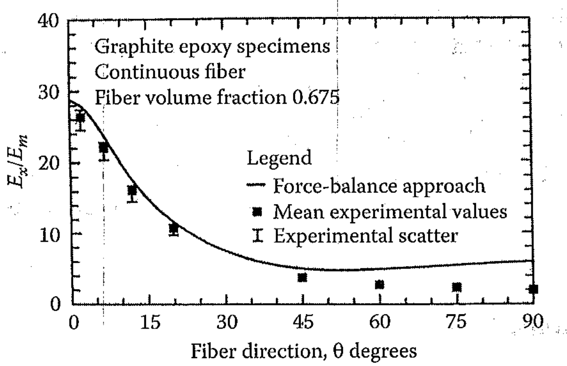

FIGURE 6.21
Comparison of predicted and measured off-axis modulus ratio, E_x/E_m, for graphite/epoxy. (From Suarez, S.A., Gibson, R.F., Sun, C.T., and Chaturvedi, S.K. 1986. *Experimental Mechanics*, 26(2), 175–184. With permission.)

As shown in the previous section, the fiber length required to attain the maximum composite stiffness at $\theta = 0°$ is quite small. Thus, the relatively low stiffness of practical short fiber composites is more likely to be caused by the off-axis orientation of the fibers than by the short length of the fibers.

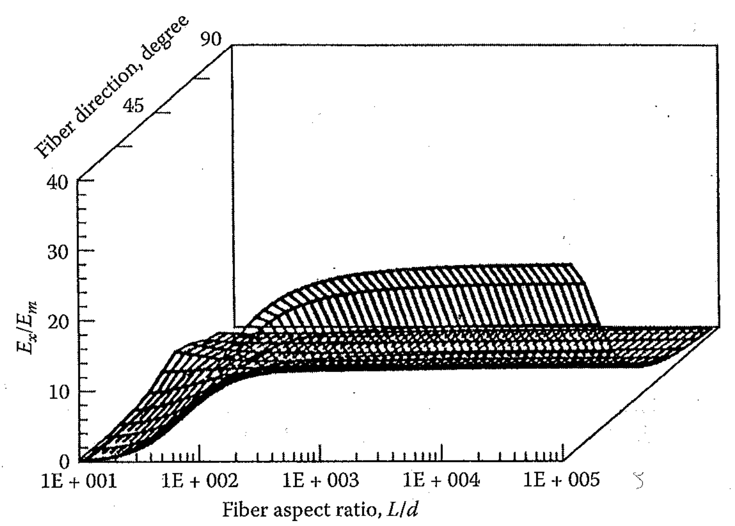

FIGURE 6.22
Tridimensional plot of E_x/E_m as a function of fiber aspect ratio and fiber orientation for graphite/epoxy. (From Suarez, S.A., Gibson, R.F., Sun, C.T., and Chaturvedi, S.K. 1986. *Experimental Mechanics*, 26(2), 175–184. With permission.)

Another important factor that should not be overlooked is the fiber volume fraction. In most short fiber composites, the maximum fiber volume fraction is quite low due to processing limitations. That is, the viscosity of the fiber/resin mixture must be kept below a certain limit for proper flow during the molding process. All these conclusions have important implications for the behavior of randomly oriented short fiber composites, which are discussed in the next section.

6.4 Randomly Oriented Discontinuous Fibers

If the fiber orientation in a composite is truly random in a 3-D sense, the composite exhibits 3-D isotropy. Such a situation is likely to exist when the fiber length, L, is much less than the thickness of the part, t, as shown in figure 6.23(a). Composites with low aspect ratio reinforcement such as whiskers, microfibers, and nanotubes generally fall into this category. However, in many short fiber composite parts (e.g., panels made from sheet-molding compounds or resin transfer moldings), the fiber length is much greater than the thickness of the part, as shown in figure 6.23(b). In this case, fiber orientation in the thickness direction is not possible, and the material exhibits 2-D isotropy or planar isotropy. The analysis of both types of materials will be discussed here, but the emphasis will be on the 2-D case.

6.4.1 Stress and Strength Analysis

The use of geometric averaging techniques for analyzing randomly oriented fiber composites has been introduced in example 2.5, and models for predicting strength and modulus of such composites are typically based

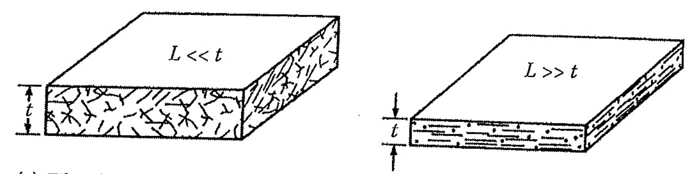

(a) Fiber length is less than thickness of part, so fibers are randomly oriented in three dimensions.

(b) Fiber length is greater than thickness of part, so fibers are randomly oriented in only two dimensions.

FIGURE 6.23
3-D and 2-D random orientations of fibers.

on averaging. For example, Baxter [20] developed a model for predicting the strength of randomly oriented fiber–reinforced metal matrix composites by averaging the Tsai–Hill equation for off-axis strength (eq. [6.31]) as

$$\bar{\sigma}_x = \frac{\int_0^{\pi} \sigma_x \, d\theta}{\pi} \tag{6.33}$$

Numerical integration was employed, since the integral could not be evaluated in closed form. The model was used to establish upper and lower limits of composite strength. The composite longitudinal strength was estimated from equation (6.14) or equation (6.15), and the other strengths in equation (6.31) were estimated according to the most likely failure modes.

Lees [21] assumed that the angular dependence of the failure stress, σ_x, for such a material under uniaxial off-axis loading could be described by using the Maximum Stress Criterion. Lees also assumed that there are three failure mechanisms according to the Maximum Stress Criterion, each operating over a range of angles as follows [recall eqs. (4.3) for uniaxial off-axis loading]:

$$\text{for } 0 \le \theta \le \theta_1, \quad \sigma_x = \frac{s_L^{(+)}}{\cos^2\theta} \quad \text{(longitudinal tensile failure)}$$

$$\text{for } \theta_1 \le \theta \le \theta_2, \quad \sigma_x = \frac{s_{LT}}{\sin\theta\cos\theta} \quad \text{(interfacial shear failure)}$$

$$\text{for } \theta_2 \le \theta \le \pi/2, \quad \sigma_x = \frac{s_T^{(+)}}{\sin^2\theta} \quad \text{(transverse tensile failure)}$$

where

$$\cot\theta_1 = \frac{s_L^{(+)}}{s_{LT}} \quad \text{and} \quad \tan\theta_2 = \frac{s_T^{(+)}}{s_{LT}}$$

For the case of the randomly oriented fiber composite, Lees assumed that the average strength over all angles is given by

$$\tilde{\sigma}_x = \frac{2}{\pi}\left\{\int_0^{\theta_1} \frac{s_L^{(+)}}{\cos^2\theta} d\theta + \int_{\theta_1}^{\theta_2} \frac{s_{LT}}{\sin\theta\cos\theta} d\theta + \int_{\theta_2}^{\pi/2} \frac{s_T^{(+)}}{\sin^2\theta} d\theta\right\} \tag{6.34}$$

After integrating and using equation (4.21) for $s_L^{(+)}$ for continuous fibers, and then making some simplifying approximations, Lees found that

$$\tilde{\sigma}_x \simeq \frac{2s_{LT}}{\pi}\left[1 + \frac{s_T^{(+)}}{s_{mfl}} + \ln\frac{s_T^{(+)} s_{mfl}}{s_{LT}^2}\right] \tag{6.35}$$

where s_{mfl} is the matrix stress corresponding to the fiber failure strain. The same approach was later taken by Chen [22], who included a strength efficiency factor, ψ, to account for discontinuous fibers and obtained the equation,

$$\tilde{\sigma}_x = \frac{2s_{LT}}{\pi}\left[2 + \ln\frac{\psi s_L^{(+)} s_T^{(+)}}{s_{LT}^2}\right] \tag{6.36}$$

Lees and Chen both reported reasonable agreement of their predictions with experimental data.

Another approach suggested by Halpin and Kardos [23] is based on the assumption that the strength of a randomly oriented fiber composite is the same as the strength of a quasi-isotropic laminate of the same material. Quasi-isotropic laminates, which are laminates of certain stacking sequences that behave in a planar isotropic manner, will be discussed in chapter 7 on laminates. Halpin and Kardos reported that the quasi-isotropic laminate model with the Maximum Strain Criterion for lamina failure gave good agreement with experimental data for a glass/epoxy composite [23].

6.4.2 Modulus Analysis

One major conclusion from section 6.3.2 was that fiber orientation is more important than fiber length in the determination of off-axis elastic constants of unidirectional composites. Further support for this conclusion is provided by the observation that continuous fiber models give reasonably accurate predictions of elastic properties of randomly oriented fiber–reinforced composites. The concept of averaging the elastic constants over all possible orientations by integration was apparently introduced by Cox [2], who modeled paper as a planar mat of continuous fibers without matrix material. The Cox formulas for the averaged isotropic elastic constants of random arrays of fibers are given here for later reference, but they are not considered to be accurate enough for design use. For the 2-D case,

$$\tilde{E} = \frac{E_f v_f}{3}, \quad \tilde{G} = \frac{E_f v_f}{8}, \quad \tilde{\nu} = \frac{1}{3} \tag{6.37}$$

and for the 3-D case,

$$\tilde{E} = \frac{E_f \upsilon_f}{6}, \quad \tilde{G} = \frac{E_f \upsilon_f}{15}, \quad \tilde{\nu} = \frac{1}{4} \tag{6.38}$$

where
$\tilde{E}$ = averaged Young's modulus for randomly oriented fiber composite
$\tilde{G}$ = averaged shear modulus for randomly oriented fiber composite
$\tilde{\nu}$ = averaged Poisson's ratio for randomly oriented fiber composite

Nielsen and Chen [24] used the averaging concept, along with micromechanics equations and transformation equations for a unidirectional continuous fiber–reinforced lamina, to analyze a planar isotropic composite. The geometrically averaged Young's modulus, which is assumed to be the same as the in-plane Young's modulus of the isotropic composite, is given by

$$\tilde{E} = \frac{\int_0^{\pi} E_x d\theta}{\int_0^{\pi} d\theta} \tag{6.39}$$

where the off-axis Young's modulus, E_x, is defined by the first of eqs. (2.39), and the angle is defined in figure 2.6. Nielsen and Chen used a set of micromechanics equations for a unidirectional continuous fiber composite to calculate E_1, E_2, G_{12}, and υ_{12}. Figure 6.24 shows that the averaged

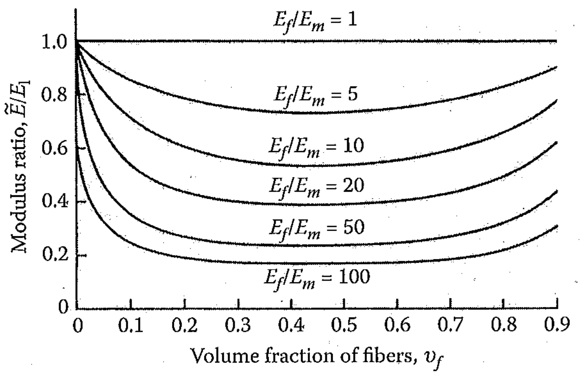

FIGURE 6.24
Dependence of modulus ratio, $\tilde{E}/E_1$, on fiber volume fraction for several values of E_f/E_m from Nielsen–Chen model. (From Nielsen, L.E. and Chen, P.E. 1968. *Journal of Materials*, 3(2), 352–358. Copyright, ASTM. Reprinted with permission.)

modulus for the randomly oriented fiber composite is much lower than the corresponding longitudinal modulus, E_1, for most practical composites. Since the analysis is based on a continuous fiber model, the predicted reduction in modulus is due to fiber orientation, and not to fiber length. The equation that Nielsen and Chen used for E_2 was known to give values lower than measured values, so the predictions of equation (6.39) were also lower than the corresponding experimental values.

The evaluation of equation (6.39) requires the integration of the expression for E_x given by equation (2.39), which is quite cumbersome. The integration is much simpler if the invariant forms of the transformed lamina stiffnesses are used. For example, the averaged value of the transformed lamina stiffness $\bar{Q}_{11}$ is given by

$$\tilde{Q}_{11} = \frac{\int_0^{\pi} \bar{Q}_{11} d\theta}{\int_0^{\pi} d\theta} = \frac{\int_0^{\pi} [U_1 + U_2 \cos\theta + U_3 \cos 4\theta] d\theta}{\pi} = U_1 \tag{6.40}$$

Similarly,

$$\tilde{Q}_{22} = U_1, \quad \tilde{Q}_{12} = \tilde{Q}_{21} = U_4, \quad \tilde{Q}_{66} = (U_1 - U_4)/2, \quad \tilde{Q}_{16} = \tilde{Q}_{26} = 0$$

and the stress–strain relations for any set of axes x,y in the plane are

$$\begin{Bmatrix} \sigma_x \\ \sigma_y \\ \tau_{xy} \end{Bmatrix} = \begin{bmatrix} U_1 & U_4 & 0 \\ U_4 & U_1 & 0 \\ 0 & 0 & (U_1 - U_4)/2 \end{bmatrix} \begin{Bmatrix} \varepsilon_x \\ \varepsilon_y \\ \gamma_{xy} \end{Bmatrix} \tag{6.41}$$

Since this is an isotropic material, we can write

$$\begin{aligned} \bar{Q}_{11} &= U_1 = \frac{\tilde{E}}{1-\tilde{\nu}^2} = \bar{Q}_{22} \\ \tilde{Q}_{12} &= U_4 = \frac{\tilde{\nu}\tilde{E}}{1-\tilde{\nu}^2} \\ \tilde{Q}_{66} &= \tilde{G} = \frac{\tilde{E}}{2(1+\tilde{\nu})} = \frac{U_1 - U_4}{2} \end{aligned} \tag{6.42}$$

Tsai and Pagano [25] and Halpin and Pagano [26] have obtained the same results by using invariant concepts along with quasi-isotropic laminate theory, which will be discussed later. Solving these equations for the isotropic engineering constants, we get

$$\tilde{E} = \frac{(U_1 - U_4)(U_1 + U_4)}{U_1}$$
$$\tilde{G} = \frac{U_1 - U_4}{2} \tag{6.43}$$
$$\tilde{\nu} = \frac{U_4}{U_1}$$

Using the equations relating the invariants in eqs. (6.43) to the engineering constants E_1, E_2, G_{12}, and ν_{12} for the orthotropic lamina (recall eqs. [2.44] and [2.27]), Tsai and Pagano [25] also developed the following approximate expressions:

$$\tilde{E} = \frac{3}{8}E_1 + \frac{5}{8}E_2, \quad \tilde{G} = \frac{1}{8}E_1 + \frac{1}{4}E_2 \tag{6.44}$$

These equations, along with the Halpin–Tsai equations for E_1 and E_2, were used to estimate the elastic moduli of randomly oriented boron fiber–reinforced epoxy, and the results compare favorably with experimental results (fig. 6.25). Manera [27] also got good agreement with experimental results by using equations (6.43) with a different set of micromechanics equations for E_1, E_2, G_{12}, and ν_{12}.

Christensen and Waals [28] also used the averaging approach to find the isotropic elastic constants for continuous fiber composites with 2-D and 3-D random fiber orientation. This appears to be the first published report of the analysis of a composite with 3-D oriented fibers, although Cox [2] derived equations (6.38) for the case of fibers without matrix material. Only the 3-D analysis of Christensen and Waals is summarized here, since the 2-D analysis is quite similar to those that have already been discussed.

For the 3-D Christensen–Waals analysis, the spherical coordinate system shown in figure 6.26 is used. An orthotropic, transversely isotropic composite with fibers oriented along the 1 direction is subjected to an arbitrary normal strain such as ε'_{33} along the 3′ direction. For the purpose of the analysis, the 3 axis is taken to be in the 1′2′ plane. The basic premise of the solution is that the resulting ratio of stress to strain $\sigma'_{ij} / \varepsilon'_{33}$ $(i, j = 1, 2, 3)$ for a random orientation of fibers can be found by calculating the average value of $\sigma'_{ij} / \varepsilon'_{33}$ over all possible orientations of the fiber direction (1 axis) relative to the fixed x'_i axes. Using the 3-D stress–strain relationships for a generally orthotropic, transversely isotropic material [i.e., the stiffness

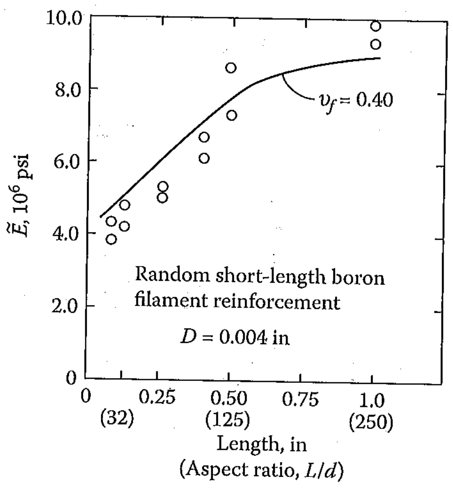

FIGURE 6.25
Dependence of Young's modulus of randomly oriented short fiber boron/epoxy composite on fiber aspect ratio. Comparison of predictions from Halpin–Tsai equations and invariant expressions with experimental data. (From Halpin, J.C. and Pagano, N.J. 1969. *Journal of Composite Materials*, 3, 720–724. Reprinted by permission of Technomic Publishing Co.)

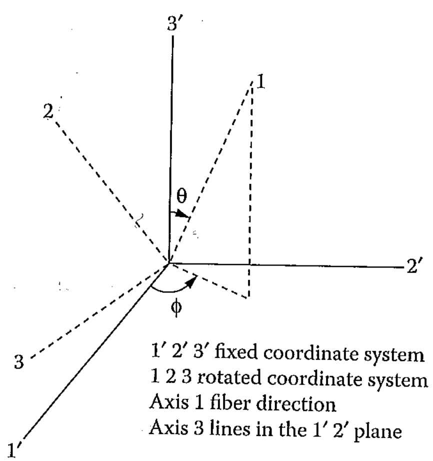

FIGURE 6.26
Spherical coordinates for 3-D Christensen–Waals analysis. (From Christensen, R.M. and Waals, F.M. 1972. *Journal of Composite Materials*, 6, 518–532. Reprinted by permission of Technomic Publishing Co.)

matrix of equation (2.17) transformed to an arbitrary 1′2′3′ off-axis coordinate system], it can be shown that

$$\frac{\sigma'_{33}}{\varepsilon'_{33}} = C_{11}\lambda_{31}^4 + (2C_{12} + 4C_{66})\lambda_{31}^2\lambda_{32}^2 + C_{22}\lambda_{32}^4 \tag{6.45}$$

and that

$$\begin{aligned}\frac{\sigma'_{22}}{\varepsilon'_{33}} &= C_{11}\lambda_{31}^2\lambda_{21}^2 + C_{12}\left(\lambda_{32}^2\lambda_{21}^2 + \lambda_{31}^2\lambda_{22}^2 + \lambda_{31}^2\lambda_{23}^2\right) \\ &\quad + C_{22}\lambda_{32}^2\lambda_{22}^2 + 4C_{66}\lambda_{31}\lambda_{32}\lambda_{21}\lambda_{22} + C_{23}\lambda_{32}^2\lambda_{23}^2\end{aligned} \tag{6.46}$$

where the direction cosines λ_{ij} are given by

$$\lambda_{ij} = \begin{bmatrix} \sin\theta\cos\phi & -\cos\theta\cos\phi & \sin\phi \\ \sin\theta\sin\phi & -\cos\theta\sin\phi & -\cos\phi \\ \cos\theta & \sin\theta & 0 \end{bmatrix} \tag{6.47}$$

Averaging over all possible orientations of the fiber direction, we have

$$\left.\frac{\sigma'_{ij}}{\varepsilon'_{33}}\right|_{\text{Random}} = \frac{\int_0^\pi\int_0^\pi (\sigma'_{ij}/\varepsilon'_{33})\sin\theta\, d\theta\, d\phi}{\int_0^\pi\int_0^\pi \sin\theta\, d\theta\, d\phi} \tag{6.48}$$

After substituting equation (6.45) in equation (6.48), we get

$$\left.\frac{\sigma'_{33}}{\varepsilon'_{33}}\right|_{\text{Random}} = \frac{1}{15}(3C_{11} + 4C_{12} + 8C_{22} + 8C_{23}) \tag{6.49}$$

For an equivalent homogeneous isotropic material, the corresponding ratio of stress to strain is

$$\frac{\sigma'_{33}}{\varepsilon'_{33}} = \frac{\tilde{E}(1-\tilde{\nu})}{(1+\tilde{\nu})(1-2\tilde{\nu})} \tag{6.50}$$

Similarly, after substituting equation (6.46) in equation (6.48), we get

$$\left.\frac{\sigma'_{22}}{\varepsilon'_{33}}\right|_{\text{Random}} = \frac{1}{15}(C_{11} + 8C_{12} + C_{22} - 4C_{66} + 5C_{23}) \tag{6.51}$$

and the corresponding ratio of stress to strain for an equivalent homogeneous isotropic material is

$$\frac{\sigma'_{22}}{\varepsilon'_{33}} = \frac{\tilde{\nu}\tilde{E}}{(1+\tilde{\nu})(1-2\tilde{\nu})} \tag{6.52}$$

Equating the ratio in equation (6.49) to that in equation (6.50), then equating the ratio in equation (6.51) to that in equation (6.52), and solving the two resulting equations simultaneously for the effective isotropic engineering constants, Christensen and Waals found that

$$\tilde{E} = \frac{\left[E_1 + \left(4\nu_{12}^2 + 8\nu_{12} + 4\right)K_{23}\right]\left[E_1 + \left(4\nu_{12}^2 - 4\nu_{12} + 1\right)K_{23} + 6(G_{12} + G_{23})\right]}{3\left[2E_1 + \left(8\nu_{12}^2 + 12\nu_{12} + 7\right)K_{23} + 2(G_{12} + G_{23})\right]} \tag{6.53}$$

and

$$\tilde{\nu} = \frac{E_1 + \left(4\nu_{12}^2 + 16\nu_{12} + 6\right)K_{23} - 4(G_{12} + G_{23})}{4E_1 + \left(16\nu_{12}^2 + 24\nu_{12} + 14\right)K_{23} + 4(G_{12} + G_{23})} \tag{6.54}$$

where K_{23} is the plane strain bulk modulus for dilatation in the 2–3 plane with $\varepsilon_{11} = 0$, and the other properties are defined in chapter 2. Christensen and Waals used the previously developed micromechanics equations by Hashin [29,30] and Hill [31] to calculate the five independent engineering constants E_1, ν_{12}, G_{12}, G_{23}, and K_{23}, which appear in equation (6.53) and equation (6.54). Predictions from equation (6.53) for a glass/epoxy composite are shown in figure 6.27, along with the rule of mixtures prediction from equation (3.23) and the Cox prediction from equation (6.38). The prediction from the Cox model is well below that of the Christensen–Waals model, and the rule of mixtures prediction is much too high.

Using the same averaging technique, Christensen and Waals also developed a set of equations analogous to equation (6.53) and equation (6.54) for the 2-D case. The results are [23]:

$$\tilde{E} = \frac{1}{u_1}\left(u_1^2 - u_2^2\right) \tag{6.55}$$

and

$$\tilde{\nu} = \frac{u_2}{u_1} \tag{6.56}$$

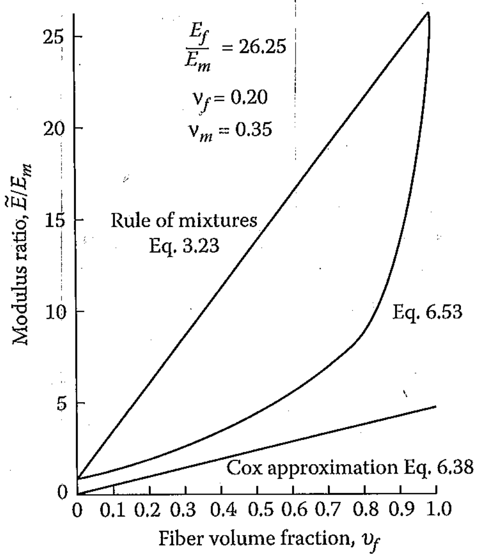

FIGURE 6.27
Comparison of Christensen–Waals 3-D analysis for Young's modulus of randomly oriented fiber composite with rule of mixtures and Cox approximation for a glass/epoxy composite. (From Christensen, R.M. and Waals, F.M. 1972. *Journal of Composite Materials*, 6, 518–532. Reprinted by permission of Technomic Publishing Co.)

where

$$u_1 = \frac{3}{8}E_1 + \frac{G_{12}}{2} + \frac{\left(3 + 2\nu_{12} + 3\nu_{12}^2\right)G_{23}K_{23}}{2(G_{23} + K_{23})}$$
$$u_2 = \frac{1}{8}E_1 - \frac{G_{12}}{2} + \frac{\left(1 + 6\nu_{12} + \nu_{12}^2\right)G_{23}K_{23}}{2(G_{23} + K_{23})} \tag{6.57}$$

The results from equation (6.55) to equation (6.57) for a glass/polystyrene composite are shown in figure 6.28. The Christensen–Waals model is seen to give much better agreement with the measurements than either the Cox model or the rule of mixtures, although none of the models takes into account the fiber length. Chang and Weng [32] also obtained good agreement with experimental results for glass/polyester sheet-molding compounds by using equation (6.55) to equation (6.57). Christensen later presented simplified versions of these equations based on an asymptotic expansion [33,34].

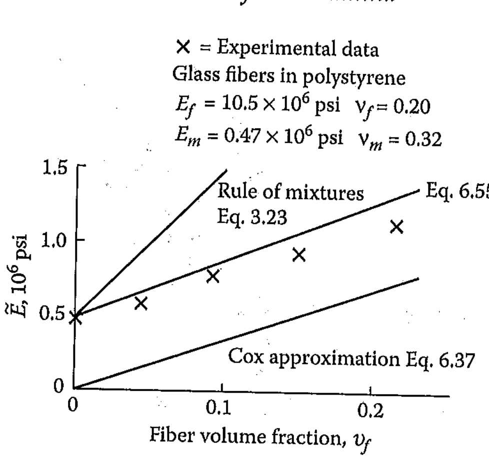

FIGURE 6.28
Comparison of Christensen–Waals 2-D analysis for Young's modulus of randomly oriented fiber composite with rule of mixtures and Cox approximation for a glass/polystyrene composite. (From Christensen, R.M. and Waals, F.M. 1972. *Journal of Composite Materials*, 6, 518–532. Reprinted by permission of Technomic Publishing Co.)

Weng and Sun [35] used the Christensen–Waals equations along with micromechanics equations, which were modified to account for the effect of fiber length. The effect of fiber length was modeled by using a so-called "fictitious fiber," which included the effect of matrix material at the ends of the fiber in the RVE shown in figure 6.2(a). The effects of varying stresses along the fiber were not accounted for, however, as it was assumed that the stresses were equal in the fiber and matrix portions of the fictitious fiber. The equation for the effective modulus of the fictitious fiber is analogous to equation (6.28) for the modified Cox model, except that the stress distribution along the fiber is assumed to be uniform. Figure 6.29 shows a comparison of the predictions of the modified Christensen–Waals theory with the original Christensen–Waals theory, the rule of mixtures, the Halpin–Tsai equations, and experimental data. For the glass/polyester sheet-molding compound material used, the effect of fiber length is apparently not very great, as the predictions of modified and original Christensen–Waals theories are almost the same. Both theories give predictions that are in good agreement with the experimental data.

The effects of fiber length and nonuniform stress distribution along the discontinuous fiber were accounted for by Sun et al. [36], who developed equations for the elastic moduli of 2-D randomly oriented, short fiber composites as part of a study of vibration damping properties. A modified Cox model was used to determine E_1, while the other lamina properties

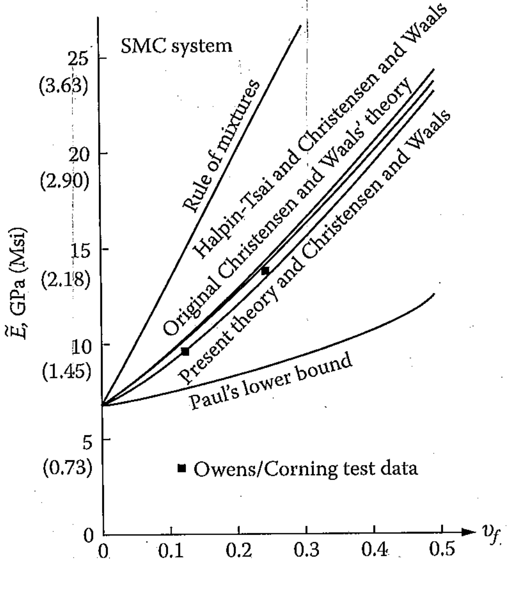

FIGURE 6.29
Comparison of various theories for prediction of Young's modulus of randomly oriented chopped glass/polyester sheet molding compound. (From Weng, G.J. and Sun, C.T. 1979. In Tsai, S.W. ed., *Composite Materials: Testing and Design (Fifth Conference)*, ASTM STP 674, pp. 149–162. American Society for Testing and Materials, Philadelphia, PA. Copyright ASTM. Reprinted with permission.)

were assumed to be independent of fiber length. The modified Cox model in this case is of the form

$$E_{MC1} = E_{f1}\left[\frac{1-\tanh(\beta L/2)}{\beta L/2}\right]\upsilon_f\alpha + E_m\upsilon_m\gamma \tag{6.58}$$

where α and γ are strain magnification factors, which are determined from a finite element analysis. The modified Cox model for E_1, along with the rule of mixtures (eq. [3.41]) for υ_{12} and the Halpin–Tsai equations (eq. [3.59]) and eq. [3.60]) for E_2 and G_{12}, are used in transformation equations of the form described in equations (6.32), which are then used in equations (6.43) to determine the averaged isotropic engineering constants for the randomly oriented fiber composite. A tridimensional plot of the Young's modulus versus the fiber aspect ratio, L/d, and the ratio E_f/E_m is shown in figure 6.30. It is seen that high E_f/E_m and high L/d are required in order to have a high composite modulus. As with the aligned discontinuous case, the fiber aspect ratio required to attain maximum stiffness for given fiber and matrix materials is quite low.

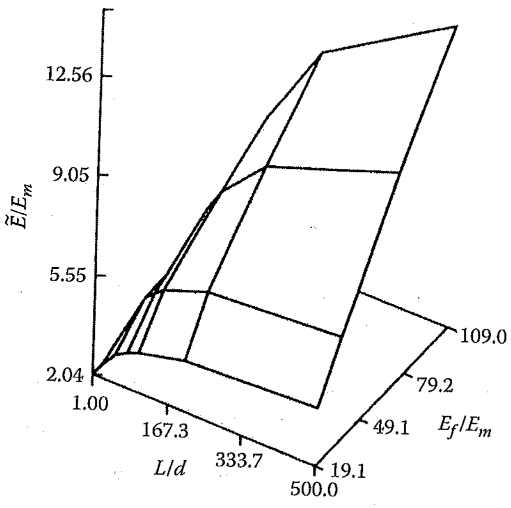

FIGURE 6.30
Tridimensional plot of $\tilde{E}/E_m$ as a function of L/d and E_f/E_m for a randomly oriented short fiber composite. (From Sun, C.T., Wu, J.K., and Gibson, R.F. 1985. *Journal of Reinforced Plastics and Composites*, 4, 262–272. Reprinted by permission of Technomic Publishing Co.)

EXAMPLE 6.3

A carbon/epoxy composite with randomly oriented short fibers is made of the same constituent materials with the same fiber volume fraction as the material described in examples 3.1, example 3.4, and example 4.5. Assuming that the in-plane shear strength s_{LT} = 60 MPa, and that the fiber length is much greater than the thickness of the material, estimate the Young's modulus, shear modulus, Poisson's ratio, and tensile strength of this composite.

Solution. From equations (6.44), the Young's modulus is approximately

$$\tilde{E} = \frac{3}{8}E_1 + \frac{5}{8}E_2 = \frac{3}{8}(113) + \frac{5}{8}(5.65) = 45.9 \text{ GPa}$$

and the shear modulus is approximately

$$\tilde{G} = \frac{1}{8}E_1 + \frac{1}{4}E_2 = \frac{1}{8}(113) + \frac{1}{4}(5.65) = 15.54 \text{ GPa}$$

which means that the Poisson's ratio is

$$\tilde{\nu} = \frac{\tilde{E}}{2\tilde{G}} - 1 = \frac{45.9}{2(15.54)} - 1 = 0.47$$

From equation (6.35), the tensile strength is approximately

$$\tilde{\sigma}_x = \frac{2s_{LT}}{\pi}\left[1 + \frac{s_T^{(+)}}{s_{mfl}} + \ln\frac{s_T^{(+)}s_{mfl}}{s_{LT}^2}\right] = \frac{2(60)}{\pi}\left[1 + \frac{66.9}{37.95} + \ln\frac{66.9(37.95)}{(60)^2}\right] = 92.2 \text{ MPa}$$

Notice that the isotropic Young's modulus for the randomly oriented composite is much greater than the transverse modulus but less than half the longitudinal modulus of the corresponding orthotropic lamina. Likewise, the isotropic strength is greater than the orthotropic transverse strength but well below the orthotropic longitudinal strength. It is also important to remember that these predictions are based on randomly oriented continuous fibers, so that the differences between the isotropic properties and the orthotropic properties are due to fiber orientation, and not to fiber length.

EXAMPLE 6.4

Determine the Young's modulus of a randomly oriented fiber composite if the unidirectional form of the composite has an off-axis Young's modulus that can be described by an equation of the form

$$E_x(\theta) = E_2 + (E_1 - E_2)[1 - (2\theta/\pi)^{1/3}]$$

where θ is the fiber angle in radians and E_1 and E_2 are the longitudinal and transverse Young's moduli, respectively, of the unidirectional composite.

Solution. The Young's modulus of the randomly oriented fiber composite, averaged over all angles, is

$$\tilde{E} = \frac{2}{\pi}\int_0^{\pi/2} E_x(\theta)d\theta = \frac{2}{\pi}\int_0^{\pi/2}\left\{E_2 + (E_1 - E_2)[1 - (2\theta/\pi)^{1/3}]\right\}d\theta = 0.25E_1 + 0.75E_2$$

If, say, $E_2 = 0.1E_1$ for carbon/epoxy composite, then

$$\tilde{E} = 0.25E_1 + 0.75(0.1E_1) = 0.325E_1 \quad \text{or} \quad 3.25E_2$$

These results again reflect the magnitude of the reduction in stiffness that can be expected because of fiber orientation effects alone, since the fiber length has not been considered in this analysis.

6.5 Nanofibers and Nanotubes

The development of nanofibers and nanotubes has played a major role in the recent nanotechnology revolution, and the use of these materials as reinforcements in composites has received particular attention. With dimensions in the nanometer range, nanofibers have solid cylindrical shapes and nanotubes have hollow tubular geometries. Although aspect ratios L/d may range up into the thousands, they are both generally considered to be discontinuous in nature, so it is particularly appropriate to discuss them in this chapter. There has been intense interest in carbon nanotubes (CNTs) since they were discovered in 1991 by Iijima [37], and the number of publications on CNTs and CNT-reinforced composite materials has grown very quickly since that time. Several review articles on the mechanical behavior of CNTs have appeared [38,39], and a special issue of a leading composites journal was dedicated to modeling and characterization of nanostructured materials [40]. CNTs are available in single wall (SWNT) or multiwalled (MWNT) configurations, and the geometrical arrangement of carbon atoms in the nanotubes can be described as being either zig-zag or armchair [38,39].

Microscopic images of carbon nanofibers and nanotubes in various polymer matrices are shown in figure 6.31 from ref. [41] and figure 6.32

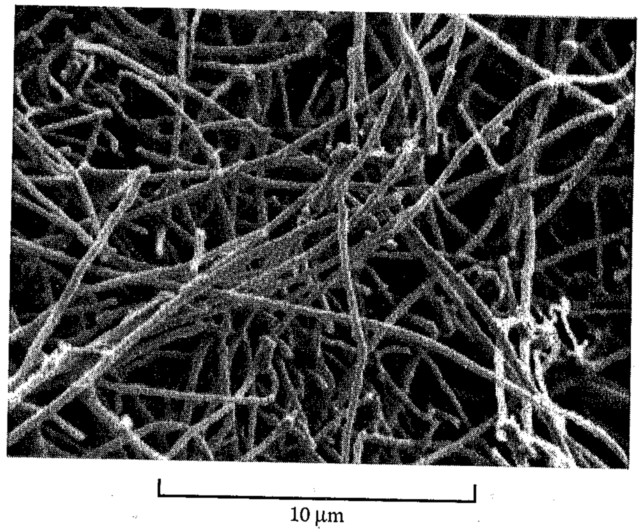

FIGURE 6.31
Scanning electron microscope image of vapor-grown carbon nanofibers in a polypropylene matrix. (From Tibbetts, G.G. and McHugh, J.J. 1999. *Journal of Materials Research*, 14(7), 2871–2880. With permission.)

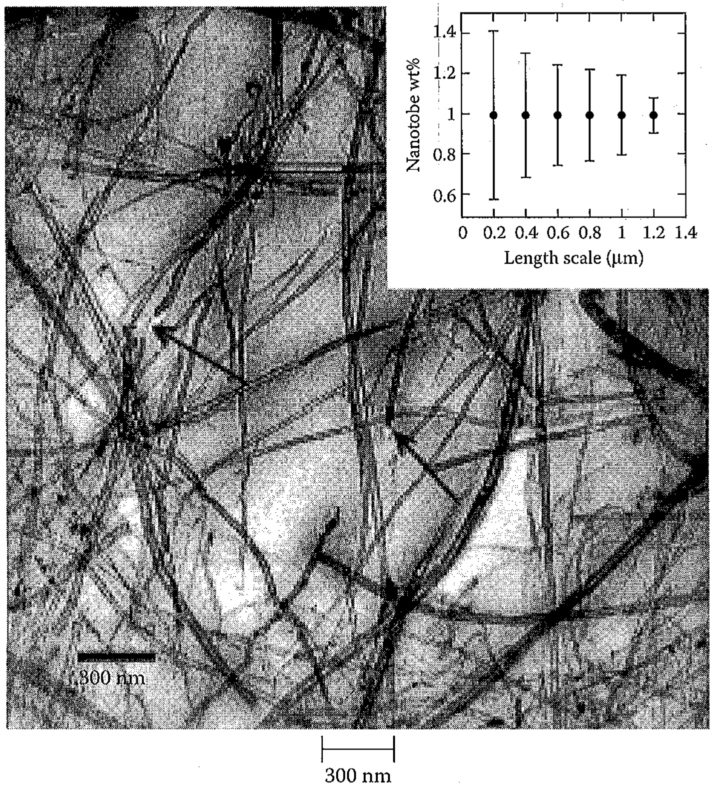

FIGURE 6.32
Transmission electron microscope image of MWNTs in a polystyrene matrix. (From Qian, D., Dickey, E.C., Andrews, R., and Rantell, T. 2000. *Applied Physics Letters*, 76 (20), 2868–2870. With permission.)

from ref. [42], respectively, while typical geometrical and mechanical properties of nanofibers and nanotubes are listed in table 6.1, which is partially taken from ref. [43].

From figure 6.31 and figure 6.32 and table 6.1, it is clear that two key geometrical features must be accounted for in the development of micromechanical models for nanocomposites reinforced with nanofibers and/or nanotubes. Due to their microscopic dimensions by comparison with typical thicknesses of composite structures, nanofibers or nanotubes will almost certainly have random orientations in all three dimensions within the composite as in figure 6.23(a), so the resulting nanocomposite will be macroscopically isotropic. Nanofibers and nanotubes exhibit significant waviness, but all of the previously discussed micromechanics models as

TABLE 6.1
Geometrical and Mechanical Properties of Typical Carbon Nanofibers and Nanotubes

Material	Diameter (nm)	Length (nm)	Young's Modulus (GPa)	Tensile Strength (GPa)
Vapor-grown carbon nanofibers	100–200[a]	30,000–100,000[a]	400–600[a]	2.7–7.0[a]
SWNT	~ 1.3[b]	500–40,000[b]	320–1470[c]	13–52[c]

Source: [a]Nanofiber geometrical and mechanical properties from Applied Sciences, Inc., Cedarville, OH.
[b]Nanotube geometrical properties from Helix Material Solutions, Inc., Richardson, TX.
[c]Nanotube mechanical properties from Yu, M.-F., Files, B., Arepalli, S., and Ruoff, R.S. 2000. *Physical Review Letters*, 84(24), 5552–5555. With permission.

in figure 6.2, figure 6.14, and figure 6.16 have been based on the assumption of straight fiber reinforcement.

6.5.1 Strength Analysis

Models for predicting the strength of nanocomposites with randomly oriented nanofibers or nanotubes are not as well developed as those for predicting elastic modulus. Tibbetts and McHugh [41] presented experimental and analytical results for randomly oriented carbon nanofiber–reinforced polypropylene and nylon composites. Strength predictions were based on the averaging method of Baxter [20], which was described in section 6.4.1. Nanofibers were assumed to have lengths less than the critical length, so equation (6.14) was used to estimate the longitudinal composite strength as input to the Tsai–Hill equation (eq. [6.31]) before performing the averaging in equation (6.33), but the effect of nanofiber waviness was not considered. The authors concluded that the experimental results for as-grown nanofibers were generally disappointing due to inadequate infiltration of the fiber clumps by the matrix resin during the injection molding of the specimens, but ball milling of the nanofibers reduced the size of the clumps, resulting in significant improvement in the properties, as did etching of the surfaces of the nanofibers. Experimental strength data generally fell between the predictions of 1-D and 3-D models based on Baxter's approach, but since nanofiber waviness was not included in the models, it is difficult to draw conclusions from comparisons of predictions with measurements.

6.5.2 Modulus Analysis

Micromechanics models for the elastic moduli of nanocomposites, which include the effects of both 3-D random orientation and waviness of the

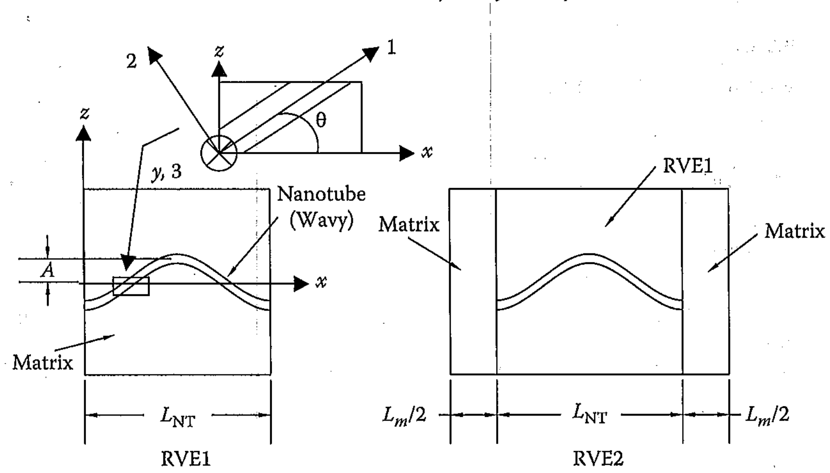

FIGURE 6.33
RVEs for Anumandla–Gibson model. (From Anumandla, V. and Gibson, R.F. 2006. *Composites Part A: Applied Science and Manufacturing* 37(12), 2178–2185. With permission.)

reinforcement, have been developed by Fisher et al. [44–46] and by Anumandla and Gibson [47,48]. The approach of Fisher et al. [44–46] is based on 3-D finite element models, whereas the model of Anumandla and Gibson [47,48] is an approximate closed form solution. Only the latter approach is summarized in the following.

The Anumandla–Gibson approach [47,48] consists of a combination of the waviness models of Chan and Wang [49] and Hsiao and Daniel [50] for locally orthotropic materials, the Chamis micromechanics equations (ref. [14] of chap. 3) for predicting the elastic constants of the locally orthotropic material, and the Christensen–Waals model [28], which accounts for the 3-D random orientation of the fibers (or in this case, nanotubes). The wavy fiber-reinforced composite is divided into segments along its length, each of which is locally orthotropic but with off-axis orientation. The strains are averaged over one wavelength along the loading direction for uniaxial loading, and the effective Young's modulus is determined from the ratio of applied stress to resulting average strains. The RVEs are shown in figure 6.33, where the waviness and orientation of the nanotube are accounted for in RVE1, and the overall length of RVE2 includes the matrix material between fibers.

The nanotube waviness is characterized by the waviness factor,

$$w = \frac{A}{L_{NT}} \tag{6.59}$$

where A is the amplitude of the waviness, L_{NT} is the nanotube length, and coordinates x and z, describing the waviness, are defined in figure 6.33 and equation (6.60):

$$z = A\sin\left(\frac{2\pi x}{L_{NT}}\right) \tag{6.60}$$

The effective Young's modulus, E_x, of RVE1, with uniform waviness of the embedded nanotube, is assumed to be the same as that of an element in a locally orthotropic lamina containing wavy fibers as described by Hsiao and Daniel [50]. Following this approach, the transformed compliances of an off-axis orthotropic lamina are averaged over one wavelength of fiber waviness, and the definition of an effective Young's modulus is used to find [50]

$$E_x = \frac{\sigma_x}{\bar{\varepsilon}_x} = \frac{1}{S_{11}I_1 + (2S_{12} + S_{66})I_3 + S_{22}I_5} = E_{RVE1} \tag{6.61}$$

where σ_x is the applied uniaxial stress, $\bar{\varepsilon}_x$ is the resulting average strain, S_{11}, S_{12}, S_{22}, and S_{66} are the locally orthotropic compliances referred to the principal material coordinates, and I_1, I_3, and I_5 are functions that depend only on the waviness factor. The locally orthotropic compliances are estimated from micromechanics using the Chamis equations (ref. [14] of chap. 3). The effective elastic modulus $\tilde{E}$ ($= E_{3D\text{-}RVE1}$) for the 3-D random orientation of the nanotubes is assumed to be the same as the modulus for a fiber-reinforced composite containing fibers that are randomly oriented in all three dimensions as given by Christensen and Waals [28]. For the purpose of the present discussion, the Christensen–Waals analysis described in section 6.4. is modified by replacing the (1,2,3), and (1′,2′,3′) coordinate systems in figure 6.26 by the (x,y,z) and (x',y',z') coordinate systems, respectively. Then according to the modified Christensen–Waals analysis, an orthotropic, transversely isotropic composite with nanotube waviness along the x direction is subjected to an arbitrary normal strain such as ε'_{zz} along the z' direction (the z axis is taken to be in the $x'y'$ plane for the purpose of the analysis). The resulting ratio of stress to strain, $\sigma'_{ij}/\varepsilon'_{zz}$ $(i, j = x, y, z)$, for random orientation of fibers is found by calculating the average value of $\sigma'_{ij}/\varepsilon'_{zz}$ over all possible orientations of the nanotube waviness direction (x axis) relative to the fixed x'_i axes. Equation (6.62) indicates the averaging over all possible orientations of the wavy nanotube:

$$\left.\frac{\sigma'_{ij}}{\varepsilon'_{zz}}\right|_{Random} = \frac{\int_0^{\pi}\int_0^{\pi}\frac{\sigma'_{ij}}{\varepsilon'_{zz}}\sin\theta\, d\theta\, d\phi}{\int_0^{\pi}\int_0^{\pi}\sin\theta\, d\theta\, d\phi} = \frac{1}{2\pi}\int_0^{\pi}\int_0^{\pi}\frac{\sigma'_{ij}}{\varepsilon'_{zz}}\sin\theta\, d\theta\, d\phi \tag{6.62}$$

where the angles θ and ϕ are defined in figure 6.26. The equations resulting from equation (6.62) upon substituting the 3-D stress–strain relationships for a generally orthotropic transversely isotropic material and solving simultaneously with the stress–strain relations for an equivalent homogenous isotropic material, yield the effective composite elastic modulus $\tilde{E}$ (= $E_{3D\text{-}RVE1}$) for the 3-D random orientation of the nanotube as:

$$\tilde{E} = \frac{\left[E_x + \left(4\nu_{xz}^2 + 8\nu_{xz} + 4\right)K_{zy}\right]\left[E_x + \left(4\nu_{xz}^2 - 4\nu_{xz} + 1\right)K_{zy} + 6(G_{xz} + G_{zy})\right]}{3\left[2E_x + \left(8\nu_{xz}^2 + 12\nu_{xz} + 7\right)K_{zy} + 2(G_{xz} + G_{zy})\right]}$$

$$= E_{3D\text{-}RVE1} \qquad (6.63)$$

where E_x (= E_{RVE1}) is the effective elastic modulus of RVE1 according to equation (6.61), K_{zy} is the plane bulk modulus for dilatation in the y–z plane with $\varepsilon_{xx} = 0$, and all other properties in equation (6.63) are for RVE1 in accordance with those defined in ref. [50]. Note that equation (6.63) is the same as equation (6.53), except for the substitution of coordinates described above. An expression for the effective elastic modulus of RVE2 with 3-D random orientation of nanotubes, $E_{3D\text{-}RVE2}$, is approximated by means of another inverse rule of mixtures for the series arrangement in RVE2 (fig. 6.33) as

$$\frac{1}{E_{3D\text{-}RVE2}} = \frac{1}{E_{3D\text{-}RVE1}}\left(\frac{L_{NT}}{L_m + L_{NT}}\right) + \frac{1}{E_m}\left(\frac{L_m}{L_m + L_{NT}}\right) \qquad (6.64)$$

where $E_{3D\text{-}RVE1}$ is the effective elastic modulus of RVE1 for 3-D random orientation of the nanotubes according to equation (6.63).

Figure 6.34 shows a comparison of the predictions of $E_{3D\text{-}RVE2}$ from equation (6.64) with experimental results on MWNT/polystyrene composites published by Andrews et al. [51]. In the predictions, the modulus of the polystyrene matrix was assumed to be 1.9 GPa, the local modulus of the nanotube was assumed to be 1 TPa, and the nanotube volume fraction in RVE2 was varied by assuming L_{NT}/L_m ratios of 0, 1, 2, 3, 4, and 5. It is seen that if waviness is neglected (i.e., $w = 0$), equation (6.64) significantly overpredicts the experimental data, but as waviness increases, the predicted modulus is reduced accordingly. For waviness factors lying within the range 0.075–0.25, the predictions are in best agreement with the published experimental results. These values of waviness seem quite reasonable in view of microscopic images such as the one in figure 6.32.

Nanofibers and nanotubes can be used not only as the principal reinforcement in composites, but as a third phase in composites consisting of conventional fiber reinforcement. Such a nanocomposite matrix material can

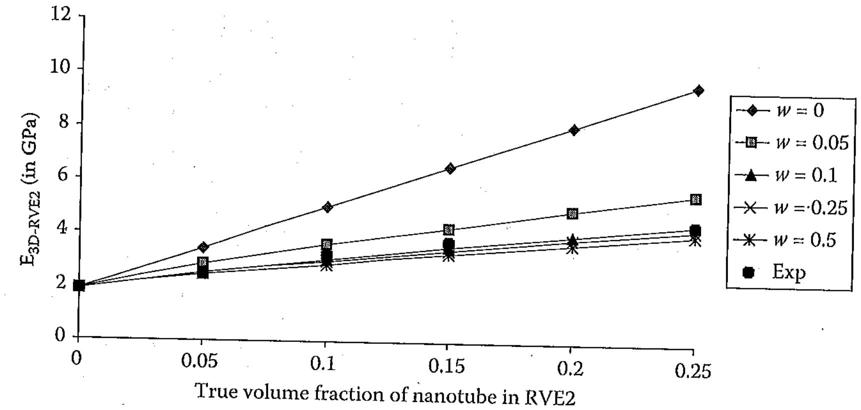

FIGURE 6.34
Comparison of experimental modulus data for MWNT/polystyrene composite from Andrews et al. 2002, Micromolecular Materials Engineering, 287(6), 395–403 with micromechanics predictions from equation (6.64). (From Anumandla, V. and Gibson, R.F. 2006. *Composites Part A: Applied Science and Manufacturing* 37(12), 2178–2185. With permission.)

improve the matrix-dominated properties of a conventional continuous fiber composite, such as compressive strength. A nanocomposite matrix material typically has a higher modulus than the plain polymer matrix, thus increasing the lateral support for the continuous fibers, increasing the buckling load, and improving the compressive strength of the conventional composite. For example, Vlasveld et al. [52] developed hybrid composites consisting of conventional glass or carbon fibers in a nanocomposite matrix (fig. 6.35),

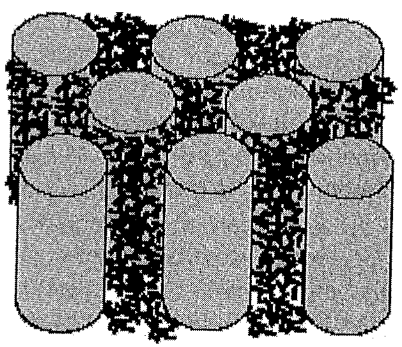

FIGURE 6.35
Nanoparticle reinforcement of the matrix in a conventional continuous fiber composite. (From Vlasveld, D.P.N., Bersee, H.E.N., and Picken, S.J. 2005. *Polymer*, 46, 10269–10278. With permission.)

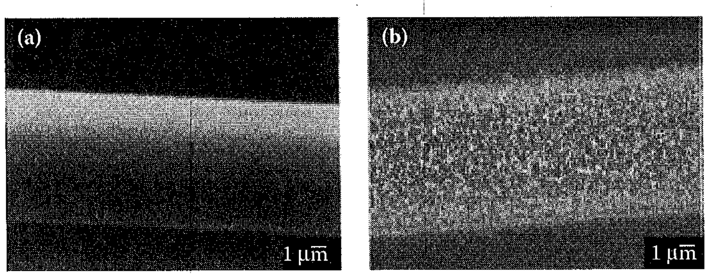

FIGURE 6.36
SEM micrographs of carbon fibers (a) before and (b) after CNT growth on the fiber surface. (From Thostenson, E.T., Li, W.Z., Wang, D.Z., Ren, Z.F., and Chou, T.W. 2002. *Journal of Applied Physics*, 91(9), 6034–6037. With permission.)

where the nanocomposite matrix was made of polyamide 6 (PA6) polymer reinforced with synthetic mica–layered silica nanoparticles. The nanocomposite matrix led to significant increases in flexural strength, which was dominated by fiber microbuckling on the compression side of the specimens. The effect was particularly significant at elevated temperatures. Thostenson et al. [53] developed a hybrid multiscale composite by growing CNTs directly on the surfaces of conventional carbon fibers, which were then combined with a conventional epoxy matrix. Figure 6.36 shows micrographs of the carbon fiber before and after nanotube growth.

6.6 Problems

1. A short fiber composite is to be modeled using the RVE in figure 6.2(b). Assuming that the matrix is rigid–plastic in shear but that both the fiber and matrix are elastic in extension, develop an equation for the longitudinal modulus of the RVE. What values of the longitudinal modulus does the model give as the fiber length becomes very large? very small?
2. Using the result from problem 6.1, develop an expression for the longitudinal modulus of the RVE shown in figure 6.2(a) that includes the effect of the matrix material at the fiber ends.
3. A carbon/epoxy single fiber test specimen is subjected to a uniaxial tensile stress that is increased until the fiber breaks up into pieces having a length of 0.625 mm. If the fiber has a diameter of 0.01 mm, a longitudinal modulus of 240 GPa, and an ultimate tensile strength of 2.5 GPa, what is the interfacial shear strength of the specimen? If the composite longitudinal modulus is 80 GPa,

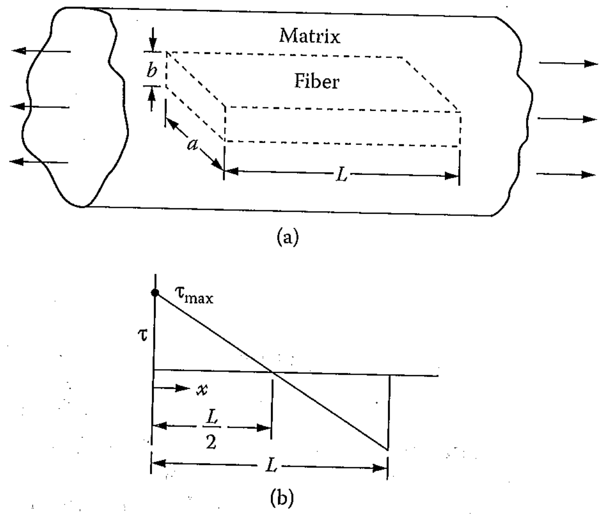

FIGURE 6.37
(a) Fiber with rectangular cross-section embedded in matrix. (b) Interfacial shear stress distribution along the fiber shown in (a).

what applied composite stress is required to produce the condition above?

4. A linear elastic fiber of rectangular cross-section is embedded in a linear elastic matrix material, and the composite is subjected to a uniaxial stress as shown in figure 6.37(a). The interfacial shear stress distribution along the fiber is to be approximated by a linear function, as shown in figure 6.37(b). Determine the fiber length, L, that is required to develop the ultimate tensile stress, $s_{f1}^{(+)}$, at the midpoint of the fiber. Neglect the stress transmitted across the ends of the fiber.
5. A short fiber composite is made from boron fibers of length 0.125 in (3.175 mm) and diameter 0.0056 in (0.142 mm) randomly oriented in a high-modulus (HM) epoxy matrix with a fiber volume fraction of 0.4. Using the fiber and matrix properties in table 3.1 and table 3.2, respectively, estimate the modulus of elasticity for the composite. Compare the modulus for the randomly oriented short fiber composite with the longitudinal and transverse moduli of an orthotropically aligned discontinuous fiber lamina of the same material.
6. Express the isotropic moduli $\tilde{E}$ and $\tilde{G}$ of a randomly oriented fiber composite in equations (6.43) in terms of the orthotropic lamina stiffnesses Q_{ij}.

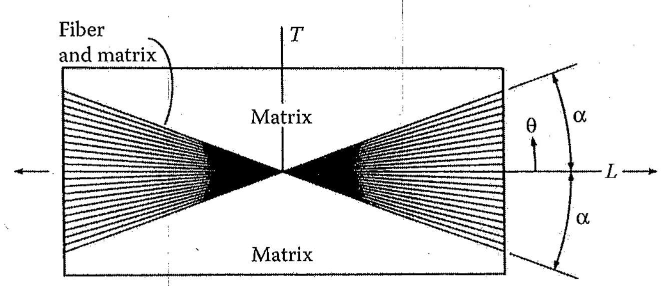

FIGURE 6.38
Composite panel with fibers arranged in X-pattern.

7. Determine the isotropic moduli $\tilde{E}$ and $\tilde{G}$ for a composite consisting of randomly oriented T300 carbon fibers in a 934 epoxy matrix if the fibers are long enough to be considered continuous. Use the properties in table 2.2. Compare the values of $\tilde{E}$ and $\tilde{G}$ calculated from the invariant expressions (eqs. [6.43]) with those calculated from the approximate expressions in equations (6.44).
8. In order to reduce material costs, a composite panel is to be made by placing fibers in the matrix material in an X-pattern of $\pm\alpha$ as shown in figure 6.38, instead of randomly distributing the fibers over all angles. The X-pattern composite is to be designed so that it has at least 90% of the stiffness of the randomly oriented fiber composite along the longitudinal (L) axis. From tensile tests of a *unidirectional* composite consisting of the same fiber and matrix materials and the same fiber volume fraction, it is found that the off-axis Young's modulus of the composite can be described by the equation

$$E_x(\theta) = 100 - 90\sin\theta \quad \text{(GPa)} \quad (0 \le \theta \le \pi/2)$$

whereas the Young's modulus of the matrix material is $E_m = 3.5$ GPa. Determine the angle α in figure 6.38 such that the longitudinal Young's modulus of the X-pattern composite is equal to 90% of the Young's modulus of the randomly oriented fiber composite.
9. Determine the coefficient of thermal expansion for a randomly oriented fiber composite in terms of the longitudinal and transverse coefficients of thermal expansion α_1 and α_2 of the corresponding unidirectional composite lamina.
10. Using micromechanics and the Tsai–Hill criterion, set up the equation for the averaged isotropic tensile strength for a randomly oriented short fiber composite. The equation should be in terms of fiber and matrix properties and volume fractions and the angle θ.

11. The RVE for an aligned discontinuous fiber composite without matrix material at its ends is shown in figure 6.4. Assume that when the RVE is loaded along the fiber direction, the interfacial shear stress distribution is given by

$$\tau = \frac{2\tau_{max}}{L}\left(\frac{L}{2} - x\right)$$

and the fiber tensile stress is given by

$$\sigma_f = \frac{4\sigma_{f\,max}x(L-x)}{L^2}$$

where L = fiber length, x = distance from left end of RVE, τ_{max} = maximum interfacial shear stress, and $\sigma_{f\,max}$ = maximum fiber tensile normal stress.

(a) Sketch the distributions of τ and σ_f along the length of the fiber.

(b) Neglecting the stress transmitted across the ends of the fiber, derive the relationship between τ_{max} and $\sigma_{f\,max}$.

(c) If the interfacial shear strength is about the same as the fiber tensile strength, and the fiber aspect ratio L/d is very large (say $L/d > 1000$), will the most likely mode of failure be interfacial shear failure or fiber tensile failure?

12. For the RVE in figure 6.4, assume that the fiber length is greater than the ineffective length, and that the distribution of the fiber tensile normal stress is given by

$$\sigma_f = \frac{4\sigma_{f\,max}x(L_i - x)}{L_i^2} \quad \text{for} \quad 0 \le x \le \frac{L_i}{2}$$

$$\sigma_f = \sigma_{f\,max} \quad \text{for} \quad \frac{L_i}{2} \le x \le \frac{L}{2}$$

(a) Determine the expression for the fiber/matrix interfacial stress, τ, and plot its distribution along the fiber length.

(b) Determine the magnitude and location of the maximum interfacial shear stress, τ_{max}, and show it on the shear stress distribution from part (a).

13. Using the Maximum Strain Criterion and micromechanics, set up the equation for predicting the averaged isotropic strength of a randomly oriented short fiber-reinforced composite. You may assume that the matrix failure strain is greater than the fiber failure strain. Your answer should be given in terms of the appropriate fiber and matrix properties and volume fractions and the variable fiber orientation angle θ. It is not necessary to solve the equation.

References

1. Kelly, A. and Tyson, W.R. 1965. Tensile properties of fibre reinforced metals: copper/tungsten and copper/molybdenum. *Journal of the Mechanics and Physics of Solids*, 13, 329–350.
2. Cox, H.L. 1952. The elasticity and strength of paper and other fibrous materials. *British Journal of Applied Physics*, 3, 72–79.
3. Rosen, B.W. 1987. Composite materials analysis and design, in Reinhart, T.J. ed., *Engineered Materials Handbook*, vol. 1, *Composites*, Sec. 4, pp. 173–281. ASM International, Materials Park, OH.
4. Agarwal, B.D. and Broutman, L.J. 1990. *Analysis and Performance of Fiber Composites*, 2d ed. John Wiley & Sons, Inc., New York.
5. Drzal, L.T., Rich, M.J., and Lloyd, P.F. 1982. Adhesion of graphite fibers to epoxy matrices: I. The role of fiber surface treatment. *Journal of Adhesion*, 16, 1–30.
6. Drzal, L.T., Rich, M.J., Koenig, M.F., and Lloyd, P.F. 1983. Adhesion of graphite fibers to epoxy matrices: II. The effect of fiber finish. *Journal of Adhesion*, 16, 133–152.
7. Kelly, A. 1973. *Strong Solids*, 2d ed. Clarendon Press, Oxford, U.K.
8. Rosen, B.W. 1965. Mechanics of composite strengthening, in *Fiber Composite Materials*, Chap. 3, pp. 37–75. American Society for Metals, Metals Park, OH.
9. Gibson, R.F., Chaturvedi, S.K., and Sun, C.T. 1982. Complex moduli of aligned discontinuous fibre reinforced polymer composites. *Journal of Materials Science*, 17, 3499–3509.
10. Hwang, S.J. 1985. Finite element modeling of damping in discontinuous fiber composites. M.S. Thesis, University of Idaho, Moscow, ID.
11. Sun, C.T. and Wu, J.K. 1984. Stress distribution of aligned short fiber composites under axial load. *Journal of Reinforced Plastics and Composites*, 3, 130–144.
12. Tyson, W.R. and Davies, G.J. 1965. A photoelastic study of the shear stress associated with the transfer of stress during fiber reinforcement. *British Journal of Applied Physics*, 16, 199–205.
13. MacLaughlin, T.F. 1968. A photoelastic analysis of fiber discontinuities in composite materials. *Journal of Composite Materials*, 2(1), 44–45.
14. Suarez, S.A., Gibson, R.F., Sun, C.T., and Chaturvedi, S.K. 1986. The influence of fiber length and fiber orientation on damping and stiffness of polymer composite materials. *Experimental Mechanics*, 26(2), 175–184.

15. Hwang, S.J. and Gibson, R.F. 1987. Micromechanical modeling of damping in discontinuous fiber composites using a strain energy/finite element approach. *Journal of Engineering Materials and Technology*, 109, 47–52.
16. Halpin, J.C. 1969. Stiffness and expansion estimates for oriented short fiber composites. *Journal of Composite Materials*, 3, 732–734.
17. Tucker, C.L. and Liang, E. 1999. Stiffness predictions for unidirectional short fiber composites: Review and evaluation. *Composites Science and Technology*, 59(5), 655–671.
18. Chon, C.T. and Sun, C.T. 1980. Stress distribution along a short fiber in fiber reinforced plastics. *Journal of Materials Science*, 15, 931–938.
19. Sun, C.T., Gibson, R.F., and Chaturvedi, S.K. 1985. Internal damping of polymer matrix composites under off-axis loading. *Journal of Materials Science*, 20, 2575–2585.
20. Baxter, W.J. 1992. The strength of metal matrix composites reinforced with randomly oriented discontinuous fibers. *Metallurgical Transactions A*, 23A, 3045–3053.
21. Lees, J.K. 1968. A study of the tensile strength of short fiber reinforced plastics. *Polymer Engineering and Science*, 8(3), 195–201.
22. Chen, P.E. 1971. Strength properties of discontinuous fiber composites. *Polymer Engineering and Science*, 11(1), 51–55.
23. Halpin, J.C. and Kardos, J.L. 1978. Strength of discontinuous reinforced composites: I. Fiber reinforced composites. *Polymer Engineering and Science*, 18(6), 496–504.
24. Nielsen, L.E. and Chen, P.E. 1968. Young's modulus of composites filled with randomly oriented fibers. *Journal of Materials*, 3(2), 352–358.
25. Tsai, S.W. and Pagano, N.J. 1968. Invariant properties of composite materials, in Tsai, S.W., Halpin, J.C., and Pagano, N.J. eds., *Composite Materials Workshop*, pp. 233–252. Technomic Publishing Co., Lancaster, PA.
26. Halpin, J.C. and Pagano, N.J. 1969. The laminate approximation for randomly oriented fibrous composites. *Journal of Composite Materials*, 3, 720–724.
27. Manera, M. 1977. Elastic properties of randomly oriented short fiber-glass composites. *Journal of Composite Materials*, 11, 235–247.
28. Christensen, R.M. and Waals, F.M. 1972. Effective stiffness of randomly oriented fibre composites. *Journal of Composite Materials*, 6, 518–532.
29. Hashin, Z. 1965. On elastic behavior of fibre reinforced materials of arbitrary transverse phase geometry. *Journal of the Mechanics and Physics of Solids*, 13, 119–134.
30. Hashin, Z. 1966. Viscoelastic fiber reinforced materials. *AIAA Journal*, 4, 1411–1417.
31. Hill, R. 1964. Theory of mechanical properties of fiber-strengthened materials: I. Elastic behavior. *Journal of the Mechanics and Physics of Solids*, 12, 199–212.
32. Chang, D.C. and Weng, G.J. 1979. Elastic moduli of randomly oriented chopped fibre composites with filled resin. *Journal of Materials Science*, 14, 2183–2190.
33. Christensen, R.M. 1976. Asymptotic modulus results for composites containing randomly oriented fibers. *International Journal of Solids and Structures*, 12, 537–544.

34. Christensen, R.M. 1979. *Mechanics of Composite Materials*. John Wiley & Sons, New York.
35. Weng, G.J. and Sun, C.T. 1979. Effects of fiber length on elastic moduli of randomly oriented chopped fiber composites, in Tsai, S.W. ed., *Composite Materials: Testing and Design (Fifth Conference)*, ASTM STP 674, pp. 149–162. American Society for Testing and Materials, Philadelphia, PA.
36. Sun, C.T., Wu, J.K., and Gibson, R.F. 1985. Prediction of material damping in randomly oriented short fiber polymer matrix composites. *Journal of Reinforced Plastics and Composites*, 4, 262–272.
37. Iijima, S. 1991. Helical microtubules of graphitic carbon. *Nature*, 354, 56–58.
38. Qian, D., Wagner, J.G., Liu, W.K., Yu, M.F., and Ruoff, R.S. 2002. Mechanics of carbon nanotubes. *Applied Mechanics Reviews*, 55(6), 495–533.
39. Thostenson, E.T., Ren, Z., and Chou, T.W. 2001. Advances in the science and technology of carbon nanotubes and their composites: A review. *Composites Science and Technology*, 61(13), 1899–1912.
40. Gates, T.S. ed. 2003. Modeling and characterization of nanostructured materials. *Composites Science and Technology (Special Issue)*, 63(11), 1497–1724.
41. Tibbetts, G.G. and McHugh, J.J. 1999. Mechanical properties of vapor-grown carbon fiber composites with thermoplastic matrices. *Journal of Materials Research*, 14(7), 2871–2880.
42. Qian, D., Dickey, E.C., Andrews, R., and Rantell, T. 2000. Load transfer and deformation mechanisms in carbon nanotube-polystyrene composites. *Applied Physics Letters*, 76 (20), 2868–2870.
43. Yu, M.-F., Files, B., Arepalli, S., and Ruoff, R.S. 2000. Tensile loading of ropes of single wall carbon nanotubes and their mechanical properties. *Physical Review Letters*, 84(24), 5552–5555.
44. Fisher, F.T. 2002. Nanomechanics of carbon nanotube-reinforced polymers. Ph.D. Thesis, Department of Mechanical Engineering, Northwestern University.
45. Fisher, F.T., Bradshaw, R.D., and Brinson, L.C. 2003. Fiber waviness in nanotube-reinforced polymer composites — I: Modulus predictions using effective nanotube properties. *Composites Science and Technology*, 63(11), 1689–1703.
46. Bradshaw, R.D., Fisher, F.T., and Brinson, L.C. 2003. Fiber waviness in nanotube-reinforced polymer composites — II: Modeling via numerical approximation of the dilute strain concentration tensor. *Composites Science and Technology*, 63(11), 1705–1722.
47. Anumandla, V. 2004. A comprehensive closed form micromechanics model for estimating the elastic modulus of nanotube-reinforced composites. M.S. Thesis, Department of Mechanical Engineering, Wayne State University.
48. Anumandla, V. and Gibson, R.F. 2006. A comprehensive closed form micromechanics model for estimating the elastic modulus of nanotube-reinforced composites. *Composites Part A: Applied Science and Manufacturing*. 37(12), 2178–2185.
49. Chan, W.S. and Wang, J.S. 1994. Influence of fiber waviness on the structural response of composite laminates. *Journal of Thermoplastic Composite Materials*, 7(3), 243–260.

50. Hsiao, H.M. and Daniel, I.M. 1996. Elastic properties of composites with fiber waviness. *Composites Part A: Applied Science and Manufacturing*, 27(10), 931–941.
51. Andrews, R., Jacques, D., Minot, M., and Ratnell, T. 2002. Fabrication of carbon multiwall nanotube/polymer composites by shear mixing. *Macromolecular Materials Engineering*, 287(6), 395–403.
52. Vlasveld, D.P.N., Bersee, H.E.N., and Picken, S.J. 2005. Nanocomposite matrix for increased fibre composite strength. *Polymer*, 46, 10269–10278.
53. Thostenson, E.T., Li, W.Z., Wang, D.Z., Ren, Z.F., and Chou, T.W. 2002. Carbon nanotube/carbon fiber hybrid multiscale composite. *Journal of Applied Physics*, 91(9), 6034–6037.